



UNIVERSITÀ  
DEGLI STUDI  
FIRENZE

## DOTTORATO DI RICERCA IN SCIENZE CHIMICHE

CICLO XXX

COORDINATORE Prof. PIERO BAGLIONI

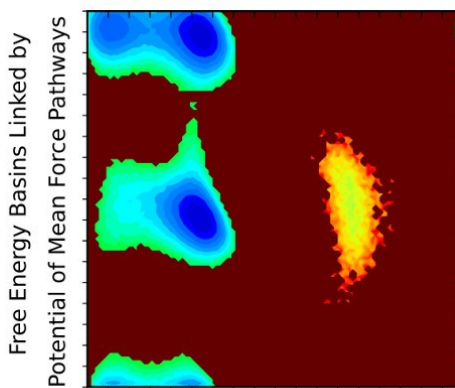
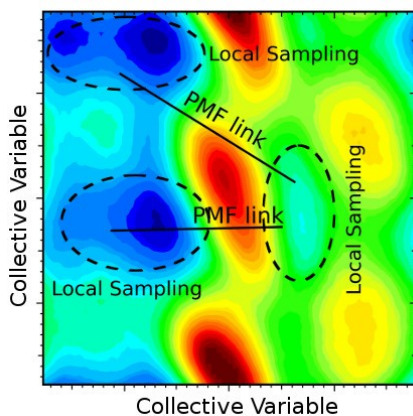
### SAMPLING METHODS AND FREE ENERGY ESTIMATORS FOR COMPUTER SIMULATIONS: DEVELOPMENT AND APPLICATIONS

#### **Dottorando**

Dott. Edoardo Giovannelli

#### **Tutore**

Prof. Riccardo Chelli





UNIVERSITÀ  
DEGLI STUDI  
FIRENZE

DOTTORATO DI RICERCA IN  
SCIENZE CHIMICHE

CICLO XXX

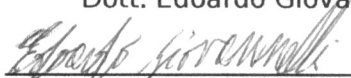
COORDINATORE Prof. PIERO BAGLIONI

SAMPLING METHODS AND FREE ENERGY  
ESTIMATORS FOR COMPUTER SIMULATIONS:  
DEVELOPMENT AND APPLICATIONS

Settore Scientifico Disciplinare CHIM/02

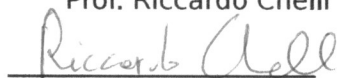
**Dottorando**

Dott. Edoardo Giovannelli

  
(firma)

**Tutore**

Prof. Riccardo Chelli

  
(firma)

**Coordinatore**

Prof. Piero Baglioni

\_\_\_\_\_  
(firma)

Anni 2014/2017 (di inizio e fine corso)

---

## Contents

---

<b>1</b>	<b>List of the Main Acronyms</b>	<b>1</b>
<b>2</b>	<b>Abstract</b>	<b>3</b>
<b>3</b>	<b>Introduction</b>	<b>5</b>
<b>4</b>	<b>Nonequilibrium work theorems</b>	<b>9</b>
4.1	Introduction . . . . .	9
4.2	Principles of thermodynamics . . . . .	10
4.3	Crooks fluctuation theorem . . . . .	13
4.4	Other nonequilibrium work theorems . . . . .	15
<b>5</b>	<b>Nonequilibrium work theorems applied to transitions between configura- tional domains</b>	<b>17</b>
5.1	Introduction . . . . .	17
5.2	Theory . . . . .	20
5.2.1	Configurational-Domains Transition scheme (CDTS) . . . . .	20
5.2.2	Crooks fluctuation theorem under CDTS . . . . .	22

---

CONTENTS

---

5.2.3	CDTS under deterministic dynamics . . . . .	24
5.3	Numerical Tests . . . . .	26
5.3.1	Systems and simulation details . . . . .	26
5.3.2	Results . . . . .	31
5.3.3	Discussion and concluding remarks . . . . .	35
<b>6</b>	<b>Annealed importance sampling with constant cooling rate</b>	<b>39</b>
6.1	Introduction . . . . .	39
6.2	Theory . . . . .	41
6.2.1	Annealed importance sampling . . . . .	41
6.2.2	Annealed importance sampling from generalized nonequilibrium path-ensemble theory . . . . .	43
6.3	Model system and simulations . . . . .	46
6.4	Simulation tests . . . . .	49
6.5	Concluding remarks . . . . .	54
<b>7</b>	<b>Computing free energy differences of configurational basins</b>	<b>55</b>
7.1	Introduction . . . . .	55
7.2	Theory . . . . .	58
7.3	System and simulation details . . . . .	62
7.3.1	System . . . . .	62
7.3.2	Shared simulation setup . . . . .	64
7.3.3	Path-Linked Domains scheme . . . . .	64
7.3.4	Serial generalized ensemble simulation . . . . .	69
7.4	Simulation tests . . . . .	70
7.5	Conclusive remarks . . . . .	75
<b>8</b>	<b>Binding free energies of host-guest systems by nonequilibrium alchemical simulations with constrained dynamics</b>	<b>77</b>
8.1	Introduction . . . . .	77
8.2	Thermodynamics of the noncovalent binding . . . . .	79
8.3	The double-decoupling method . . . . .	83
8.3.1	Decoupling the ligand from solvent and receptor: $\Delta G_1^{\circ}$ calculation . .	85



## CONTENTS

---

8.3.2	Decoupling the ligand from the solvent: $\Delta G_2^\circ$ calculation . . . . .	94
8.4	Using the ligand-receptor distance as binding descriptor in the double-decoupling method . . . . .	97
8.5	Zn(II)-anion complex . . . . .	100
8.5.1	Computational details . . . . .	100
8.5.2	Results . . . . .	103
8.6	$\beta$ -cyclodextrin with aromatic compounds . . . . .	110
8.6.1	Computational details . . . . .	110
8.6.2	Results . . . . .	113
8.7	Conclusions . . . . .	117
	<b>Bibliography</b>	<b>119</b>

## CONTENTS

---

---

## List of the Main Acronyms

---

- ABFE: Absolute Binding Free Energy;
- AIS: Annealed Importance Sampling;
- BiD-AP: Binded-Domain Alchemical-Path scheme;
- CD: CycloDextrine;
- CDTS: Configurational Domains Transitions scheme;
- CFT: Crooks Fluctuation Theorem;
- JE: Jarzynski Equality;
- MC: Monte Carlo simulation;
- MD: Molecular Dynamics simulation;
- NCMC: Nonequilibrium Candidate Monte Carlo;

## List of the Main Acronyms

---

- NPT: statistical ensemble at fixed Number of particles, Pressure and Temperature;
- NVE: statistical ensemble at fixed Number of particles, Volume and Energy;
- NVT: statistical ensemble at fixed Number of particles, Volume and Temperature;
- NWTs: Nonequilibrium Work Theorems;
- PLD: Path-Linked Domains scheme;
- PMF: Potential of Mean Force;
- SiP-AP: Single-Point Alchemical-Path scheme;
- SGE: Serial Generalized Ensemble;
- SMD: Steered Molecular Dynamics simulation.

---

**Abstract**

---

Strategies extending the range of application of nonequilibrium work theorems [Phys. Rev. E, 2000, 61, 2361] and improving the efficiency of the related computational techniques are developed and tested. The Configurational Domains Transitions scheme, based on steps consisting of transition kernels alternated to relaxation kernels, performs nonequilibrium paths connecting two states with arbitrary shape and size in the space of the collective coordinates, giving access to their free energy difference. The method can be viewed as a generalization of the Steered Molecular Dynamics [Phys. Rev. E, 2008, 677, 016709]. Moreover, Annealed Importance Sampling [Stat. Comput., 2001, 11, 125] is reviewed, from the perspective of nonequilibrium path-ensemble averages. The equivalence of Neal and Crooks treatments highlights the generality of the method, which goes beyond the mere thermal protocols. A temperature schedule based on a constant cooling rate outperforms stepwise cooling schedules. Furthermore, the Path-Linked Domains scheme is proposed as an alternative approach to estimate free energy differences between conformational states, defined in terms of collective coordinates of the molecular system. The computational protocol is organized into three independent stages. Two of them consist of independent simulations

aimed at sampling the states of interest. Free energy evaluation is completed by estimation of the potential of mean force difference between two arbitrary points of the configurational surface, located around the target domains. Finally, the developed algorithms are adapted to the context of ligand-receptor equilibria, in order to evaluate absolute binding free energies of noncovalent complexes. We have developed two approaches, termed binded-domain and single-point alchemical-path schemes, based on the possibility of performing alchemical trajectories during which the ligand is constrained to fixed positions relative to the receptor. The first scheme exploits Configurational Domains Transitions framework to estimate the free energy difference between the coupled and uncoupled states of the ligand-receptor complex. On the other side, the single-point scheme resembles the Path Linked Domains procedure, originally conceived in the context of conformational equilibria, to avoid the calculation of the binding-site volume by introducing an additional equilibrium simulation of ligand and receptor in the bound state. The extra computational effort required by the second scheme leads to a significant improvement of accuracy in the free energy estimates. However, comparison with experimental data and previous molecular dynamics simulation studies confirm the validity of both nonequilibrium-alchemical methodologies.

The free energy difference between two equilibrium states of a molecular system is the reversible work necessary to perform a transition between such states. Therefore, it represents the fundamental quantity to assess the relative stability of the two states. For this reason, several simulation techniques for free energy calculations have been devised [41, 69]: thermodynamic integration[116], perturbation theory[211], and more advanced histogram reweighting or thermodynamic path sampling strategies[41]. These methods are finalized to sample the phase space in equilibrium or near-equilibrium conditions. On the other side, a different approach for free energy calculation consists of guiding the system from an initial to a final state by nonequilibrium switches. These transformations are produced by Steered Molecular Dynamics (SMD), during which an external potential is applied to constrain a collective coordinate to fluctuate around a value given by a fixed time dependent protocol[151]. Nonequilibrium strategies are based on two main Nonequilibrium Work Theorems (NWTs), *i.e.* the Jarzynski equality[106, 107] (JE) and the Crooks fluctuation theorem[48–50] (CFT), which relate the free energy difference of two thermodynamic states, say  $A$  and  $B$ , to the work performed in a set of realizations switching the system between such states. The first

of them was formulated in 1997 by Jarzynski[106], and successively in a wide variety of cases: Markov chains[49], Langevin dynamical systems[168], Hamiltonian e non Hamiltonian dynamics [51, 108, 166], quantum systems [139], systems underlying thermal variations [25, 30, 31, 202] and electronic fotoexcitation processes[70]. The first experimental test of JE was carried on by Liphardt *et al.* [125], determining the irreversible steering mechanical work performed on a single DNA fragment. The basic difference between JE and CFT is that the former employs realizations driving the system in only one direction ( $A \rightarrow B$  or  $B \rightarrow A$ ), while CFT involves realizations performed in both directions of the process. The theorem was initially proved for Markovian microscopically reversible systems in the context of Monte Carlo simulations[48]. Successively, its validity was extended to Markovian dynamical systems in both NPT and NVT ensembles, that satisfy detailed balance conditions[30, 159]. CFT has been verified experimentally[45, 55, 56, 77, 115, 167, 199], and is having a relevant echo in computer simulations. In this field, in fact, an amount of strategies aimed at computing free energy differences[25, 130, 177] and potential of mean force [27, 35, 36, 54, 68, 81, 84, 137, 142, 143, 145] has been proposed. Also the JE has been the object of many studies to enhance its performances[29, 144, 148, 152, 206, 207], even if its lower efficiency with respect to CFT-based free energy estimators is recognized[41, 88]. Let consider a system exchanging energy with the environment in two ways, namely the contact with a thermal bath at the inverse temperature  $\beta$  and the coupling with an external device, which keeps full control on a chosen collective coordinate of the system  $\xi(\mathbf{x})$  (function of the microstate  $\mathbf{x}$ ), through a control parameter  $\lambda$ . The coordinate  $\xi(\mathbf{x})$  corresponds, generally, to some structural property of the system, *e.g.*, interatomic distances, bending and torsional angles, but even more complex parametric dependences involving thermal quantities can be considered[25, 31, 32, 202]. The control parameter  $\lambda$  may change according to an arbitrary time schedule  $\lambda(t)$ , starting from a configuration sampled at equilibrium with  $\lambda$  held fixed at  $\lambda_A \equiv \lambda(0)$  up to a final (in general nonequilibrium) state with  $\lambda_B \equiv \lambda(\tau)$ , being  $\tau$  the duration of the finite-time protocol. Because of thermal fluctuations of the uncontrolled degrees of freedom in the initial states and during the transformations, a different amount of work  $W$  is performed on the system in dependence of the dynamical path followed during the transformation. The corresponding work distribution  $P(W)$  will depend not only on the physical nature of the system and on the type of driven collective coordinate, but also on the specific  $\lambda(t)$  time schedule employed in the set of realizations. The existence of a con-



trolled coordinate allows us to define the  $\lambda$ -dependent free energy profile  $F(\lambda)$ , the so-called potential of mean force[116] (PMF), which is defined for any equilibrium state at fixed  $\lambda$ . The PMF can be evaluated from  $P(W)$  via JE as,

$$F(\lambda) - F(\lambda_A) = -\beta^{-1} \ln \left( \int_{-\infty}^{+\infty} dW P_{\lambda_A \rightarrow \lambda}(W) e^{-\beta W} \right), \quad (3.1)$$

where  $P_{\lambda_A \rightarrow \lambda}(W)$  is the work distribution obtained from realizations in which the control parameter varies from  $\lambda_A$  to  $\lambda$ . An analogous reasoning can be done for realizations performed in the opposite direction of the process, during which a time reverse protocol, from  $\lambda_B$  to  $\lambda$ , is applied. This allows to recover the PMF with  $\lambda = \lambda_B$  as the reference state, namely  $F(\lambda) - F(\lambda_B)$ . Concerning the CFT, the most popular relationship, first proved for classical systems[48, 49] and later extended to closed as well as open quantum systems[22, 43, 185], is perhaps the one which establishes a universal connection between  $P_{\lambda_A \rightarrow \lambda_B}(W)$  and  $P_{\lambda_B \rightarrow \lambda_A}(-W)$ [50]:

$$\frac{P_{\lambda_A \rightarrow \lambda_B}(W)}{P_{\lambda_B \rightarrow \lambda_A}(-W)} = e^{\beta(W - \Delta F)}, \quad (3.2)$$

where  $P_{\lambda_B \rightarrow \lambda_A}(-W)$  is the probability of performing an amount of work  $-W$  in the process  $\lambda_B \rightarrow \lambda_A$  and  $\Delta F = F(\lambda_B) - F(\lambda_A)$ . The JE can be proved to be a consequence of eq. 3.2 (see, for example, Ref.[49]). NWTs will be derived in chapter 4, and preceded by a summary of the basic thermodynamical concepts which lay down the entire exposition of the present research. In the following chapters, strategies will be presented which extend the range of application of NWTs and improve the efficiency of the related computational techniques. In chapter 5, the Configurational Domains Transitions scheme (CDTS) is introduced, based on steps consisting of transition kernels alternated to relaxation kernels, that allows the production of nonequilibrium paths connecting two states with arbitrary shape and size in the space of the collective coordinates, giving access to their free energy difference. The method can be viewed as a generalization of the SMD. In chapter 6 we review the Annealed Importance Sampling (AIS)[140], from the perspective of nonequilibrium path-ensemble averages. The equivalence of Neal[140], and Crooks[50] treatments highlights the generality of the method, which goes beyond the mere thermal protocols. Furthermore, we show that a temperature schedule based on a constant cooling rate outperforms stepwise cooling schedules. In chapter 7, the Path-Linked Domains (PLD) scheme is proposed as

an approach (alternative to CDTS) to estimate free energy differences between conformational states A and B, defined in terms of collective coordinates of the molecular system. The computational protocol is organized into three stages that can be carried on simultaneously. Two of them consist of independent simulations aimed at sampling, in turn, A and B states. Free energy evaluation is completed by estimation of the potential of mean force difference between two arbitrary points of the configurational surface, located the first around A and the second around B. In the last chapter 8, the algorithms developed in the previous chapters 5 and 7 are adapted to the context of ligand-receptor equilibria, in order to evaluate absolute binding free energies of noncovalent complexes. We indeed develop two approaches, termed binded-domain and single-point alchemical-path schemes (BiD-AP and SiP-AP), based on the possibility of performing alchemical trajectories during which the ligand is constrained to fixed positions relative to the receptor. The BiD-AP scheme exploits extension of NWTs (reported in chapter 5) to estimate the free energy difference between the coupled and uncoupled states of the ligand-receptor complex. With respect to the fast-switching decoupling method without constraints, BiD-AP prevents the ligand from leaving the binding site, but still requires an estimate of the positional binding-site volume, which may not be a simple task. On the other side, the SiP-AP scheme resembles the PLD procedure, originally conceived in the context of conformational equilibria, to avoid the calculation of the binding-site volume by introducing an additional equilibrium simulation of ligand and receptor in the bound state. We show that the extra computational effort required by SiP-AP leads to a significant improvement of accuracy in the free energy estimates. Validation is provided by comparing binding free-energy data relative to two poses of a Zn(II)-anion complex. Absolute binding free energies of 1:1 complexes of  $\beta$ -cyclodextrin with aromatic compounds (benzene and naphthalene) is also estimated. Comparison with experimental data and previous MD simulation studies confirm the validity of both BiD-AP and SiP-AP nonequilibrium-alchemical methodologies.

## 4.1 Introduction

In Steered Molecular Dynamics (SMD) simulations[151], the introduction of a stiff external potential restrains the system to a defined value of a collective coordinate. During a realization of the nonequilibrium process, a parameter evolves in time according to a prescribed time schedule, guiding the evolution of the collective coordinate itself. From work performed along an ensemble of SMD trajectories whose starting states are sampled in equilibrium conditions, Nonequilibrium Work Theorems (NWTs) allow to recover the Potential of Mean Force (PMF) as a function of the collective coordinate, assuming the stiff spring approximation[151] or making use of reweighting techniques[79]. We report here a brief derivation of Nonequilibrium Work Theorems (NWTs), relating free energy variations to distributions of nonequilibrium work performed along sets of trajectories sampled in equilibrium conditions. Exposition of NWTs will be preceded by a summary of fundamental concepts of thermodynamics in sec. 4.2. In sec. 4.3 will be introduced the Crooks Fluctuations Theorem (CFT)[49, 50], that links the probability to observe a trajectory with the

probability of observing its time reversal. The theorem was initially proved for Markovian microscopically reversible systems in the context of Monte Carlo simulations[48]. Successively, its validity was extended to Markovian dynamical systems in both NPT and NVT ensemble, that satisfy detailed balance conditions[30, 159]. From CFT, other important NWTs will be deduced in the following sec. 4.4.

## 4.2 Principles of thermodynamics

An homogeneous macroscopic system, constituted by a fixed number of particles, is described by a set of state parameters: volume  $V$ , pressure  $P$  and temperature  $T$ [14, 19]. The same parameters are not independent, but tied by a single equation of state, specific for the target system. The condition at which the parameters  $P$ ,  $V$  and  $T$  maintain in time values univocally defined and fixed is the equilibrium state of the system. In a thermodynamic process, a system can evolve from an initial to a final equilibrium states, that differ for the values of the state parameters. A state function is any thermodynamic property whose variation between two equilibrium states depends only on the parameters describing the same states, and not on the intermediate path followed by a process connecting them.

The first principle of thermodynamics states the variation of system energy  $E$  corresponds to a state function, sum of heat  $Q$  and work  $W'$  exchanged between the system and the environment (in a thermodynamic process, conventionally we pose  $Q > 0$  if the heat is adsorbed by the system, while  $W' > 0$  if work is performed on the system). Considering an infinitesimal process we have:

$$dE = \delta Q + \delta W'. \quad (4.1)$$

The notation points out that infinitesimal heat and work are not exact differentials, as  $Q$  and  $W'$  are not functions of state of the isolated system, but depend on the path of the transformation. In an isolated system, the first principle implies the conservation of energy. The second principle, instead, allows to determine the spontaneous direction of processes taking place into the same isolated system. In this context, we define ideal reversible processes, consisting of series of intermediate equilibrium states. Real processes, not happening in this way, are called irreversible. Nevertheless, the velocity of a process alters the degree of reversibility: the more a process is slow, the more it is near to reversibility. The second principle introduces a state function, called entropy and denoted with  $S$ . Entropy is

described by the Clausius relation, describing an infinitesimal process along which the heat exchange  $\delta Q$  takes place at temperature  $T$ :

$$dS \geq \frac{\delta Q}{T}, \quad (4.2)$$

where the equality is valid only for reversible transformations. As already stated, the second principle allows to establish the spontaneous direction of irreversible processes. Indeed, if eq. 4.2 is satisfied for a transformation happening in the spontaneous direction, it is not satisfied for the inverse not spontaneous process. We define now the Helmholtz  $F$  and Gibbs free energy  $G$  state functions:

$$F = E - TS \quad (4.3)$$

$$G = E + PV - TS. \quad (4.4)$$

Making use of both first and second thermodynamics principles (eq. 4.1 e 4.2), we can write for a generic process:

$$dE \leq TdS + \delta W', \quad (4.5)$$

Decomposing the term  $\delta W' = \delta W - PdV$  in an expansive,  $-PdV$ , ed a not expansive  $\delta W$  term, we gain

$$dE + PdV - TdS \leq \delta W. \quad (4.6)$$

From 4.6 can be shown that for a transformation at fixed  $V$  and  $T$

$$[dF]_{V,T} \leq \delta W. \quad (4.7)$$

Helmholtz free energy difference between two states at the same volume and temperature corresponds to non expansive work necessary to carry on a reversible process connecting the two states. If the transformation is irreversible, work will instead be greater then free energy difference. For a process at fixed  $P$  and  $T$ , instead,

$$[dG]_{P,T} \leq \delta W. \quad (4.8)$$

Gibbs free energy difference between two states at the same pressure and temperature corresponds to non expansive work necessary to carry on a reversible process connecting the two states. Again, work performed along an irreversible process will overcome free energy change.

Our aim is now to relate macroscopic properties of a thermodynamic system to its microscopic state [12, 23, 69]. In this context, a molecular system will be described, in classical approximation, by a vector  $\mathbf{x}$ , collecting coordinates and momenta of all the  $N$  atoms composing the system. The set of microstates in the phase space  $\mathcal{D}$ , compatible with the macroscopic state of the system, define the ensemble of the system. We define ensemble NVT as the set of microstates of an  $N$  particles system, at equilibrium at fixed volume  $V$  and temperature  $T$ . Analogously, we define the ensemble NPT, constituted by the set of microstates of an  $N$  particles system, at equilibrium at fixed pressure  $P$  and temperature  $T$ . To every microstate is associated an ensemble density of probability  $p(\mathbf{x})$ , such that the fraction of states contained in the infinitesimal volume  $d\mathbf{x}$  centered in microstate  $\mathbf{x}$  is  $p(\mathbf{x})d\mathbf{x}$ . The density probability of an ensemble NVT, denoted  $p_{\text{NVT}}(\mathbf{x})$ , is given by the following equation

$$p_{\text{NVT}}(\mathbf{x}) = \frac{e^{-\beta H(\mathbf{x})}}{Q_{\text{NVT}}} \quad (4.9)$$

where  $\beta = (k_B T)^{-1}$  con  $k_B$  costante di Boltzmann. The Hamiltonian function  $H(\mathbf{x})$  corresponds to the energy of the microstate  $\mathbf{x}$ . The partition function of the NVT ensemble is defined by the following equation:

$$Q_{\text{NVT}} = \int_{\mathcal{D}} d\mathbf{x} e^{-\beta H(\mathbf{x})}. \quad (4.10)$$

It can be shown that  $Q_{\text{NVT}}$  is correlated to Helmholtz free energy  $F$ , according to the relation

$$Q_{\text{NVT}} = e^{-\beta F}. \quad (4.11)$$

Analogously, we define the partition function of an NPT ensemble:

$$Q_{\text{NPT}} = \int_0^\infty dV \int_{\mathcal{D}(V)} d\mathbf{x} e^{-\beta[H(\mathbf{x})+PV]}, \quad (4.12)$$

where the phase space  $\mathcal{D}(V)$  of microstates  $\mathbf{x}$  is now dependent on the volume  $V$ . A relation analogous to eq. 4.11 is valid between the partition function  $Q_{\text{NPT}}$  and Helmholtz free energy:

$$Q_{\text{NPT}} = e^{-\beta G}. \quad (4.13)$$

### 4.3 Crooks fluctuation theorem

Given a system evolving in the phase space  $\mathcal{D}$  at fixed inverse temperature  $\beta$ , we are interested in evaluating the relative stability (free energy difference) of two thermodynamic states identified by specific Hamiltonians,  $H_A(\mathbf{x})$  and  $H_B(\mathbf{x})$ , associated with the non-normalized probability distributions  $\rho_A(\mathbf{x}) = e^{-\beta H_A(\mathbf{x})}$  and  $\rho_B(\mathbf{x}) = e^{-\beta H_B(\mathbf{x})}$ . To this aim, we produce trajectories  $\Gamma$ , consisting of  $N$  (finite or infinite) steps along which the Hamiltonian evolves in time from  $H_0(\mathbf{x}) = H_A(\mathbf{x})$  (state  $A$ ) to  $H_N(\mathbf{x}) = H_B(\mathbf{x})$  (state  $B$ ), by a fixed switching protocol. We remark that only a single protocol has to be designed to establish the temporal behaviour along the trajectory of the Hamiltonian  $H_i(\mathbf{x})$ , and hence the underlying non-normalized equilibrium probability distribution  $\rho_i(\mathbf{x}_i) = e^{-\beta H_i(\mathbf{x}_i)}$ . A generic path is described by a Markovian evolution scheme, which preserves proper balance conditions aimed to preserve the microscopic reversibility of the produced trajectory  $\Gamma$  in the phase space  $\mathcal{D}$ , starting from the microstate  $\mathbf{x}_0$  and ending in the microstate  $\mathbf{x}_N$  by a sequence of finite or infinite number of steps. The initial microstate  $\mathbf{x}_0$  is sampled according to the normalized probability distribution

$$p_A(\mathbf{x}_0) = \rho_A(\mathbf{x}_0)/Q_A, \quad (4.14)$$

where  $Q_A = \int_{\mathcal{D}} d\mathbf{x} \rho_A(\mathbf{x})$  is the partition function of the state  $A$ . Moreover,  $H_N(\mathbf{x}_N) \equiv H_B(\mathbf{x}_N)$ . Each step of the trajectory consists of move  $\mathbf{x}_i \rightarrow \mathbf{x}_{i+1}$ , realized according to a transition kernel  $S(\mathbf{x}_i \rightarrow \mathbf{x}_{i+1}) \geq 0$ , such that  $\int_{\mathcal{D}} d\mathbf{x}'_i S(\mathbf{x}_i \rightarrow \mathbf{x}'_i) = 1$ . These moves are performed by enforcing the detailed balance condition

$$\rho_i(\mathbf{x}_i) S(\mathbf{x}_i \rightarrow \mathbf{x}_{i+1}) = \rho_i(\mathbf{x}_{i+1}) S(\mathbf{x}_{i+1} \rightarrow \mathbf{x}_i). \quad (4.15)$$

Let us consider the trajectory  $\Gamma^*$ , reverse to  $\Gamma$ , whose initial microstate is assumed to be sampled according to the equilibrium probability distribution  $p_B(\mathbf{x}) = \rho_B(\mathbf{x})/Q_B$  (cf. eq. 4.14). Of course, as there is no reason to take the  $\Gamma$  path as the reference for the transition distributions, an analogous reasoning can be applied to the reverse path  $\Gamma^*$ . We start observing that the ratio between the probability  $P_{A \rightarrow B}[\Gamma]$  of generating the trajectory  $\Gamma$  in the  $A \rightarrow B$  process, and the probability  $P_{B \rightarrow A}[\Gamma^*]$  of generating the trajectory  $\Gamma^*$  in a time reverse process  $B \rightarrow A$  (both trajectories starting from microstates sampled at equilibrium),

is given by the equation[48]

$$\frac{P_{A \rightarrow B}[\Gamma]}{P_{B \rightarrow A}[\Gamma^*]} = \frac{p_A(\mathbf{x}_0)}{p_B(\mathbf{x}_N)} \prod_{i=0}^{N-1} \frac{S(\mathbf{x}_i \rightarrow \mathbf{x}_{i+1})}{S(\mathbf{x}_{i+1} \rightarrow \mathbf{x}_i)}. \quad (4.16)$$

Exploiting eq. 4.15, together with eq. 4.14 for  $p_A(\mathbf{x}_0)$  (and the analogous relationship  $p_B(\mathbf{x}_N) = \rho_B(\mathbf{x}_N)/Q_B$ ), we obtain

$$\frac{P_{A \rightarrow B}[\Gamma]}{P_{B \rightarrow A}[\Gamma^*]} = \frac{Q_B}{Q_A} \frac{\rho_A(\mathbf{x}_0)}{\rho_B(\mathbf{x}_N)} \prod_{i=0}^{N-1} \frac{\rho_i(\mathbf{x}_{i+1})}{\rho_i(\mathbf{x}_i)} = \frac{Q_B}{Q_A} \prod_{i=1}^N \frac{\rho_{i-1}(\mathbf{x}_i)}{\rho_i(\mathbf{x}_i)}, \quad (4.17)$$

where the equivalences  $\rho_0(\mathbf{x}_0) \equiv \rho_A(\mathbf{x}_0)$  and  $\rho_N(\mathbf{x}_N) \equiv \rho_B(\mathbf{x}_N)$  have been used in going from the middle to the right term of the equation. From eq. 4.17, we derive a fundamental expression, involving the free energy difference  $\Delta F_{AB} = -\beta^{-1} \ln(Q_B/Q_A)$  between the states  $A$  and  $B$

$$\frac{P_{A \rightarrow B}[\Gamma]}{P_{B \rightarrow A}[\Gamma^*]} = e^{\beta(W_{A \rightarrow B}[\Gamma] - \Delta F_{AB})}. \quad (4.18)$$

Accounting for the ratio between transition and equilibrium distributions relative to microstates collected along the trajectory, we have introduced the mechanical work,

$$W_{A \rightarrow B}[\Gamma] = \beta^{-1} \ln \left( \prod_{i=1}^N \frac{\rho_{i-1}(\mathbf{x}_i)}{\rho_i(\mathbf{x}_i)} \right) = \sum_{i=1}^N [H_i(\mathbf{x}_i) - H_{i-1}(\mathbf{x}_i)]. \quad (4.19)$$

In eq. 4.19, the generic term in the sum corresponds to the work performed on the system to switch the Hamiltonian from  $H_{i-1}(\mathbf{x}_i)$  to  $H_i(\mathbf{x}_i)$  at fixed configuration. The sum over all the switching steps provides the total work  $W_{A \rightarrow B}[\Gamma]$  performed during the  $\Gamma$  path. For each move  $i$ , the occurrence of  $\rho_{i-1}(\mathbf{x}_i)/\rho_i(\mathbf{x}_i) > Q_{i-1}/Q_i$  will enhance the dissipation associated with the path. On the contrary, an anti-dissipative contribution will arise from  $\rho_{i-1}(\mathbf{x}_i)/\rho_i(\mathbf{x}_i) < Q_{i-1}/Q_i$ . We underline that the CFT is straightforwardly extensible to a continuous process, described by an Hamiltonian function  $H(\mathbf{x}, \lambda(t))$ , changing in time  $t$  under a fixed protocol, given by the time dependent parameter  $\lambda(t)$ . For a trajectory  $\Gamma$ , performed between initial time 0 and final time  $\tau$ , mechanical work becomes

$$W_{A \rightarrow B}[\Gamma] = \int_0^\tau \frac{\partial}{\partial t} H(\mathbf{x}, \lambda(t)) dt, \quad (4.20)$$



Moreover, we point out that a continuous deterministic dynamics represents a special case of the present stochastic Markovian process. From the CFT of eq. 4.18, it is possible to recover other important nonequilibrium work theorems, some of which are shortly revised in the next section 4.4.

## 4.4 Other nonequilibrium work theorems

Multiplying both members of eq. 4.18 by a generic path-functional  $\mathcal{A}_{A \rightarrow B}[\Gamma]$ , defined for the set of trajectories in phase space  $\mathcal{D}$ , we get

$$\mathcal{A}_{A \rightarrow B}[\Gamma] P_{A \rightarrow B}[\Gamma] e^{-\beta W_d} = \mathcal{A}_{B \rightarrow A}^*[\Gamma^*] P_{B \rightarrow A}[\Gamma^*], \quad (4.21)$$

where  $\mathcal{A}_{B \rightarrow A}^*[\Gamma^*] = \mathcal{A}_{A \rightarrow B}[\Gamma]$  is the path-functional associated with the time reversed trajectory  $\Gamma^*$ . We have introduced the dissipated work  $W_d = W_{A \rightarrow B}[\Gamma] - \Delta F_{AB}$ . Summing both members of eq. 4.21 over all possible paths furnishes eq.1 reported in Ref.[50]:

$$\langle \mathcal{A} e^{-\beta W_d} \rangle_{A \rightarrow B} = \langle \mathcal{A}^* \rangle_{B \rightarrow A}. \quad (4.22)$$

The angular brackets denote the path-ensemble averages performed in the two directions of the process. From eq. 4.22, nonequilibrium work theorems follow straightforwardly. The choice  $\mathcal{A}_{A \rightarrow B}[\Gamma] = \mathcal{A}_{B \rightarrow A}^*[\Gamma^*] = 1$  gives the Jarzynski equality (JE, cf. sec. IIIA of Ref.[50])

$$\langle e^{-\beta W} \rangle_{A \rightarrow B} = e^{-\beta \Delta F_{AB}}. \quad (4.23)$$

Free energy variation, *i.e.* the reversible work, is given by average exponential work performed on nonequilibrium trajectories, whose initial microstates are sampled in equilibrium conditions. JE, here deduced from CFT, was demonstrated before it[106], and extended to Monte Carlo simulations and Langevin systems [49, 168]. CFT for work distributions is recovered by setting  $\mathcal{A}_{A \rightarrow B}[\Gamma] = \delta(W_{A \rightarrow B}[\Gamma] - W)$  and hence  $\mathcal{A}_{A \rightarrow B}^*[\Gamma^*] = \delta(W_{B \rightarrow A}[\Gamma^*] + W)$  (cf. sec. IIIB of Ref.[50]),

$$\frac{P_{A \rightarrow B}(W)}{P_{B \rightarrow A}(-W)} = e^{\beta(W - \Delta F_{AB})}. \quad (4.24)$$

Equation 4.24 relates the dissipated work  $W - \Delta F_{AB}$  to the ratio between the probability  $P_{A \rightarrow B}(W)$  of observing the generalized dimensionless work  $W$  in the  $A \rightarrow B$  process and

the probability  $P_{B \rightarrow A}(-W)$  of observing the work  $-W$  in the reverse process. Probabilities  $P_{A \rightarrow B}(W)$  and  $P_{B \rightarrow A}(-W)$  are both evaluated picking the initial microstates from equilibrium simulations related to the states  $A$  and  $B$ , respectively. In a graphic reporting  $P_{A \rightarrow B}(W)$  and  $P_{B \rightarrow A}(-W)$  as a function of  $W$ , the intersection point is observed at  $W = \Delta F_{A \rightarrow B}$ . Rendering the process more reversible, decreasing its speed, overlap between  $P_F(W)$  and  $P_B(-W)$  increases. In the limit of a reversible process, both the distribution collapse to the Dirac delta function  $\delta(W - \Delta F_{A \rightarrow B})$ . By following the arguments of Shirts *et al.*[174], using eq. 4.24 it is possible to get a (Bennett-like[18]) maximum likelihood estimator of  $\Delta F_{AB}$  (cf. eq. 8 of Ref.[174])

$$\left\langle \frac{1}{n_{B \rightarrow A} + n_{A \rightarrow B} e^{\beta(W - \Delta F_{AB})}} \right\rangle_{A \rightarrow B} = \left\langle \frac{1}{n_{A \rightarrow B} + n_{B \rightarrow A} e^{\beta(W + \Delta F_{AB})}} \right\rangle_{B \rightarrow A}, \quad (4.25)$$

where the path-ensemble averages of the  $A \rightarrow B$  and  $B \rightarrow A$  processes are made on  $n_{A \rightarrow B}$  and  $n_{B \rightarrow A}$  trajectories, respectively. Finally, CFT-based free energy estimators exploiting sets of trajectories performed in both directions of a process have also been devised to compute the PMF connecting two states along established collective coordinates[35, 36, 137]. All the reported Nonequilibrium Work theorems (eqs. 4.22, 4.23, 4.24, 4.25), deduced here in a constant volume NVT ensemble context, are valid also in a constant pressure NPT case. In such a case, NWTs relate Gibbs free energy variation  $\Delta G$  with non expansive work  $W$  distribution of a nonequilibrium process.

---

## Nonequilibrium work theorems applied to transitions between configurational domains

---

### 5.1 Introduction

The Potential of Mean Force (PMF)  $F(\lambda)$  is the free energy associated to  $\mathcal{D}_\lambda$ , *i.e.* a configurational subdomain of phase space  $\mathcal{D}$  of the microstates  $\mathbf{x}$ , identified by the constraining equation:

$$\mathcal{D}_\lambda = \{\mathbf{x} \in \mathcal{D} \mid \xi(\mathbf{x}) = \lambda\}. \quad (5.1)$$

For example, in steered molecular dynamics (SMD) simulations[151], though the microstates are located in the whole phase space  $\mathcal{D}$ , the introduction of a stiff external potential restrains the system to move with a defined value of the collective coordinate ( $\xi(\mathbf{x}) = \lambda$ ) and hence within the phase-space subdomain  $\mathcal{D}_\lambda$ . During a realization of the nonequilibrium process, the parameter  $\lambda$  evolves in time according to a prescribed time schedule  $\lambda(t)$ , guiding the evolution of the collective coordinate itself and, more generally, of the phase-space subdomain  $\mathcal{D}_\lambda$ . As deduced in the previous sec. 4, from work performed along an ensemble of tra-

jectories whose starting states are sampled in equilibrium conditions, Nonequilibrium Work Theorems (NWTs) allow to recover the PMF as a function of the collective coordinate  $\xi(\mathbf{x})$ , assuming the stiff spring approximation[151] or making use of reweighting techniques[79]. The previous reasoning can readily be extended to a system featured by a multidimensional space of collective coordinates. In any case, by using the Jarzynski equality (JE)[106] we are limited to evaluate the PMF along monodimensional paths designed in such a multidimensional space. Analogously, the CFT[50] provides free energy differences between states defined for specific points of the collective-coordinate space. The main purpose of this study is to introduce a generalized formulation of the JE and CFT that allows to perform calculations of free energy differences between phase-space domains in which the collective coordinate is constrained within an established volume, or hypersurface, of the collective-coordinate space, rather than to simple points. In principle, the PMF can also be obtained as a function of a path consisting of a continuous sequence of subspaces of the multidimensional collective-coordinate space. This formulation of the nonequilibrium work theorems is not alternative to the “classical” one[50, 106], but it includes the latter as a special case. Thus, the spectrum of applicability of the JE and CFT is extended to processes that involve thermodynamic states more general than those identified by eq. 5.1. The time evolution of the collective coordinate  $\xi(\mathbf{x})$  is limited to paths lying within an established subspace, whose size and shape can change during the nonequilibrium process. Assuming to deal with a monodimensional collective coordinate, at a given time  $t$ , the phase-space subdomain can be represented as

$$\mathcal{D}_t = \{\mathbf{x} \in \mathcal{D} \mid \lambda_1(t) \leq \xi(\mathbf{x}) = \lambda(t; \xi(\mathbf{x}_0)) \leq \lambda_2(t)\}. \quad (5.2)$$

A mapping  $\lambda(t; \xi(\mathbf{x}_0))$  is established at time  $t$  for  $\xi(\mathbf{x})$ , within the interval  $(\lambda_1(t), \lambda_2(t))$  (the subspace of  $\xi(\mathbf{x})$  at that time). A different  $\xi(\mathbf{x})$  value is externally imposed for different paths, according to the value of the collective coordinate at the initial time, *i.e.*  $\xi(\mathbf{x}_0)$ . This is the reason why, in eq. 5.2, we make explicit the parametric dependence of  $\lambda(t; \xi(\mathbf{x}_0))$  on  $\xi(\mathbf{x}_0)$ . Therefore, a path starting from the initial microstate  $\mathbf{x}_0$ , sampled at equilibrium under the condition  $\lambda_1(0) \leq \xi(\mathbf{x}_0) \leq \lambda_2(0)$ , is realized constraining  $\xi(\mathbf{x})$  to take a value in accord with the time dependent mapping  $\lambda(t; \xi(\mathbf{x}_0))$ , such that  $\lambda(0; \xi(\mathbf{x}_0)) = \xi(\mathbf{x}_0)$ . In designing the mapping for  $\xi(\mathbf{x})$ , a proper definition of work is deduced. We will show that the usual expression of mechanical work, as employed in standard SMD simulations, can be re-

covered in the limit  $\lambda_1(t) = \lambda_2(t) = \lambda(t)$ . As stated above, according to eq. 5.2, the present approach allows to estimate free energy differences associated with specific subspaces, rather than points, of the collective-coordinate space. This strategy can result particularly useful when a multidimensional collective coordinate is considered and the free energy difference of interest is that related to two basins of the hypersurface of the collective coordinate[82, 209]. In such cases, in fact, the standard approach of restraining the collective coordinate to a specific path along its hypersurface would not lead to free energy differences between the multidimensional configurational states (basins of the hypersurface), but rather to free energy differences between the initial and final points of the path designed on the hypersurface (see, *e.g.*, Ref.[82]). We point out that the present approach is rather general and the evolution of the collective coordinate may occur not only in a deterministic way as assumed above, but also according to a stochastic kernel. Therefore, in order to adhere to the general applicability of the method, in the treatment of sec. 5.2, the transition kernel will be expressed as a generic transition matrix. We will provide explicit expressions in the case studies reported in sec. 5.3. The switching scheme we are discussing about, that we may define Configurational-Domains Transition Scheme (CDTS), traces the concept of perturbation kernel, employed by Nilmeier and coworkers in performing nonequilibrium candidate Monte Carlo (NCMC) simulations[85, 147]. This technique is based on guided nonequilibrium trajectories between configurational domains separated by high energy barriers. The produced nonequilibrium candidate moves are accepted according to a criterion that preserves the balance conditions, involving the work associated with the transition paths. If NCMC is designed as a scheme to achieve a global sampling of the system[147], we instead show how to extend, through analogous algorithms, the JE and CFT analysis to ensembles of paths connecting separate phase-space subsets. We remark that the prime aim is to outline the novel theoretical development of the nonequilibrium work theorems under study and to provide a numerical validation of the method through the comparison with the standard technique employed for such a type of calculations, *i.e.*, SMD simulations. To this purpose, we limit the numerical tests to simple monodimensional collective-coordinate spaces. In particular the CDTS is verified by computing the free energy difference between configurational domains related to a Brownian particle moving into a double-well potential and to a two-particles dimer solvated by a Lennard-Jones fluid (sec. 5.3). Furthermore, it is important to notice that we do not pretend to prove here the superiority of CDTS with

respect to standard SMD, but only to establish the correctness of our theoretical outcomes in recovering free energy differences between given subspaces of the collective-coordinate space. Indeed, if we are interested to free energy differences between subspaces defined as intervals along a monodimensional path in a collective-coordinate space, as in our tests, the SMD approach would appear more performing than CDTS. On the other side, using monodimensional paths is the only way to carry out a fair comparison between CDTS and SMD. Nevertheless, there are important situations in which only CDTS can be applied. This aspect is widely discussed in sec. 5.3.3, where concluding remarks are also given.

## 5.2 Theory

### 5.2.1 Configurational-Domains Transition scheme (CDTS)

Given a system evolving in the phase space  $\mathcal{D}$ , we are interested in evaluating the relative stability (free energy difference) of two thermodynamic states identified by specific subdomains of  $\mathcal{D}$ , possibly, but not necessarily[1], defined through one or more order parameters. To this aim, we connect the states of interest,  $A$  and  $B$ , by a switching protocol that drives the system through an arbitrary sequence of intermediate configurational subdomains. A generic path from  $A$  to  $B$  is produced by a Markovian evolution scheme, which preserves proper balance conditions designed to enforce the validity of nonequilibrium work theorems. The states  $A$  and  $B$ , located in generic subdomains  $\mathcal{D}_A$  and  $\mathcal{D}_B$  of  $\mathcal{D}$ , are described by the dimensionless Hamiltonians  $\mathcal{H}_A(\mathbf{x})$  and  $\mathcal{H}_B(\mathbf{x})$ , associated with the non-normalized probability distributions  $\rho_A(\mathbf{x})$  and  $\rho_B(\mathbf{x})$ . Let us consider a stochastic process consisting of a finite or infinite number of steps, generating a trajectory  $\Gamma$  in the phase space  $\mathcal{D}$ , starting from the microstate  $\mathbf{x}_0$  and ending in the microstate  $\mathbf{x}_N$ . A generic intermediate microstate  $\mathbf{x}_i$  is sampled in the subdomain  $\mathcal{D}_i$  of  $\mathcal{D}$ , characterized by the Hamiltonian  $\mathcal{H}_i(\mathbf{x})$ , and hence by the underlying non-normalized probability distribution  $\rho_i(\mathbf{x}_i) = e^{-\mathcal{H}_i(\mathbf{x}_i)}$ . In the expression of  $\mathcal{H}_i(\mathbf{x}_i)$ , the explicit dependence on time can lie in an (extended) Hamiltonian through some mechanical control parameter, introduced to simultaneously change appropriate collective coordinates (interatomic distances, torsion angles, volume, coordination numbers, etc.), or through thermostat and/or barostat inertial factors, or also in the inverse temperature  $\beta_i$  of an external bath[26]. The initial microstate  $\mathbf{x}_0$  is sampled into  $\mathcal{D}_0 \equiv \mathcal{D}_A$ , according to

the normalized probability distribution

$$p_A(\mathbf{x}_0) = \rho_A(\mathbf{x}_0)/Q_A, \quad (5.3)$$

where  $Q_A = \int_{\mathcal{D}_A} d\mathbf{x} \rho_A(\mathbf{x})$  is the partition function of the state  $A$ . Moreover, the final state coincides with the state  $B$ , namely  $\mathcal{D}_N \equiv \mathcal{D}_B$ , and hence  $\mathcal{H}_N(\mathbf{x}_N) \equiv \mathcal{H}_B(\mathbf{x}_N)$ . We point out that the trajectory  $\Gamma$  consists of a sequence of  $N$  transitions between arbitrary subdomains of  $\mathcal{D}$ , *i.e.*,  $\mathcal{D}_0 \rightarrow \mathcal{D}_1 \rightarrow \dots \rightarrow \mathcal{D}_N$ . Only a single protocol has to be designed to establish the sequence of domains visited along the trajectory. In analogy with the NCMC simulation scheme[147], each step of the trajectory is produced in two phases. A domain-transition move, switching the system from  $\mathcal{D}_i$  to  $\mathcal{D}_{i+1}$ , is alternated with one move of the type  $\mathbf{x}_i \rightarrow \mathbf{x}'_i$ , realized in the domain  $\mathcal{D}_i$  according to a relaxation kernel  $S(\mathbf{x}_i \rightarrow \mathbf{x}'_i) \geq 0$ , such that  $\int_{\mathcal{D}_i} d\mathbf{x}'_i S(\mathbf{x}_i \rightarrow \mathbf{x}'_i) = 1$ . Relaxation moves are targeted to reduce the dissipated work accumulated during the transition moves, ultimately enhancing the accuracy of thermodynamic estimates realized in a finite number of steps[88]. These moves are performed by enforcing the detailed balance condition (cf. eq. 4.15)

$$\rho_i(\mathbf{x}_i) S(\mathbf{x}_i \rightarrow \mathbf{x}'_i) = \rho_i(\mathbf{x}'_i) S(\mathbf{x}'_i \rightarrow \mathbf{x}_i). \quad (5.4)$$

It is obvious that more relaxation moves can take place before a transition move, but, for the sake of simplicity, only one relaxation move will be considered in the current treatment. After the relaxation step, a  $\mathbf{x}'_i \rightarrow \mathbf{x}_{i+1}$  move, leading from  $\mathcal{D}_i$  to  $\mathcal{D}_{i+1}$ , takes place under the established transition kernel  $T(\mathbf{x}'_i \rightarrow \mathbf{x}_{i+1}) \geq 0$ . Again, we require the probability of reaching whatever microstate of  $\mathcal{D}_{i+1}$ , moving from a given  $\mathbf{x}'_i \in \mathcal{D}_i$  to be normalized, namely  $\int_{\mathcal{D}_{i+1}} d\mathbf{x}_{i+1} T(\mathbf{x}'_i \rightarrow \mathbf{x}_{i+1}) = 1$ . We can now give the following definition of transition distribution:

$$\tau_i(\mathbf{x}_i) = \int_{\mathcal{D}_{i-1}} d\mathbf{x}_{i-1} \rho_{i-1}(\mathbf{x}_{i-1}) T(\mathbf{x}_{i-1} \rightarrow \mathbf{x}_i). \quad (5.5)$$

$\tau_i(\mathbf{x}_i)$  is a statistical weight proportional to the probability of reaching the microstate  $\mathbf{x}_i \in \mathcal{D}_i$ , moving under the transition kernel  $T(\mathbf{x}_{i-1} \rightarrow \mathbf{x}_i)$  from any microstate  $\mathbf{x}_{i-1} \in \mathcal{D}_{i-1}$ , sampled according to  $\rho_{i-1}(\mathbf{x}_{i-1})$ . We note that, by integration,  $\tau_i(\mathbf{x}_i)$  gives the partition function related to the Hamiltonian  $\mathcal{H}_{i-1}(\mathbf{x})$ :

$$\int_{\mathcal{D}_i} d\mathbf{x} \tau_i(\mathbf{x}) = \int_{\mathcal{D}_{i-1}} d\mathbf{x} \rho_{i-1}(\mathbf{x}) = Q_{i-1}. \quad (5.6)$$

Let us consider the trajectory  $\Gamma^*$ , reverse to  $\Gamma$ , whose initial microstate is assumed to be sampled in the domain  $\mathcal{D}_B$ , according to the equilibrium probability distribution  $p_B(\mathbf{x}) = \rho_B(\mathbf{x})/Q_B$  (cf. eq. 5.3). A new detailed balance condition is imposed to the moves of the bidirectional process,

$$\rho_i(\mathbf{x}'_i) T(\mathbf{x}'_i \rightarrow \mathbf{x}_{i+1}) = \tau_{i+1}(\mathbf{x}_{i+1}) T^*(\mathbf{x}_{i+1} \rightarrow \mathbf{x}'_i), \quad (5.7)$$

relating the reverse transition kernel  $T^*(\mathbf{x}_{i+1} \rightarrow \mathbf{x}'_i)$  to the transition distributions  $\tau_{i+1}(\mathbf{x}_{i+1})$  associated with the  $\Gamma$  path. Through integration of eq. 5.7 over the domain  $\mathcal{D}_i$ , it is straightforward to verify that, consistently with the definition of transition kernel,  $T^*(\mathbf{x}_{i+1} \rightarrow \mathbf{x}'_i)$  is normalized, *i.e.*,  $\int_{\mathcal{D}_i} d\mathbf{x}'_i T^*(\mathbf{x}_{i+1} \rightarrow \mathbf{x}'_i) = 1$ . Of course, as there is no reason to take the  $\Gamma$  path as the reference for the transition distributions, an analogous reasoning can be applied to the reverse path  $\Gamma^*$ . In such a case, the detailed balance condition of eq. 5.7 would read as

$$\tau_i^*(\mathbf{x}'_i) T(\mathbf{x}'_i \rightarrow \mathbf{x}_{i+1}) = \rho_{i+1}(\mathbf{x}_{i+1}) T^*(\mathbf{x}_{i+1} \rightarrow \mathbf{x}'_i). \quad (5.8)$$

Integration of eq. 5.8 over the domain  $\mathcal{D}_{i+1}$  allows to recover the transition distribution  $\tau_i^*(\mathbf{x}'_i)$  consistent with the distribution in the  $\Gamma$  path (eq. 5.5)

$$\tau_i^*(\mathbf{x}'_i) = \int_{\mathcal{D}_{i+1}} d\mathbf{x}_{i+1} \rho_{i+1}(\mathbf{x}_{i+1}) T^*(\mathbf{x}_{i+1} \rightarrow \mathbf{x}'_i). \quad (5.9)$$

### 5.2.2 Crooks fluctuation theorem under CDTS

The CDTS described in sec. 5.2.1 is based on a sequence of relaxation and domain-transition moves satisfying the detailed balance conditions of eqs. 5.4 and 5.7, respectively. In this section, we show how these conditions allow to formulate a more general expression of the CFT. The derivation traces sec. 4.3, and the treatment described by Crooks in ref.[48]. Specifically, the switching process is assumed to occur in two steps consisting of a perturbation move (transition kernel) and a relaxation move (relaxation kernel). We start observing that the ratio between the probability  $P_{A \rightarrow B}[\Gamma]$  of generating the trajectory  $\Gamma$  in the  $A \rightarrow B$  process, and the probability  $P_{B \rightarrow A}[\Gamma^*]$  of generating the trajectory  $\Gamma^*$  in a time reverse process  $B \rightarrow A$  (both trajectories starting from microstates sampled at equilibrium), is given by the equation

$$\frac{P_{A \rightarrow B}[\Gamma]}{P_{B \rightarrow A}[\Gamma^*]} = \frac{p_A(\mathbf{x}_0)}{p_B(\mathbf{x}_N)} \prod_{i=0}^{N-1} \frac{S(\mathbf{x}_i \rightarrow \mathbf{x}'_i) T(\mathbf{x}'_i \rightarrow \mathbf{x}_{i+1})}{S(\mathbf{x}'_i \rightarrow \mathbf{x}_i) T^*(\mathbf{x}_{i+1} \rightarrow \mathbf{x}'_i)}. \quad (5.10)$$



Exploiting eqs. 5.4 and 5.7, together with eq. 5.3 for  $p_A(\mathbf{x}_0)$  (and the analogous relationship  $p_B(\mathbf{x}_N) = \rho_B(\mathbf{x}_N)/Q_B$ ), we obtain

$$\frac{P_{A \rightarrow B}[\Gamma]}{P_{B \rightarrow A}[\Gamma^*]} = \frac{Q_B \rho_A(\mathbf{x}_0)}{Q_A \rho_B(\mathbf{x}_N)} \prod_{i=0}^{N-1} \frac{\tau_{i+1}(\mathbf{x}_{i+1})}{\rho_i(\mathbf{x}_i)} = \frac{Q_B}{Q_A} \prod_{i=1}^N \frac{\tau_i(\mathbf{x}_i)}{\rho_i(\mathbf{x}_i)}, \quad (5.11)$$

where the equivalences  $\rho_0(\mathbf{x}_0) \equiv \rho_A(\mathbf{x}_0)$  and  $\rho_N(\mathbf{x}_N) \equiv \rho_B(\mathbf{x}_N)$  have been used in going from the middle to the right term of the equation. From eq. 5.11, we derive a fundamental expression, involving the dimensionless free energy difference  $\Delta\mathcal{F}_{AB} = -\ln(Q_B/Q_A)$  between the states  $A$  and  $B$

$$\frac{P_{A \rightarrow B}[\Gamma]}{P_{B \rightarrow A}[\Gamma^*]} = e^{\mathcal{W}_{A \rightarrow B}[\Gamma] - \Delta\mathcal{F}_{AB}}. \quad (5.12)$$

Accounting for the ratio between transition and equilibrium distributions relative to microstates collected along the trajectory, we have introduced the generalized dimensionless work,

$$\mathcal{W}_{A \rightarrow B}[\Gamma] = \ln \left( \prod_{i=1}^N \frac{\tau_i(\mathbf{x}_i)}{\rho_i(\mathbf{x}_i)} \right). \quad (5.13)$$

In order to verify that the definition of work provided by eq. 5.13 coherently extends the concept of mechanical work to transitions between general configurational domains, we derive the expression obtained by using eq. 5.13 if  $\mathcal{D}_i \equiv \mathcal{D}_{i+1}$  for each step  $i$  of the path. To this aim, let us identify the stationary non-normalized probability distribution at the  $i$ -th step with the canonical one, *i.e.*,  $\rho_i(\mathbf{x}) = e^{-\beta H_i(\mathbf{x})}$ , at fixed inverse temperature  $\beta$ . As no transition between different domains takes place, the generic transition kernel  $T(\mathbf{x}_{i-1} \rightarrow \mathbf{x}_i)$  reduces to an identity function, *i.e.*,  $T(\mathbf{x}_{i-1} \rightarrow \mathbf{x}_i) = \delta(\mathbf{x}_i - \mathbf{x}_{i-1})$ . Under this condition, eq. 5.5 becomes  $\tau_i(\mathbf{x}_i) = \rho_{i-1}(\mathbf{x}_i)$ , which, substituted into eq. 5.13, gives

$$\mathcal{W}_{A \rightarrow B}[\Gamma] = \ln \left( \prod_{i=1}^N \frac{\rho_{i-1}(\mathbf{x}_i)}{\rho_i(\mathbf{x}_i)} \right) = \beta \sum_{i=1}^N [H_i(\mathbf{x}_i) - H_{i-1}(\mathbf{x}_i)]. \quad (5.14)$$

In eq. 5.14, the generic term in the sum corresponds to the work performed on the system to switch the Hamiltonian from  $H_{i-1}(\mathbf{x}_i)$  to  $H_i(\mathbf{x}_i)$  at fixed configuration. The sum over all the switching steps provides the total work  $W_{A \rightarrow B}[\Gamma]$  performed during the  $\Gamma$  path. We may therefore recognize the identity  $\mathcal{W}_{A \rightarrow B}[\Gamma] = \beta W_{A \rightarrow B}[\Gamma]$ , which, substituted into eq. 5.12, gives the well-known form of the CFT[48, 50].

We notice that  $\mathcal{W}_{A \rightarrow B}[\Gamma]$  depends on the ratio between  $\tau_i(\mathbf{x}_i)$  and  $\rho_i(\mathbf{x}_i)$ , where  $\mathbf{x}_i$  is the microstate reached upon applying the transition kernel  $T(\mathbf{x}'_{i-1} \rightarrow \mathbf{x}_i)$  leading from the domain  $\mathcal{D}_{i-1}$  to the domain  $\mathcal{D}_i$  (assuming  $\mathbf{x}'_{i-1}$  sampled according to  $\rho_{i-1}(\mathbf{x}'_{i-1})$ ). For each transition move  $i$ , the occurrence of  $\tau_i(\mathbf{x}_i)/\rho_i(\mathbf{x}_i) > Q_{i-1}/Q_i$  will enhance the dissipation associated with the path. On the contrary, an anti-dissipative contribution will arise from  $\tau_i(\mathbf{x}_i)/\rho_i(\mathbf{x}_i) < Q_{i-1}/Q_i$ .

Alternatively to the previous approach, we can use eq. 5.8 into eq. 5.10 to get

$$\frac{P_{A \rightarrow B}[\Gamma]}{P_{B \rightarrow A}[\Gamma^*]} = \frac{Q_B}{Q_A} \prod_{i=0}^{N-1} \frac{\rho_i(\mathbf{x}'_i)}{\tau_i^*(\mathbf{x}'_i)}. \quad (5.15)$$

In analogy with eq. 5.13, the generalized dimensionless work for the reverse  $\Gamma^*$  path is

$$\mathcal{W}_{B \rightarrow A}[\Gamma^*] = \ln \left( \prod_{i=0}^{N-1} \frac{\tau_i^*(\mathbf{x}'_i)}{\rho_i(\mathbf{x}'_i)} \right). \quad (5.16)$$

Also in this case,  $\mathbf{x}'_i$  is the microstate reached upon applying the transition kernel leading from the domain  $\mathcal{D}_{i+1}$  to the domain  $\mathcal{D}_i$ , specifically  $T^*(\mathbf{x}_{i+1} \rightarrow \mathbf{x}'_i)$ . Combining eqs. 5.15 and 5.16, allows to recover the relationship

$$\frac{P_{A \rightarrow B}[\Gamma]}{P_{B \rightarrow A}[\Gamma^*]} = e^{-\mathcal{W}_{B \rightarrow A}[\Gamma^*] - \Delta \mathcal{F}_{AB}}. \quad (5.17)$$

From the ratio between eqs. 5.7 and 5.8, it is easy to show that  $\mathcal{W}_{B \rightarrow A}[\Gamma^*] = -\mathcal{W}_{A \rightarrow B}[\Gamma]$ , and hence the equivalence between the relationships 5.12 and 5.17.

From the generalized CFT of eq. 5.12, it is possible to operate an equivalent extension of the NWTs reported in sec. 4.4. The mechanical work  $\beta W$  is directly substituted by the generalized work  $\mathcal{W}$ .

### 5.2.3 CDTS under deterministic dynamics

Molecular dynamics simulations based on deterministic laws of motion are particularly suited for being supplemented with the CDTS. In agreement with the treatment of Secs. 5.2.1 and 5.2.2, we observe that a deterministic dynamics can be thought as a sequence of  $N$  transitions  $\mathbf{x}_i \rightarrow \mathbf{x}'_i \rightarrow \mathbf{x}_{i+1}$ , with  $\mathbf{x}_i, \mathbf{x}'_i \in \mathcal{D}_i$  and  $\mathbf{x}_{i+1} \in \mathcal{D}_{i+1}$ . Transition moves correspond to the dynamics of externally controlled degrees of freedom, realized under a

flux function  $\mathbf{x}_{i+1} = \Phi_{i \rightarrow i+1}(\mathbf{x}'_i)$ , connecting in a bijective manner  $\mathbf{x}'_i$  in the domain  $\mathcal{D}_i$  to  $\mathbf{x}_{i+1}$  in the domain  $\mathcal{D}_{i+1}$ . Hence, the transition kernel corresponds to the Dirac delta function  $T(\mathbf{x}'_i \rightarrow \mathbf{x}_{i+1}) = \delta(\mathbf{x}_{i+1} - \Phi_{i \rightarrow i+1}(\mathbf{x}'_i))$ . Relaxation kernel is also given by a Dirac delta function  $S(\mathbf{x}_i \rightarrow \mathbf{x}'_i) = \delta(\mathbf{x}'_i - \Phi_{i \rightarrow i}(\mathbf{x}_i))$ , consisting in the dynamics of uncontrolled degrees of freedom. The bijective flux function  $\mathbf{x}'_i = \Phi_{i \rightarrow i}(\mathbf{x}_i)$  links the microstates  $\mathbf{x}'_i$  and  $\mathbf{x}_i$  into the domain  $\mathcal{D}_i$ . Exploiting the definition of  $\tau_i(\mathbf{x}_i)$  (eq. 5.5) and the expressions of the transition matrices  $S(\mathbf{x}_i \rightarrow \mathbf{x}'_i)$  and  $T(\mathbf{x}'_i \rightarrow \mathbf{x}_{i+1})$  reported above (together with the properties of the Dirac delta function), it can be shown that

$$\frac{\rho_i(\mathbf{x}_i)}{\tau_{i+1}(\mathbf{x}_{i+1})} = |J_{\Phi_{i \rightarrow i}}(\mathbf{x}_i) J_{\Phi_{i \rightarrow i+1}}(\mathbf{x}'_i)|, \quad (5.18)$$

where  $J_{\Phi_{i \rightarrow i}}(\mathbf{x}_i)$  and  $J_{\Phi_{i \rightarrow i+1}}(\mathbf{x}'_i)$  are the Jacobian determinants, associated with the flux functions  $\Phi_{i \rightarrow i}(\mathbf{x})$  and  $\Phi_{i \rightarrow i+1}(\mathbf{x})$ , computed into  $\mathbf{x}_i$  and  $\mathbf{x}'_i$ , respectively. Since the trajectory  $\Gamma$  is completely determined by the initial configuration of the system, the work can be expressed as a function of the initial microstate  $\mathbf{x}_0$ , namely  $\mathcal{W}_{A \rightarrow B}[\Gamma] \equiv \mathcal{W}_{A \rightarrow B}(\mathbf{x}_0)$ . The generalized dimensionless work takes the form of eq. 5.13 and can be written as

$$\begin{aligned} \mathcal{W}_{A \rightarrow B}(\mathbf{x}_0) &= \ln \left( \prod_{i=0}^{N-1} \frac{\tau_{i+1}(\mathbf{x}_{i+1})}{\rho_{i+1}(\mathbf{x}_{i+1})} \right) \\ &= \ln \frac{\rho_A(\mathbf{x}_0)}{\rho_B(\mathbf{x}_N)} - \ln |J_{\Phi_{0 \rightarrow N}}(\mathbf{x}_0)|, \end{aligned} \quad (5.19)$$

where  $J_{\Phi_{0 \rightarrow N}}(\mathbf{x}_0) = \prod_{i=0}^{N-1} J_{\Phi_{i \rightarrow i}}(\mathbf{x}_i) J_{\Phi_{i \rightarrow i+1}}(\mathbf{x}'_i)$  is the Jacobian determinant of the flux function  $\Phi_{0 \rightarrow N}(\mathbf{x}_0)$ , relating the final microstate  $\mathbf{x}_N$  to the initial microstate  $\mathbf{x}_0$ . In order to simplify the discussion, we note that, while the initial microstates can be sampled according to non-Hamiltonian dynamics, as in constant-volume constant-temperature (NVT) simulations, the nonequilibrium trajectories can be performed adopting Hamiltonian laws of motion, typical of constant-volume constant-energy (NVE) simulations. Hence, in the nonequilibrium trajectories, the infinitesimal phase-space volume is conserved during the evolution of the uncontrolled degrees of freedom (the dynamics under the relaxation kernel) and hence the associated Jacobian,  $J_{\Phi_{i \rightarrow i}}(\mathbf{x}_i)$ , holds 1. Thus, only the transition moves contribute to the global Jacobian determinant, *i.e.*,  $J_{\Phi_{0 \rightarrow N}}(\mathbf{x}_0) = \prod_{i=0}^{N-1} J_{\Phi_{i \rightarrow i+1}}(\mathbf{x}'_i)$ . From the physical point of view, the change in dynamical laws from NVT to NVE-type corresponds to an instantaneous break of energy exchange between system and thermostat. This

approach is dated back to the work of Jarzynski[107], who showed that an instantaneous detachment of the thermal bath from a system subject to pulling processes does not affect the free energy estimates obtained by eq. 4.23. The scheme was later applied to a simulation study in Ref.[142]. Under canonical sampling conditions, we have shown that  $\mathcal{W}_{A \rightarrow B}(\mathbf{x}_0) = \beta W_{A \rightarrow B}(\mathbf{x}_0)$  and  $\rho_i(\mathbf{x}_i) = e^{-\beta H_i(\mathbf{x}_i)}$  (see eq. 5.14 and related discussion). Equation 5.19 can therefore be written as

$$W_{A \rightarrow B}(\mathbf{x}_0) = H_B(\mathbf{x}_N) - H_A(\mathbf{x}_0) - \beta^{-1} \ln |J_{\Phi_0 \rightarrow N}(\mathbf{x}_0)|. \quad (5.20)$$

Comparing eq. 5.20 with the first law of thermodynamics, we can identify  $\beta^{-1} \ln |J_{\Phi_0 \rightarrow N}(\mathbf{x}_0)|$  with the heat entering the system during the  $\mathbf{x}_0 \rightarrow \mathbf{x}_N$  path.

## 5.3 Numerical Tests

### 5.3.1 Systems and simulation details

Numerical validation of the CDTS is provided evaluating free energy differences between states defined in specific phase-space configurational domains for two systems: a Brownian particle moving into a double-well potential and a dimer immersed in a Lennard-Jones fluid. Switching processes between the target states have been realized under deterministic transition kernels (sec. 5.2.3), applying both instantaneous (Brownian particle case) and noninstantaneous (dimer case) changes of the externally controlled variables. The CDTS outcomes are compared to those obtained from standard SMD simulations.

#### Brownian particle

The system consists of a particle moving into a monodimensional space through overdamped Langevin dynamics[12], with unitary values of diffusion coefficient and inverse temperature  $\beta$  (dimensionless units are adopted). The motion is regulated by a double-well potential energy function,  $U(x) = 5(x^2 - 1)^2 + 3x$ , which corresponds to the PMF  $\mathcal{F}(x)$  (see fig. 5.1). Two minima at  $x \simeq \pm 1$  are separated by an energy barrier at  $x \simeq 0$ . The target states  $A$  and  $B$  are defined by subdomains  $\mathcal{D}_A$  and  $\mathcal{D}_B$  of the phase-space  $\mathcal{D} = \{x \in \mathcal{D} \mid -\infty < x < \infty\}$ , such that  $\mathcal{D}_A = \{x \in \mathcal{D} \mid \lambda_A^{(1)} \leq x \leq \lambda_A^{(2)}\}$  and

$\mathcal{D}_B = \{x \in \mathcal{D} \mid \lambda_B^{(1)} \leq x \leq \lambda_B^{(2)}\}$ , where  $\lambda_S^{(n)}$  are established boundaries. The free energies associated with the states  $A$  and  $B$  are

$$\mathcal{F}_S = -\ln \left( \int_{\lambda_S^{(1)}}^{\lambda_S^{(2)}} dx e^{-\mathcal{F}(x)} \right) \quad S \equiv A, B \quad (5.21)$$

which are computed by numerical integration. This provides the reference values for  $\Delta\mathcal{F}_{AB} = \mathcal{F}_B - \mathcal{F}_A$ . Various free energy calculations differing in size and position of the  $\mathcal{D}_A$  and  $\mathcal{D}_B$

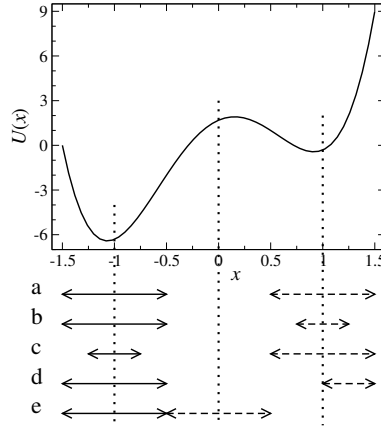


**Figure 5.1:** Double-well potential energy  $U(x)$  as a function of  $x$  for the Brownian particle (dimensionless units). Domains  $\mathcal{D}_A$  and  $\mathcal{D}_B$  featuring the states  $A$  and  $B$  are shown with full and dashed-line arrows, respectively, according to the following boundary definitions of the type  $[\lambda_A^{(1)}, \lambda_A^{(2)}; \lambda_B^{(1)}, \lambda_B^{(2)}]$ .  $a = [-1.5, -0.5; 0.5, 1.5]$ ,  $b = [-1.5, -0.5; 0.75, 1.25]$ ,  $c = [-1.25, -0.75; 0.5, 1.5]$ ,  $d = [-1.5, -0.5; 1.0, 1.5]$ ,  $e = [-1.5, -0.5; -0.5, 0.5]$ .

domains have been performed. A graphical representation of these domains is reported in fig. 5.1, with the numerical definitions given in the caption. Case (a) corresponds to domains of equal size, centered, in turn, on one energy minimum. Cases (b), (c) and (d) refer to domains with different size (in the case (d), the  $\mathcal{D}_B$  domain is not centered on the minimum). In the case (e), the  $\mathcal{D}_B$  domain is located around the maximum of the energy barrier. A single transition move  $T(x_A \rightarrow x_B)$  is enforced to switch deterministically the particle from

the  $\mathcal{D}_A$  to the  $\mathcal{D}_B$  domain. This approach strongly resembles the free energy perturbation method[211], in which the system is sampled at equilibrium in a reference state and the free energy between this state and a target one is computed through the difference between the Hamiltonians of the two states computed in the configuration of the reference state. In fact, free energy perturbation can be viewed as an instantaneous switching of a control parameter associated with a work corresponding to the difference between the Hamiltonians in the target and reference states. Within this picture, the JE and the free energy perturbation relationship are equivalent. The flux function  $\phi_{A \rightarrow B}(x_A)$  associated with this transition move is linear,

$$\phi_{A \rightarrow B}(x_A) = x_B = \frac{\lambda_B^{(2)} - \lambda_B^{(1)}}{\lambda_A^{(2)} - \lambda_A^{(1)}} x_A + \frac{\lambda_A^{(2)} \lambda_B^{(1)} - \lambda_B^{(2)} \lambda_A^{(1)}}{\lambda_A^{(2)} - \lambda_A^{(1)}}, \quad (5.22)$$

where  $x_A \in \mathcal{D}_A$  and  $x_B \in \mathcal{D}_B$ . On the basis of eq. 5.19, and considering that the Jacobian of the transformation is

$$J_{\phi_{A \rightarrow B}}(x_A) = \frac{\partial x_B}{\partial x_A} = \frac{\lambda_B^{(2)} - \lambda_B^{(1)}}{\lambda_A^{(2)} - \lambda_A^{(1)}}, \quad (5.23)$$

the work performed on the system in a (instantaneous) switching realization is

$$\mathcal{W}_{A \rightarrow B}(x_A) = U(\phi_{A \rightarrow B}(x_A)) - U(x_A) - \ln \left| \frac{\lambda_B^{(2)} - \lambda_B^{(1)}}{\lambda_A^{(2)} - \lambda_A^{(1)}} \right|. \quad (5.24)$$

The formal equivalence between CDTS enforced with instantaneous switching and the free energy perturbation method is highlighted by identifying the transition  $x \rightarrow \phi_{A \rightarrow B}(x)$  with a change of the potential energy at fixed configuration  $x$ . Indeed, the free energy perturbation relationship,  $e^{-\Delta \mathcal{F}_{AB}} = \langle e^{V_A(x) - V_B(x)} \rangle_A$ , is recovered if the potential energies in the reference and target states ( $V_A(x)$  and  $V_B(x)$ ) are identified with  $U(x)$  and  $U(\phi_{A \rightarrow B}(x)) - \ln |J_{\phi_{A \rightarrow B}}(x)|$ , respectively.

The initial microstates  $x_A$  of the realizations are picked during an overdamped Langevin simulation lasting 1000 time-units, being the time-step  $10^{-6}$  time-units. Since the initial microstates must belong to the  $\mathcal{D}_A$  domain, an additional restraining potential has been applied

$$\mathcal{V}(x) = \begin{cases} 50 (x - \lambda_A^{(1)})^2 & \text{if } x \leq \lambda_A^{(1)} \\ 0 & \text{if } \lambda_A^{(1)} \leq x \leq \lambda_A^{(2)} \\ 50 (x - \lambda_A^{(2)})^2 & \text{if } x \geq \lambda_A^{(2)}. \end{cases} \quad (5.25)$$

This potential allows for a substantial canonical sampling of the microstates of interest, for which  $\lambda_A^{(1)} \leq x \leq \lambda_A^{(2)}$ . Nevertheless, owing to the continuous behavior of the potential at the boundaries, a fraction of sampled microstates falls outside  $\mathcal{D}_A$ . However, because of the stiffness of the (harmonic) potential outside the boundaries, the amount of such microstates is negligible. In any case, they are rejected in the free energy calculation. The free energy difference between the  $\mathcal{D}_A$  and  $\mathcal{D}_B$  domains is calculated using the JE (eq. 4.23 and the Bennett-like estimator (eq. 4.25) in sec. 4.4).

### Dimer in a Lennard-Jones fluid

Numerical experiments with production of fast switching trajectories have been performed on a bistable dimer, immersed in a Lennard-Jones fluid. The dimer consists of two particles interacting through a double-well potential energy, dependent on the interparticle distance  $r$ :  $U_{\text{dim}}(r) = 3[(r-1)^2 - 0.1](r-3)^2$ . All quantities here, as well as in the following, are in reduced units. The potential energy  $U_{\text{dim}}(r)$ , plotted in fig. 5.2, has two minima at the distances  $r \simeq 1$  and  $r \simeq 3$ , corresponding to compact and extended configurations of the dimer, respectively. One dimer particle is fixed at the origin of the laboratory frame, whereas the other particle can move freely or according to a control parameter along the  $x$  axis (in dependence of the type of simulation is being performed; see later). The system is formed by 600 particles, including the dimer. The solute (dimer) and solvent particles have the same masses and evolve in a cubic simulation box with standard periodic boundary conditions. The Lennard-Jones potentials for solvent-solvent and solute-solvent interactions are identical and vanish in the distance range 3.0-3.5 through a cubic switching function. Equations of motion are integrated with a time-step of  $5 \cdot 10^{-3}$ . The particle density is fixed at the value of 0.85. As for the Brownian particle, free energy differences refer to domains of the type  $\mathcal{D}_S = \{x \in \mathcal{D} \mid \lambda_S^{(1)} \leq x \leq \lambda_S^{(2)}\}$ , with  $S \equiv A, B$ . The domains considered here (see fig. 5.2), have been selected using criteria similar to the Brownian-particle case.

Sampling of the initial microstates has been performed with two equilibrium NVT simulations (keeping the temperature at 0.8 by means of a Nosé-Hoover chain thermostat[193]) restraining the dimer distance within the domains  $\mathcal{D}_A$  and  $\mathcal{D}_B$  (for  $A \rightarrow B$  and  $B \rightarrow A$  realizations, respectively). Domain restraining has been achieved by adding a harmonic potential energy term identical to that of eq. 5.25, apart from the value of the potential constant, which is 5000 instead of 50. In both simulations 2000 microstates have been collected ev-

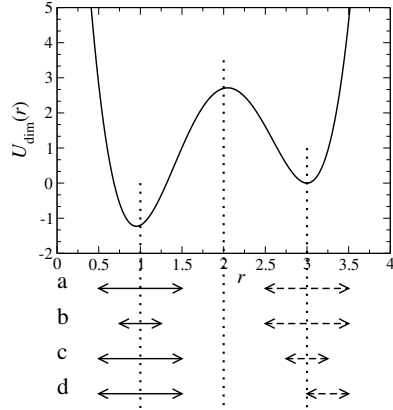


**Figure 5.2:** Double-well potential energy  $U_{\text{dim}}(r)$  as a function of the interparticle distance  $r$  (in reduced units), for a dimer immersed in a Lennard-Jones fluid. Domains  $\mathcal{D}_A$  and  $\mathcal{D}_B$  are shown with full and dashed-line arrows, respectively, according to the following boundary definitions of the type  $[\lambda_A^{(1)}, \lambda_A^{(2)}; \lambda_B^{(1)}, \lambda_B^{(2)}]$ .  $a = [0.5, 1.5; 2.5, 3.5]$ ,  $b = [0.75, 1.25; 2.5, 3.5]$ ,  $c = [0.5, 1.5; 2.75, 3.25]$ ,  $d = [0.5, 1.5; 3.0, 3.5]$ .

ery 0.5 time-units. Once the initial microstates are stored, nonequilibrium trajectories are realized. During each trajectory, the mobile dimer particle is externally driven along the  $x$ -axis from its initial position sampled at equilibrium, say  $x_A$  for the  $A \rightarrow B$  type process, according to the time-dependent component of the total flux function  $\mathbf{x}(t) = \Phi_{0 \rightarrow t}(\mathbf{x}(0))$ ,

$$\phi_{0 \rightarrow t}(x_A) = x(t) = \frac{\lambda^{(2)}(t) - \lambda^{(1)}(t)}{\lambda_A^{(2)} - \lambda_A^{(1)}} x_A + \frac{\lambda_A^{(2)} \lambda^{(1)}(t) - \lambda_A^{(1)} \lambda^{(2)}(t)}{\lambda_A^{(2)} - \lambda_A^{(1)}}. \quad (5.26)$$

The total flux function  $\Phi_{0 \rightarrow t}(\mathbf{x}(0))$  links, in a bijective manner, the microstate  $\mathbf{x}(t)$  of the whole system to the initial microstate  $\mathbf{x}(0)$  (see sec. 5.2.3). In eq. 5.26,  $\lambda^{(1)}(t) = \lambda_A^{(1)} + (\lambda_B^{(1)} - \lambda_A^{(1)}) t/\tau$ , with  $\tau$  being the (simulation) time of the switching process. An analogous expression is used for  $\lambda^{(2)}(t)$ . Note that the pulling trajectories occur with variable rates depending on the difference  $|x_A - \phi_{0 \rightarrow \tau}(x_A)|$ . Calculations with various simulation times have been carried out:  $\tau = 25, 50, 100$ . Moreover, the nonequilibrium trajectories



have been performed using NVE simulations. In these conditions, the contribution of the solute to the Jacobian determinant related to the whole trajectory is given by eq. 5.23, while solvent degrees of freedom give unitary contribution (as remarked in sec. 5.2.3, the NVE dynamics preserves the infinitesimal phase-space volume). Correspondingly, the total work is given by eq. 5.24, with  $U(x_A)$  and  $U(\phi_{A \rightarrow B}(x_A))$  being substituted by the initial and final total energies of the system, respectively.

Free energy differences between the  $\mathcal{D}_A$  and  $\mathcal{D}_B$  domains have been calculated according to eq. 4.25. Results are compared to those achieved from integrating the PMF profiles computed from standard SMD simulations performed in the same operative conditions, with only one significant difference. In SMD, the change of the dimer distance in going from the compact ( $\lambda_a = 0.4$ ) to the extended ( $\lambda_b = 3.6$ ) configuration, and viceversa, is enforced through a harmonic potential  $V(r, t) = 5000[r - \lambda(t)]^2$ , under the verified assumption that stiff spring approximation[151] holds. This implies that CDTS and SMD calculations have the same computational cost.

Finally, reference values of the free energy differences have been calculated from an accurate PMF, recovered by thermodynamic integration[116], exploiting a series of NVT molecular dynamics simulations lasting 200 time-units each. Profiles have been numerically integrated, with steps of  $5 \cdot 10^{-2}$  length units.

### 5.3.2 Results

#### Brownian particle

The free energy difference  $\Delta\mathcal{F}_{AB}$  between the  $\mathcal{D}_A$  and  $\mathcal{D}_B$  configurational domains defined in fig. 5.1 has been evaluated using both monodirectional (eq. 4.23) and bidirectional (eq. 4.25) free energy estimators. In fig. 5.3, we compare  $\Delta\mathcal{F}_{AB}$  computed through the CDTS to reference values, obtained by numerical integration of the PMF (eq. 5.21). Each value reported in the figure corresponds to an average of 100 independent  $\Delta\mathcal{F}_{AB}$  estimates obtained by configurations regularly sampled every 10 time-units from a simulation 1000 time-units long. The corresponding standard deviations are also reported in the figure as error bars. The data outline the almost perfect agreement between CDTS and the reference  $\Delta\mathcal{F}_{AB}$  values. In spite of the very small standard deviations, especially for the  $a$   $b$  and  $c$  cases, the deviations of the reference values from the CDTS ones are within the error bars.

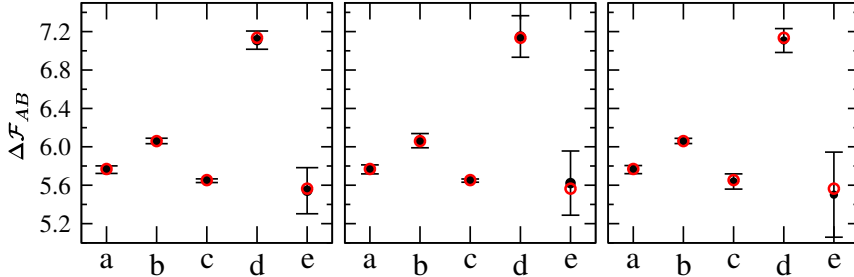


**Figure 5.3:** Dimensionless free energies  $\Delta\mathcal{F}_{AB}$  of the Brownian-particle model (black circles) related to pairs of configurational domains (labeled in the abscissa as defined in fig. 5.1). Error bars correspond to standard deviations. Reference data are calculated by numerical integration of the PMF (open red circles). Left, middle and right panels report calculations made by using the Bennett-like estimator (eq. 4.25) and the JE (eq. 4.23) in the  $A \rightarrow B$  and  $B \rightarrow A$  directions, respectively.

From general considerations on nonequilibrium work theory[88, 174], the Bennett-like estimator is expected to provide free energies more precise and accurate than those obtained from the JE. The better performances of the former approach appear quite evident from the error bars related to  $d$  and  $e$  pair domains.

More interesting is instead the behavior of the CDTS in terms of size and position of the configurational domains. It is worth noting that the choice of the transition kernels may affect the performances of the methodology, at least in this system. In fact, the switching protocol seems to yield more precise free energy estimates when highly populated, and hence more stable, regions of the initial domain are linked (via transition kernel) to more stable regions of the final domain, as it occurs in the cases  $a$ ,  $b$  and  $c$ . When this correspondence does not hold, as in the  $d$  and  $e$  cases, the precision decreases. This is ultimately due to the fact that, in the  $d$  and  $e$  cases, the better sampled paths give rise to a large work (and hence a small contribution to the path-ensemble averages appearing into eqs. 4.23 and 4.25), while the worst sampled paths yield a smaller work and hence a greater contribution to the path-ensemble averages. Therefore, the most favorable situation appears to be the one in which the better sampled paths produce the smallest work. With simple considerations on the arrangements of the  $\mathcal{D}_A$  and  $\mathcal{D}_B$  domains (fig. 5.1) and on the linear trend of the

transition move (eq. 5.22), we can envisage this feature in the cases  $a$ ,  $b$  and  $c$ . The error is correspondingly small. Furthermore, we note that differences in the size of the two domains do not affect significantly accuracy and precision of the estimates.

Although the CDTS is theoretically sound, the above considerations suggest that performance optimization could be achieved through a prior, even qualitative, knowledge of the equilibrium configurational domains. However, as we will see in the analysis of the dimer free energies, this reasoning cannot be generalized. On the other side, we have to consider that the mere computational efficiency (error minimization) may not be the only criterion employed to define the configurational domains. In fact, criteria based on efficiency may not fit physical criteria we are interested to. Therefore, other aspects related, for example, to geometrical arguments inherently not compatible with the computational efficiency, should be considered with higher priority. So, in general, calculations will be done disregarding the efficiency in terms of error optimization.

### Dimer in a Lennard-Jones fluid

The results obtained for the Brownian particle are basically confirmed by the calculations on the solvated dimer, a radically different system for which fast switching trajectories are produced. Also for this case study, different pairs of configurational domains are considered (fig. 5.2). In fig. 5.4, we compare accuracy and precision of  $\Delta F_{AB}$  estimates achieved by CDTS and SMD simulations carried out in the same operative conditions (see sec. 5.3.1 for details). In both cases, free energies are computed averaging 20 estimates obtained through the Bennett-like estimator (eq. 4.25) applied to independent sets of 100  $\mathcal{D}_A \rightarrow \mathcal{D}_B$  and 100  $\mathcal{D}_B \rightarrow \mathcal{D}_A$  nonequilibrium trajectories. Standard deviations are also reported in fig. 5.4 as error bars. An overview of fig. 5.4 allows to infer that CDTS performances are substantially comparable to those obtained with SMD, even if the error resulting from the latter method is slightly smaller. This can perhaps be ascribed to the different sampling of the initial microstates realized with the two methods. In fact, while CDTS trajectories start from phase-space microstates featured by different distances between the dimer particles, SMD limits the sampling to only one distance. This implies that in CDTS the sampling of the initial microstates has to account not only for the variance of the uncontrolled degrees of freedom (*i.e.*, the solvent), but also for the variability of the controlled degree of freedom, namely the distance between the dimer particles. This clearly enhances the phase space

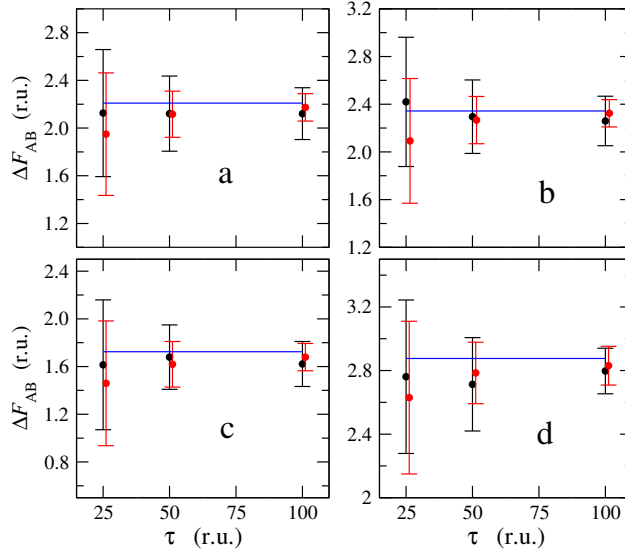


**Figure 5.4:** Free energy differences  $\Delta F_{AB}$  (in reduced units) computed by CDTS and SMD simulations (black and red circles, respectively) for the dimer system. Data are plotted against the duration  $\tau$  of the transition process (in reduced units). Error bars are the standard deviations. Reference free energies, calculated through numerical integration of the PMF obtained by thermodynamic integration, are also reported (blue lines). Each panel refers to a different pair of configurational domains, according to the definitions of fig. 5.2.

to be sampled, and hence the error with respect to the SMD. However, given the small differences in the errors, generalizing the above observation to all systems one may deal with is not safe. In front of these considerations, we outline that the possibility of sampling initial and final microstates into multidimensional domains (using more than one collective coordinate), if on one side makes the path sampling more difficult, on the other side gives direct access to free energy differences between such (multidimensional) domains. Obviously, this is not affordable by SMD, as it only allows to compute the PMF along a specific path in the multidimensional space of the collective coordinates, and hence to evaluate free energy differences between points rather than domains of such a space. The calculation

of free energy differences of configurational basins would be feasible through SMD only supplementing PMF calculations with local-sampling simulations, as proposed, for instance, in Ref.[82].

Furthermore, it is worth noting that the reference  $\Delta F_{AB}$  values are within the error bars obtained from both CDTS and SMD approaches. Increasing the duration  $\tau$  of nonequilibrium paths from 25 to 100 reduced time-units, error bars narrow from  $\sim 1.3$  to  $\sim 0.5$  reduced energy-units. Enhancement in precision is expected in both types of calculation, basically due to the decrease of dissipated work during the driven trajectories.

The  $a$ ,  $b$  and  $c$  cases of fig. 5.4 correspond to domains  $\mathcal{D}_A$  and  $\mathcal{D}_B$ , centered, in turn, around the minima corresponding to compact and extended dimer conformations (fig. 5.2). Consistently with the Brownian model, we do not observe significant variation in the error upon changing the domain size. However, we also note that moving the  $\mathcal{D}_B$  configurational domain aside the free energy minimum, as in the case  $d$ , no substantial worsening of the CDTS performances is observed. The error sources discussed for the Brownian model seem to play a negligible role in this case study.

### 5.3.3 Discussion and concluding remarks

The case studies considered above are basically aimed to validate numerically the CDTS and to illustrate, in a very simple way, how it works. The generality of the method is evident, and the following discussion highlights its suitability for investigating systems of physical and chemical interest. In general, the relevant quantity is the free energy difference between two thermodynamic states featured by different values of one or more order parameters, also called collective coordinates. Strictly speaking, a thermodynamic state is defined constraining the collective coordinate within an established domain  $\mathcal{D}_A$ , such that

$$\mathcal{D}_A = \{\mathbf{x} \in \mathcal{D} \mid \lambda_{A,i}^{(1)} \leq \xi_i(\mathbf{x}) \leq \lambda_{A,i}^{(2)}, \forall i = 1, \dots, m\}, \quad (5.27)$$

where  $\xi_i(\mathbf{x})$  is the  $i$ -th component of the  $m$ -dimensional vector  $\boldsymbol{\xi}(\mathbf{x})$  representing the collective coordinates and the parameters  $\lambda_{A,i}^{(1)}$  and  $\lambda_{A,i}^{(2)}$  identify the boundaries of  $\mathcal{D}_A$ . Analogous definition can be given for the second thermodynamic state, identified by the  $\mathcal{D}_B$  domain. It is worth noting, that, by using standard SMD in the framework of nonequilibrium work theorems, we can *only* determine PMFs along monodimensional paths designed into a mono or multidimensional space of the collective coordinates. This ultimately leads to free energy

differences between different portions of the established monodimensional path, rather than free energy differences between domains defined as in eq. 5.27. These latter can instead be assessed via CDTS, and only for  $m = 1$  both SMD and CDTS can be employed indifferently (as in our numerical tests). Configurational domains defined by eq. 5.27 may allow to set particularly simple CDTS-based switching protocols. As an example, we can imagine to deal with a bidimensional space of collective coordinates, namely  $\boldsymbol{\xi}(\mathbf{x}) = (\xi_1(\mathbf{x}), \xi_2(\mathbf{x}))$ , defined, *e.g.*, in terms of interatomic distances or torsional angles, or some combination of them. In such a case, the domains  $\mathcal{D}_A$  and  $\mathcal{D}_B$  can be represented in a plane as shown in fig. 5.5. A

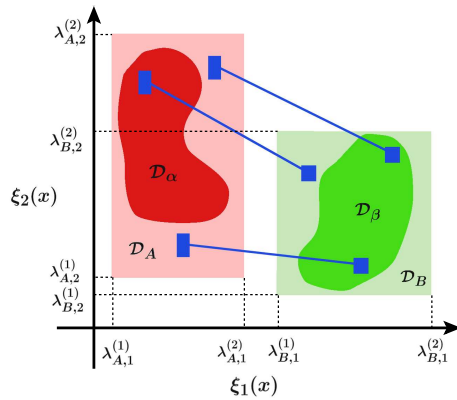


**Figure 5.5:** Schematic representation of generic target domains  $\mathcal{D}_\alpha$  and  $\mathcal{D}_\beta$  in the bidimensional space of collective coordinates,  $\boldsymbol{\xi}(\mathbf{x}) = (\xi_1(\mathbf{x}), \xi_2(\mathbf{x}))$ . The CDTS protocol connects domains of rectangular shape,  $\mathcal{D}_A$  and  $\mathcal{D}_B$ . The single nonequilibrium paths (blue lines) link infinitesimal volume elements (blue rectangles), whose ratio depends on the Jacobian determinant, while their shapes depend on the flux function associated with the transformation.

suitable CDTS protocol may link, in a bijective manner, points  $\mathbf{x}_0 \in \mathcal{D}_A$  to points  $\mathbf{x}_N \in \mathcal{D}_B$ , through the following time schedule:

$$\xi_i(\mathbf{x}(t)) = \frac{\lambda_i^{(2)}(t) - \lambda_i^{(1)}(t)}{\lambda_{A,i}^{(2)} - \lambda_{A,i}^{(1)}} \xi_i(\mathbf{x}_0) + \frac{\lambda_{A,i}^{(2)} \lambda_i^{(1)}(t) - \lambda_{A,i}^{(1)} \lambda_i^{(2)}(t)}{\lambda_{A,i}^{(2)} - \lambda_{A,i}^{(1)}}, \quad \text{with } i = 1, 2, \quad (5.28)$$

where  $\lambda_i^{(1)}(t) = \lambda_{A,i}^{(1)} + (\lambda_{B,i}^{(1)} - \lambda_{A,i}^{(1)}) t/\tau$  (and analogous definition for  $\lambda_i^{(2)}(t)$ ), with  $\tau$  being the time of the switching process. Equation 5.28 is a straightforward extension of eq. 5.22. Assuming that the dynamics of the uncontrolled degrees of freedom of the system is Hamiltonian, the Jacobian determinant associated with the whole trajectory equals the product  $\prod_{i=1}^2 (\lambda_{B,i}^{(2)} - \lambda_{B,i}^{(1)}) (\lambda_{A,i}^{(2)} - \lambda_{A,i}^{(1)})^{-1}$ . Its absolute value corresponds to the ratio between the infinitesimal volume elements of  $\mathcal{D}_A$  and  $\mathcal{D}_B$  in the collective-coordinate space (blue rectangles in fig. 5.5). The CDTS paths link these volumes in a bijective manner (blue lines in fig. 5.5). A drawback of eq. 5.27 is that it allows to define very regular domains, essentially of rectangular shape. Nevertheless, as remarked at the end of sec. 5.3.2, in several cases a more flexible definition of domain, based on energetical and/or geometrical criteria, may be required. These alternative criteria can give rise to domains featured by very complex hypersurfaces, extremely difficult to be described by simple analytic expressions (*e.g.*, the domains  $\mathcal{D}_\alpha$  and  $\mathcal{D}_\beta$  of fig. 5.5). In this respect, the impossibility of designing proper transition kernels can prevent a direct estimate of the free energy difference between the states identified by  $\mathcal{D}_\alpha$  and  $\mathcal{D}_\beta$ . Such a problem could however be tackled devising a thermodynamic cycle. Let consider two irregular domains,  $\mathcal{D}_\alpha$  and  $\mathcal{D}_\beta$ , identified by some criterion[82] and that we are interested into their free energy difference  $\Delta F_{\alpha\beta}$ . Moreover, let suppose we are able to compute, by using the CDTS, the free energy difference  $\Delta F_{AB}$  between rectangular domains  $\mathcal{D}_A$  and  $\mathcal{D}_B$ , such that  $\mathcal{D}_\alpha \subset \mathcal{D}_A$  and  $\mathcal{D}_\beta \subset \mathcal{D}_B$ , as displayed in fig. 5.5. In this situation, the free energy difference  $\Delta F_{\alpha A}$  between the states  $\alpha$  and  $A$  can be evaluated straightforwardly from the fraction of microstates picked into  $\mathcal{D}_\alpha$  during an equilibrium sampling realized into  $\mathcal{D}_A$ . An analogous calculation would give  $\Delta F_{\beta B}$ . The sum  $\Delta F_{\alpha\beta} = \Delta F_{\alpha A} - \Delta F_{\beta B} + \Delta F_{AB}$  provides the desired free energy difference. The previous arguments outline that a more accurate definition of the target chemical states  $\mathcal{D}_\alpha$  and  $\mathcal{D}_\beta$  can be adopted without changing the number of simulations to be performed (in addition to the equilibrium simulations producing the initial microstates and the nonequilibrium simulations switching the system from  $\mathcal{D}_A$  to  $\mathcal{D}_B$ , and/or viceversa). A case representative of the ideas discussed here is the calculation of the adsorption free energy in a generic equilibrium process  $\text{AdsSur} \rightleftharpoons \text{Ads} + \text{Sur}$ , where Ads is the adsorbate and Sur is the surface of the adsorbent. The bounded configuration AdsSur can be sampled using equilibrium molecular dynamics or Monte Carlo simulations, that allow to detect an initial domain  $\mathcal{D}_\alpha$ , corresponding to the layer where the adsorbate is distributed. If the adsorbate can diffuse over the surface, rectangular bound-

aries can optionally be applied along the surface by introducing wall-potentials. Along the direction perpendicular to the surface no limitations are instead enforced to the motion of the adsorbate. In this sense, no prior definition of the binding domain is necessary. The CDTS-based protocol, performing the desorption process in nonequilibrium conditions, implies a deterministic evolution of the center of mass of the adsorbate along the axis, say  $z$ , perpendicular to the surface. In the simplest case, the  $z$  coordinate of the center of mass can be externally driven according to the time schedule  $z(t) = z(0) + vt$ , where  $z(0)$  is the initial value of the coordinate and  $v$  is the switching rate. The final time of the switching simulations should be set so that adsorbate and adsorbent are no more interacting. Actually, this approach has already been applied without theoretical justification to study the impact of interfacial high-density water layer on the estimation of adsorption free energies by means of the JE[209]. Furthermore, the described procedure may result suitable to investigate other important class of processes such as receptor-ligand equilibria, following the ideas disclosed in studies of protein-ligand binding free energies[144].



---

## Annealed importance sampling with constant cooling rate

---

### 6.1 Introduction

Generalization of NWTs, operated in the previous chapter 5, is now applied in the Annealed Importance Sampling (AIS) framework. Annealed Importance Sampling assigns equilibrium weights to nonequilibrium samples generated by a simulated annealing protocol[103, 127, 140]. The weights are obtained in a series of annealing simulations starting from configurational states sampled at high temperature and then used to calculate equilibrium averages at a target temperature, usually 298 K. Calculations performed on a dileucine peptide in implicit solvent by Lyman and Zuckerman[127] showed that an efficiency gain of about three can be obtained by using AIS in lieu of conventional constant-temperature simulations. It is however evident that the efficiency of the method may vary in dependence of the complexity of the system under investigation. AIS closely resembles, and perhaps it was inspired by, simulated annealing methodologies[105, 194]. In conventional simulated annealing schemes, a configuration of the system, typically a protein, is cooled from high to low temperature in steps where constant-temperature dynamics is alternated to instantaneous lowering of the

temperature. Usually, the system is cooled down to a very low temperature, since the aim of the simulated annealing is to find the global minimum on the energy landscape. However, we can imagine ending the cooling process at  $T_0 = 298$  K and producing many of such trajectories, sampling the initial configurations at equilibrium from a simulation at high temperature, say  $T_M$ . This temperature has to be chosen sufficiently high to overcome the energy barriers between the configurational basins of interest, eventually leading to equilibrium more easily. We then have an ensemble of annealed configurations, though clearly not distributed canonically at  $T_0$ . AIS is a way to reweight this distribution allowing to compute equilibrium averages at  $T_0$ , or to any other intermediate temperature between  $T_M$  and  $T_0$ . The present chapter deals with two main issues. From one side, we are interested to clarify the theoretical aspects that correlate AIS schemes to nonequilibrium work relations[50, 63–65, 73, 74, 109, 110, 161, 204], and especially to generalized versions of such work relations where mechanical and/or thermal changes may be involved[26, 33, 34, 202]. This leads us to write down a general expression for path/configuration reweighting which goes beyond the simple temperature-stepwise approach[127], calling for truly arbitrary schedules. Such an aspect is related to the second target of this work. In particular, we will show that annealing schedules realized at constant cooling rate, *i.e.* by using a protocol where temperature is lowered at each simulation step by a small fixed amount, are much less dissipative, resulting in a greater efficiency with respect to conventional schedules in which relaxation periods (constant-temperature dynamics) are enforced after each thermal jump. We start by illustrating the AIS approach, focusing on the protocol and the basic equation that allow to recover the equilibrium average of a generic physical quantity from a series of simulated annealed trajectories (sec. 6.2.1). Then, we outline the correlation existing between AIS and the generalized nonequilibrium path-ensemble average methods (sec. 6.2.2) following the guidelines indicated in the previous chapter 5. Illustrative calculations on a model system are then reported (sec. 6.4) to show the different performances of constant-rate and stepwise schedules employed for annealing. Concluding remarks are given in sec. 6.5.

## 6.2 Theory

### 6.2.1 Annealed importance sampling

Before describing AIS, we introduce the simulation context by especially focusing on the partition function of the system when a barostat and a thermostat are employed to enforce constant-pressure, constant-temperature conditions.

Let consider a system with Hamiltonian  $H(\mathbf{x}, V)$  dependent on the vector  $\mathbf{x}$ , collecting coordinates and momenta of the particles and on the volume  $V$ . Suppose that the system evolves in the NPT ensemble (number of particles, pressure and temperature kept constant) through the coupling with a heat bath and a barostat and that such a coupling is regulated by equations of motion rather than interaction energy terms. This is indeed the case of popular algorithms for non-Hamiltonian molecular dynamics[69, 193]. The time evolution of this extended system, *i.e.*, physical system plus heat bath plus barostat, takes place in the phase space  $\mathbf{z} = \{\mathbf{x}, V, \mathbf{s}, \mathbf{h}\}$ , that includes, in addition to the physical variables,  $\mathbf{x}$  and  $V$ , the  $\mathbf{s}$  and  $\mathbf{h}$  variables associated with the heat bath and the barostat, respectively, whose distributions can be generically denoted as  $f_T(\mathbf{s})$  and  $g_T(\mathbf{h})$ . The equilibrium distribution in the extended phase space at fixed temperature  $T$  can be written as product of the distributions of the defined dynamic variables[26, 69, 193],

$$p_T(\mathbf{z}) = \frac{e^{-\beta H(\mathbf{x}, V)} f_T(\mathbf{s}) g_T(\mathbf{h})}{Q'_T} = \frac{e^{-\beta H'_T(\mathbf{z})}}{Q'_T}, \quad (6.1)$$

where  $\beta = (k_B T)^{-1}$  and  $Q'_T = \int \exp(-\beta H'_T(\mathbf{z})) d\mathbf{z}$  is the partition function of the extended system, or simply the extended partition function. By analogy with canonical Hamiltonian systems, we term  $H'_T(\mathbf{z})$  as extended Hamiltonian. If the functions  $\psi_T(\mathbf{s}) = -\beta^{-1} \ln f_T(\mathbf{s})$  and  $\phi_T(\mathbf{h}) = -\beta^{-1} \ln g_T(\mathbf{h})$  are defined, then it is possible to construct the extended Hamiltonian as the sum  $H'_T(\mathbf{z}) = H(\mathbf{x}, V) + \psi_T(\mathbf{s}) + \phi_T(\mathbf{h})$ . Since system-bath, system-barostat and bath-barostat interaction energies do not appear in the extended Hamiltonian, the extended partition function can be factorized as

$$Q'_T = Z_T \int e^{-\beta \psi_T(\mathbf{s})} d\mathbf{s} \int e^{-\beta \phi_T(\mathbf{h})} d\mathbf{h}, \quad (6.2)$$

$Z_T$  being the partition function of the physical system, that can be recovered by estimating the quantity  $Q'_T$  if the two integrals on  $\mathbf{s}$  and  $\mathbf{h}$  are analytically computable. The specific

expressions of the thermostat and barostat contributions to the extended Hamiltonian clearly depend on the implemented equations of motion. In our test calculations we have used one of the most effective methods able to produce the correct NPT-partition function for systems, with and without momentum conservation[135].

Let consider now many independent annealed trajectories realized by means of NPT equations of motion, which at time  $t_n$  have just been cooled from temperature  $T_{n+1}$  to  $T_n$ . Immediately after  $t_n$ , before the system is allowed to relax to the equilibrium distribution, we can compute the equilibrium average of an arbitrary quantity  $A$  at  $T_n$  as follows

$$\begin{aligned} \langle A \rangle_n &= \frac{1}{Q'_n} \int A(\mathbf{z}) \exp(-\beta_n H'_n(\mathbf{z})) \, d\mathbf{z} \\ &= \frac{Q'_{n+1}}{Q'_n} \frac{\int A(\mathbf{z}) \omega(\mathbf{z}) \exp(-\beta_{n+1} H'_{n+1}(\mathbf{z})) \, d\mathbf{z}}{Q'_{n+1}} \\ &= \frac{Q'_{n+1}}{Q'_n} \langle A \omega \rangle_{n+1}, \end{aligned} \quad (6.3)$$

where

$$\omega(\mathbf{z}) = \frac{\exp(-\beta_n H'_n(\mathbf{z}))}{\exp(-\beta_{n+1} H'_{n+1}(\mathbf{z}))} \quad (6.4)$$

is a weight factor for configuration  $\mathbf{z}$ , which allows to reweight the distribution at  $T = T_{n+1}$  to calculate averages over the distribution at  $T = T_n$ . Generalizing the argument to  $M$  temperature steps is straightforward[140], by forming the product of weights for successive annealing steps:

$$w[\Gamma] = \prod_{n=0}^{M-1} \omega(\mathbf{z}_n) = \prod_{n=0}^{M-1} \frac{\exp(-\beta_n H'_n(\mathbf{z}_n))}{\exp(-\beta_{n+1} H'_{n+1}(\mathbf{z}_n))}. \quad (6.5)$$

The quantity  $w[\Gamma]$  is the weight of the final configuration, which is a functional of the trajectory (denoted as  $\Gamma$ ) to reach such a configuration. Note that in the previous equation  $\beta_0$  corresponds to the final (target) inverse temperature and the subscript  $t_n$  indicates the time at which the  $T_n \rightarrow T_{n-1}$  cooling step occurs. Therefore, the quantities  $H'_n(\mathbf{z}_n)$  and  $H'_{n-1}(\mathbf{z}_n)$  are evaluated at the same time  $t_n$ , *i.e.* for the microstate[2]  $\mathbf{z}_n$  of the trajectory  $\Gamma$ , but using a different parametric value of the temperature. If  $H'_T(\mathbf{z})$  does not depend parametrically on  $T$  (see, *e.g.*, discussion in sec. IV.B of Ref.[26]), then  $w[\Gamma]$  can be written as

$$w[\Gamma] = \prod_{n=0}^{M-1} \exp[-(\beta_n - \beta_{n+1}) H'(\mathbf{z}_n)]. \quad (6.6)$$

Equation 6.5, or alternatively eq. 6.6, provides the weight for a trajectory cooled through inverse temperatures  $\beta_M, \beta_{M-1}, \dots, \beta_0$ . At each temperature, reweighting ensures that averages may be calculated for the appropriate canonical distribution, though the system has not yet relaxed.

The AIS is easily turned into an algorithm for producing a canonical distribution from serially generated annealed trajectories.

- 1) Generate a sample of the distribution at  $T = T_M$  by a sufficiently long (equilibrium) simulation.
- 2) Select a configuration of the system at random and anneal it down to  $T = T_0$ . Keep track of the weight for this trajectory by using eq. 6.5 or 6.6 and of the physical quantity  $A$  of interest.
- 3) Repeat step 2 until  $N$  trajectories are produced. To the final microstate of a generic trajectory  $j$  it is possible to associate a value  $A_j$  of the physical quantity of interest and a weight  $w_j$ .

Equilibrium averages at  $T = T_0$  are then calculated by the weighted average

$$\langle A \rangle_{T_0} = \frac{\sum_{i=1}^N w_i A_i}{\sum_{j=1}^N w_j}. \quad (6.7)$$

### 6.2.2 Annealed importance sampling from generalized nonequilibrium path-ensemble theory

To derive AIS from nonequilibrium path-ensemble theory, exposed in the previous chapter 4 and inspired by Crooks treatment[50], we will show a generalization procedure of standard NWTs that can be considered a particular case of the CDTS scheme described in previous chapter 5. We start considering the realization of a process consisting of  $M$  steps, during which the temperature is varied in a finite amount of time from the initial value  $T_M$  to the final value  $T_0$  with arbitrary time schedule. We indicate the extended phase-space trajectory during this realization as  $\Gamma$ . Such a trajectory can be associated with a conjugate (reverse) trajectory, denoted as  $\Gamma^*$ , generated by a time reverse schedule of the temperature. The existence of conjugate trajectories is guaranteed by the reversibility of the equations of motion. The transient fluctuation theorem (eq. 4.18) establishes a relation between the probability of observing the trajectory  $\Gamma$  during a realization of the considered process and

the probability of observing the trajectory  $\Gamma^*$  during a time reverse realization of the same process:

$$\frac{P_{T_M \rightarrow T_0}[\Gamma]}{P_{T_0 \rightarrow T_M}[\Gamma^*]} = \frac{Q'_0}{Q'_M} e^{\mathcal{W}[\Gamma]}, \quad (6.8)$$

where  $P_{T_M \rightarrow T_0}[\Gamma]$  and  $P_{T_0 \rightarrow T_M}[\Gamma^*]$  correspond to the probabilities of performing the trajectories  $\Gamma$  and  $\Gamma^*$  provided that the initial microstates are taken from the distributions  $p_M(\mathbf{z})$  and  $p_0(\mathbf{z})$ , respectively. The quantity  $\mathcal{W}[\Gamma]$  in eq. 6.8 is the generalized dimensionless work performed on the system during the trajectory  $\Gamma$ . We note how eq. 6.8 represents a special case of the generalized CFT, corresponding to eq. 5.12. Assuming that no constrained transition between subdomains of the phase space  $\mathcal{D}$  takes place, the transition kernel  $T(\mathbf{z}_{n+1} \rightarrow \mathbf{z}_n)$  (defined in sec. 5.2.1) reduces to an identity function, *i.e.*,  $T(\mathbf{z}_{n+1} \rightarrow \mathbf{z}_n) = \delta(\mathbf{z}_n - \mathbf{z}_{n+1})$ . Under this condition, at the  $n$ -th step taking place at time  $t_n$ , non-normalized equilibrium distribution is  $\rho_n(\mathbf{z}) = e^{-\mathcal{H}'_n(\mathbf{z})} = e^{-\beta_n H'_n(\mathbf{z})}$  and the transition distribution (eq. 5.5) becomes  $\tau_n(\mathbf{z}) = \rho_{n+1}(\mathbf{z}) = e^{-\beta_{n+1} H'_{n+1}(\mathbf{z})}$ . Substitution into generalized work expression, eq. 5.13, gives

$$\mathcal{W}[\Gamma] = \ln \left( \prod_{n=0}^{M-1} \frac{\rho_{n+1}(\mathbf{z}_n)}{\rho_n(\mathbf{z}_n)} \right) = \sum_{n=0}^{M-1} [\beta_n H'_n(\mathbf{z}_n) - \beta_{n+1} H'_{n+1}(\mathbf{z}_n)]. \quad (6.9)$$

Expressing generalized work in the continuous limit  $dt = t_n - t_{n+1} = \frac{\tau}{M} \rightarrow 0$ , we gain

$$\mathcal{W}[\Gamma] = \int_0^\tau \frac{\partial}{\partial t} [\beta(t) H'(\mathbf{z}; \lambda(t))] dt, \quad (6.10)$$

where the integral is extended over the whole duration  $\tau$  of the trajectory. In the expression of  $\mathcal{W}[\Gamma]$ , the explicit dependence on time can lie, not only in the inverse temperature of the external bath  $\beta(t)$ , but also in the extended Hamiltonian through some mechanical control parameter  $\lambda(t)$ , introduced to simultaneously change appropriate collective coordinates (interatomic distances, torsion angles, volume, coordination numbers, etc.), or through the thermostat and/or barostat inertial factors[26]. In the following, in order to simplify the discussion and to remain adherent to the standard application of AIS, we will focus on the description of thermal annealing processes, keeping the explicit dependence on temperature and time only in  $\beta(t)$ . Therefore, the extended Hamiltonian can be shortly written as  $H'[\Gamma]$ .

We introduce now a functional of the trajectory as  $\mathcal{A}[\Gamma] = \mathcal{A}^*[\Gamma^*]$ , and the generalized dimensionless dissipative work  $\mathcal{W}_d[\Gamma] = \mathcal{W}[\Gamma] + \ln \frac{Q'_0}{Q'_M}$ . Following Crooks, eq. 4.22, averages

of  $\mathcal{A}^*$  and  $\mathcal{A} \exp(-\mathcal{W}_d)$  over the ensembles of reverse and forward trajectories can be related by the following equation:

$$\langle \mathcal{A}^* \rangle_{T_0 \rightarrow T_M} = \langle \mathcal{A} e^{-\mathcal{W}_d} \rangle_{T_M \rightarrow T_0}. \quad (6.11)$$

It is also possible to derive another kind of relation by setting  $\mathcal{A}$  to be a function of the microstate of the system at some time. In particular, choosing  $\mathcal{A}$  to be a function of the final microstate  $\Gamma_{\tau, T_M \rightarrow T_0}$  of the forward process, *i.e.*  $\mathcal{A}[\Gamma] = A(\mathbf{z}_{\tau, T_M \rightarrow T_0})$ , we have to average a function of the initial microstate in the reverse process, *i.e.*  $\mathcal{A}^*[\Gamma^*] = A(\mathbf{z}_{0, T_0 \rightarrow T_M})$ . Therefore, in the reverse process the average is over the initial equilibrium ensemble of the system, and the subsequent dynamics is irrelevant:

$$\langle A(\mathbf{z}_{0, T_0 \rightarrow T_M}) \rangle_{T_0 \rightarrow T_M} \equiv \langle A \rangle_{T_0} = \langle A(\mathbf{z}_{\tau, T_M \rightarrow T_0}) e^{-\mathcal{W}_d[\Gamma]} \rangle_{T_M}, \quad (6.12)$$

where we have replaced the subscripts  $T_0 \rightarrow T_M$  and  $T_M \rightarrow T_0$  with  $T_0$  and  $T_M$ , respectively, to emphasize the thermodynamic conditions of the equilibrium ensemble average (left-hand side) and the thermodynamic conditions of the initial microstates in path-ensemble average (right-hand side). It is interesting to note that eq. 6.12 allows to compute an ensemble average at a given temperature without really performing simulations at that temperature. The path-ensemble average on the right-hand side of eq. 6.12 can be computed picking microstates from an equilibrium simulation at the arbitrary temperature  $T_M$  and then enforcing a thermal annealing with arbitrary time schedule, until the target temperature  $T_0$  is reached. In this annealing, there is no need of using a series of constant-temperature simulations, as usually done in AIS and simulated annealing implementations. A constant-rate annealing is suitable as well and, as we will see, may turn out more effective because it can decrease significantly dissipation[33]. By setting  $A(\mathbf{z}_{\tau, T_0 \rightarrow T_M}) = A(\mathbf{z}_{\tau, T_M \rightarrow T_0}) = c$  into eq. 6.12,  $c$  being an arbitrary constant, we obtain the Jarzynski equality[109]

$$\frac{Q'_0}{Q'_M} = \langle e^{-\mathcal{W}[\Gamma]} \rangle_{T_M}. \quad (6.13)$$

Substituting eq. 6.13 into eq. 6.12, we obtain the following relation

$$\langle A \rangle_{T_0} = \frac{\langle A(\mathbf{z}_{\tau, T_M \rightarrow T_0}) e^{-\mathcal{W}[\Gamma]} \rangle_{T_M}}{\langle e^{-\mathcal{W}[\Gamma]} \rangle_{T_M}}. \quad (6.14)$$

The above equation is exact in the limit of infinite number of trajectories. According to eq. 6.14, the estimator of  $\langle A \rangle_{T_0}$  resulting from a finite path sampling is

$$\langle A \rangle_{T_0} = \frac{\sum_{i=1}^N A_i e^{-\mathcal{W}[\Gamma_i]}}{\sum_{j=1}^N e^{-\mathcal{W}[\Gamma_j]}}, \quad (6.15)$$

where the quantity  $A$  at the end of the  $i$ th trajectory is compactly written as  $A_i$  and  $N$  is the number of trajectories. The correspondence between the above equation and the AIS relation (eq. 6.7) is revealed writing down the explicit expression of the dimensionless work  $\mathcal{W}[\Gamma]$  for a standard thermal annealing process. In AIS, the time-evolution of  $\beta(t)$  is stepwise and can be generically written as

$$\beta(t) = \beta_M + \sum_{n=0}^{M-1} (\beta_n - \beta_{n+1}) \theta(t - t_n), \quad (6.16)$$

where  $\theta(x)$  is the Heaviside step function[3]. The generalized work  $\mathcal{W}[\Gamma]$  under the AIS scheme can be recovered by substituting eq. 6.16 into eq. 6.10, obtaining

$$\mathcal{W}[\Gamma] = \sum_{n=0}^{M-1} (\beta_n - \beta_{n+1}) H'(\mathbf{z}_n). \quad (6.17)$$

It is now straightforward to recognize the weight  $w[\Gamma]$  of eq. 6.6 as the exponential of the generalized work  $\mathcal{W}[\Gamma]$ , *i.e.*  $w[\Gamma] = e^{-\mathcal{W}[\Gamma]}$ , which allows to identify the AIS average of eq. 6.7 with the nonequilibrium path-ensemble average of eq. 6.15.

### 6.3 Model system and simulations

Molecular dynamics simulation tests are aimed at evaluating the differences between AIS protocols realized in constant-rate and stepwise manners. Simulations have been performed on a Lennard-Jones fluid consisting of 500 particles of equal mass. Two of these particles, defined as a dimer, interact through a double-well potential along the  $x$  direction of the laboratory frame and harmonic forces are applied to restraint their motion about the  $x$  axis:

$$U = c [(x_{12} - a)^2 - d] (x_{12} - b)^2 + k(y_1^2 + z_1^2 + y_2^2 + z_2^2), \quad (6.18)$$



where  $x_1, y_1, z_1, x_2, y_2$  and  $z_2$  represent the Cartesian coordinates of the dimer particles and  $x_{12} = x_2 - x_1$ . Two series of simulation tests have been performed, differing from one another in the  $c$  parameter, being, in turn, 202.5 and 1012.5. The other parameters are  $d = 3.333 \times 10^{-3}$ ,  $a = 1$ ,  $b = 1.667$  and  $k = 4500$ . All quantities reported above and in the following are in reduced units, unless otherwise specified. The potential energy  $U$  is displayed as a function of  $x_{12}$  in fig. 6.1. Enforcing  $c = 1012.5$ , a double-well potential is

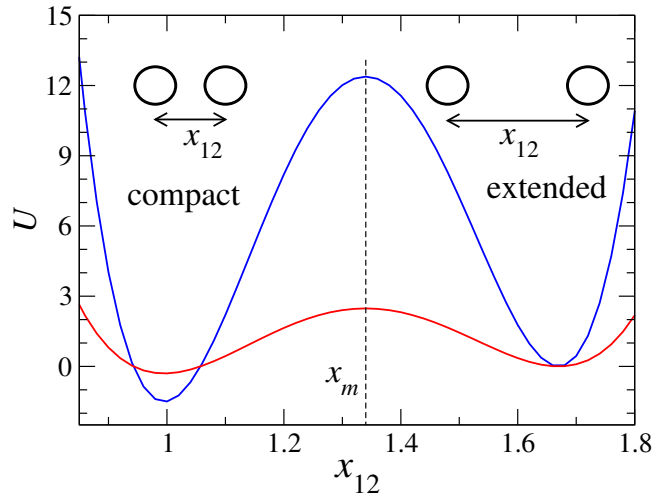


**Figure 6.1:** Double-well potential  $U$  (eq. 6.18) as a function of the dimer distance  $x_{12}$  ( $U$  and  $x_{12}$  are in reduced units), corresponding to  $c = 1012.5$  (blue line) and  $c = 202.5$  (red line). Dimer distances smaller than  $x_m$ , denoted with the dashed line, define compact configurations, while greater distances define extended configurations (eq. 6.23).

generated where the energy barrier is about 23 times larger than the thermal energy, which holds  $\sim 0.6$  at our thermodynamic conditions,  $T_0 = 0.6$  and  $P_0 = 1.94 \times 10^{-4}$ . In this case, the system gets trapped in a metastable state, since the thermal energy is much smaller than the energy barrier. This is confirmed from an equilibrium molecular dynamics simulation performed at constant temperature  $T_0$  and constant pressure  $P_0$ . As a matter of fact, such a situation is particularly suited for simulated annealing and hence for AIS, being the system

featured by deep free energy minima. By setting  $c = 202.5$ , the energy barrier is only  $\sim 4.5$  greater than the thermal energy. In such a case, a conventional equilibrium simulation is sufficient to sample the whole free energy surface. However, we decided to report also on this latter simulation test to outline the versatility of the method, though the discussion will be focused on the system with higher energy barrier. An additional Lennard-Jones potential acts between the dimer particles, which also describes, with identical  $\sigma$  and  $\epsilon$  parameters, solvent-solvent and dimer-solvent interactions. The annealing simulations have been carried out using a cubic box with standard periodic boundary conditions and are supplied with a barostat and a thermostat as prescribed by the equations of motion of Martyna, Tobias and Klein[135]. The temperature is kept constant by means of a Nosé-Hoover chain thermostat[192] with four coupled thermostating devices. The system evolution is made in time steps of  $1.364 \times 10^{-3}$ . Particle-pair contributions of Lennard-Jones energy and forces are smoothly damped to zero in the distance range 3 to 3.27. One constant-rate and three stepwise AIS schedules have been applied to a set of 1200 annealing simulations. The initial microstates are picked at regular time intervals of 2.73 from an equilibrium  $NPT$  simulation performed at temperature  $T_M = 2.48$  and pressure  $P_M = 1.55$ . The four independent sets of annealing simulations are realized by taking the same initial microstates, thus producing results independent from the method of sampling such microstates. Each annealing simulation has a time duration  $\tau$  of 136.41. For all AIS schedules, temperature and pressure have been decreased from  $T_M$  and  $P_M$  to the final values  $T_0 = 0.6$  and  $P_0 = 1.94 \times 10^{-4}$ . The three stepwise AIS schedules have been applied enforcing  $M$  annealing steps at fixed time intervals ( $M = 11, 21$  and  $61$ ; from now on denoted as S11, S21 and S61, respectively), at which temperature and pressure are instantaneously varied by  $\Delta T = (T_0 - T_M)/M$  and  $\Delta P = (P_0 - P_M)/M$ :

$$T(t) = T_M + \Delta T \sum_{j=0}^{M-1} \theta\left(t - j \frac{\tau}{M}\right) \quad (6.19)$$

$$P(t) = P_M + \Delta P \sum_{j=0}^{M-1} \theta\left(t - j \frac{\tau}{M}\right), \quad (6.20)$$

where  $\theta(x)$  is the Heaviside step function[3]. The constant-rate AIS scheme, from now on denoted as CR, has been implemented using the following time schedules for temperature

and pressure:

$$\begin{aligned} T(t) &= T_M + (T_0 - T_M) t/\tau \\ P(t) &= P_M + (P_0 - P_M) t/\tau. \end{aligned} \tag{6.21}$$

We point out that the above time schedules for temperature and pressure may not be optimal. Perhaps, less dissipative and hence more effective transformations could be obtained through a non-linear time evolution of  $T$  and  $P$ . This is however irrelevant for our conclusions, because the aim of the comparative analysis is to evaluate the relative performances of stepwise and constant-rate schedules, rather than their absolute efficiency.

## 6.4 Simulation tests

The aim of the present simulation tests is to provide a comparative evaluation of the performances of constant-rate and stepwise AIS schedules in estimating the probability ratio of the extended and compact configurations of the dimer at the target conditions of temperature and pressure, *i.e.*,  $T_0$  and  $P_0$  (see sec. 6.3). We will report this probability ratio as free energy difference between the extended and compact states:

$$\Delta G = G_{\text{ext}} - G_{\text{com}} = -k_B T_0 \ln \frac{\bar{\chi}_{\text{ext}}}{\bar{\chi}_{\text{com}}}, \tag{6.22}$$

where  $\bar{\chi}_{\text{ext}}$  and  $\bar{\chi}_{\text{com}}$  are the mean populations of extended and compact configurations, respectively. In conventional equilibrium simulations, populations of configurational states are computed straightforwardly by counting the number of times the system is found in each configuration, provided that sampling is ergodic. In the AIS framework, the quantities  $\bar{\chi}_{\text{ext}}$  and  $\bar{\chi}_{\text{com}}$  are computed via eq. 6.15, exploiting, in turn, the population functions  $\chi_{\text{ext}}$  and  $\chi_{\text{com}}$  in place of  $A_i$ :

$$\begin{aligned} \chi_{\text{com}} &= \begin{cases} 1 & \text{if } x_{12} < x_m \\ 0 & \text{if } x_{12} \geq x_m \end{cases} \\ \chi_{\text{ext}} &= 1 - \chi_{\text{com}}, \end{aligned} \tag{6.23}$$

where  $x_m = 1.34$  corresponds to the dimer distance at which the energy barrier lies (see fig. 6.1). We remark that the double-well dimer potential with  $c = 1012.5$  (from now on,

the related system will be denoted as high energy-barrier system) has been designed to introduce an energy barrier large enough to produce a very slow recrossing rate between extended and compact configurations. In fact, no crossing event has been observed during a long equilibrium molecular dynamics simulation. Therefore, the energetics into play makes our high energy-barrier system suitable for testing non-conventional methods, such as AIS, in enhancing configurational sampling. In fig. 6.2, we report estimates of  $\Delta G$  obtained for

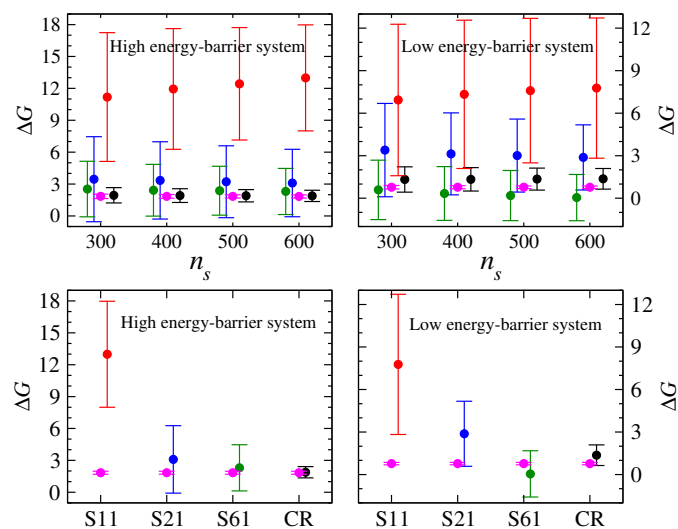


**Figure 6.2:** *Upper panels:* estimates of the free energy difference between extended and compact configurations,  $\Delta G = G_{\text{ext}} - G_{\text{com}}$  (reduced units), computed for low and high energy-barrier systems ( $c = 202.5$  and  $1012.5$ , respectively) with S11 (red), S21 (blue), S61 (green) and CR (black) schedules. Calculations have been made by using the bootstrap method, exploiting a variable number of trajectories ( $n_s = 300, 400, 500, 600$ ) for each bootstrapped  $\Delta G$  estimate (see text for details). Standard deviations are reported as error bars. For the sake of clarity, the data are shifted along the abscissa. *Lower panels:*  $\Delta G$  estimates computed by using  $n_s = 600$  (data taken from the upper panels). Reference data (magenta) are from Umbrella Sampling simulations.

both low and high energy-barrier systems supplied with S11, S21, S61 and CR schedules. For

each AIS schedule,  $\Delta G$ s and the related standard deviations have been computed through the bootstrap method[59], by exploiting  $10^4$  bootstrapped  $\Delta G$  estimates calculated with a variable number of trajectory samples,  $n_s = 300, 400, 500$  and  $600$ , randomly picked from the whole set of 1200 annealed trajectories. The data related to  $n_s = 600$  are reported separately in fig. 6.2 (lower panels) to highlight the dependence of  $\Delta G$  on the number of annealing steps. We point out that the uncertainties arising from bootstrapping do not account for bias contribution. Determining uncertainty of exponential averages (statistical plus bias) is a rather difficult task[210]. In this respect, a comparative analysis of the four AIS schemes can roughly be gained determining the deviations of the  $\Delta G$  estimates from a bias-free reference value. This reference free energy difference has been obtained through a constant-temperature constant-pressure Umbrella Sampling[188] simulation at the target thermodynamic conditions, *i.e.*  $T_0$  and  $P_0$ . The simulation-time length is 13641. The potential energy surface of the dimer particles has been made flatter through an additional potential  $V_{\text{us}}$ :

$$V_{\text{us}} = \begin{cases} -U & \text{for } x_{12} < 2 \\ -U + 1012.5 (x_{12} - 1)^2 (x_{12} - 2)^2 & \text{for } x_{12} \geq 2 \end{cases} \quad (6.24)$$

where  $U$  is the double-well potential of eq. 6.18. In order to compute the reference free energy data for the low and high energy-barrier systems, different  $U$  potentials (by setting  $c = 202.5$  and  $1012.5$  into eq. 6.18, respectively) have been employed in eq. 6.24. The standard reweighting formula[188] has been used to evaluate the population functions  $\chi_{\text{ext}}$  and  $\chi_{\text{com}}$  of eq. 6.23. Further simulation details are given in sec. 6.3. From fig. 6.2, it is evident that both precision and accuracy globally improve with increasing the number of annealing steps of the AIS schedules. In fact, regardless the value of  $n_s$ , while the CR schedule provides almost exact  $\Delta G$  estimates with small error bars, S11 and S21 schedules deviate from the reference values by more than 200% and 50%, respectively, with error bars one order of magnitude greater than those obtained from the CR schedule. Stepwise schedules clearly approximate the CR one as the number of annealing steps increases, as we can infer observing the data obtained by using the S61 schedule. From the viewpoint of nonequilibrium work theory, these results can be rationalized considering the biasing phenomenon in work exponential averages and the increase of such systematic error with the mean dissipation associated to the process. More precisely, it has been shown that, in the

limit of a large number of sampled work values, the bias is roughly proportional to the variance of the exponential of minus the dissipated work[88]  $\text{Var}[\exp(\Delta\mathcal{G} - \mathcal{W})]$ , where  $\Delta\mathcal{G}$  is the dimensionless free energy difference between the final and initial states of the process. In our case, the dimensionless work  $\mathcal{W}$  is computed via eq. 6.17, while  $\Delta\mathcal{G} = \mathcal{G}(T_0) - \mathcal{G}(T_M)$ , with  $\mathcal{G}(T_M) = -\ln Q'(T_M)$  and  $\mathcal{G}(T_0) = -\ln Q'(T_0)$ [4] being the dimensionless free energies of the high and low temperature states, respectively. These considerations lead us to analyze the dimensionless dissipated-work distributions related to stepwise and constant-rate schedules. We notice that, in a comparative analysis of the dissipated works, as  $\Delta\mathcal{G}$  does not depend on the kind of AIS schedule, we may focus on the work differences (in fact, work differences correspond to dissipated-work differences). However, since it can be of some interest to evaluate the absolute degree of reversibility of the nonequilibrium processes, which is correlated to the absolute dissipation  $\mathcal{W} - \Delta\mathcal{G}$ , we attempt to get a  $\Delta\mathcal{G}$  estimate as much accurate as possible. A good estimate of  $\Delta\mathcal{G}$  can be gained exploiting bidirectional nonequilibrium techniques[35, 37, 50, 137, 174, 177] extended to thermal processes[26, 34, 202]. In particular, we have used the Bennett-like approach[18, 174] applied to the CR schedule (see eq.27 of Ref.[26]), because such a schedule has been found to produce the lowest mean work (this feature should enhance the accuracy and precision of the bidirectional nonequilibrium technique[159]). To this aim, a number of 1200 simulation trajectories has been realized with a reversed schedule for temperature and pressure, which corresponds to eq. 6.21 with exchanged initial and final conditions. Initial system configurations have been picked at regular time intervals from a Nonequilibrium Candidate Monte Carlo (NCMC) simulation[147] at temperature  $T_0$  and pressure  $P_0$ . NCMC is a simulation method devised to design Monte Carlo moves with high acceptance probabilities, through nonequilibrium driven trajectories in the configurational space. Here, we have employed the configurational-freezing variant of NCMC[86]. In this variant, the probability of accepting a candidate configuration as the next sample in the Markov chain is enhanced through the Configurational Freezing algorithm[27, 143], according to which only the evolution of the particles close to the dissipation region is allowed during a nonequilibrium attempted move. The distribution functions of the dimensionless dissipated work,  $\mathcal{W} - \Delta\mathcal{G}$ [4], obtained for the high energy-barrier system using the S11, S21 and CR schedules are reported in fig. 6.3. Expanded views are shown in the figure to highlight the shapes of the distributions and especially their widths. It can be seen that, while the CR schedule produces trajecto-

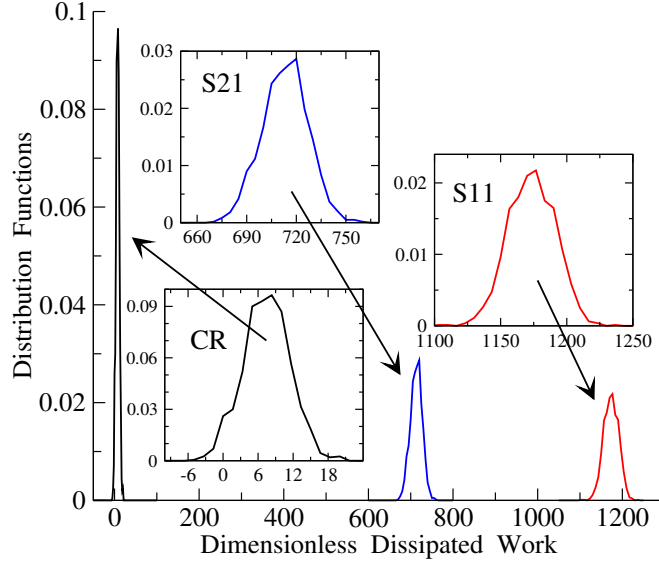


**Figure 6.3:** Distribution functions of the dimensionless dissipated work,  $\mathcal{W} - \Delta\mathcal{G}[4]$ , obtained for the high energy-barrier system using the S11 (red), S21 (blue) and CR (black) schedules. Distribution functions are also drawn in the insets to highlight their features. The data related to the S61 schedule, not reported here for the sake of clarity, show a consistent trend.

ries with dissipation less than 20, with a significant fraction of antidissipative trajectories ( $\mathcal{W} - \Delta\mathcal{G} < 0$ ), S11 and S21 schedules give very large dissipation, well above 1100 and 650, respectively. It is also interesting to note the greater variance (distribution width) obtained from stepwise schedules with respect to the CR one. According to expectations, the bias increases (right shift of the distributions) with the growth of the variance. In spite of the subtle details of the dissipated-work distributions that could be discussed, the most relevant information for our purposes is that, going gradually from stepwise to constant-rate time schedule for the thermodynamical control parameters (temperature and pressure in our case), the mean dissipated work decreases along with the variance of its distribution. In the framework of nonequilibrium simulations, these features of dissipation are known to enhance

accuracy in estimating free energy differences and, in general, average equilibrium quantities via eq. 6.15[34, 64]. Thus, from the perspective of nonequilibrium work theorems, this may account for the radically different uncertainties of the free energy estimates resulting from the four AIS schedules (see fig. 6.2). Qualitatively similar outcomes are gained from the low energy-barrier system.

## 6.5 Concluding remarks

We have proved the equivalence between the Annealed Importance Sampling (AIS) method for equilibrium sampling by Neal[140] (eq. 6.7) and the nonequilibrium path-ensemble average approach by Crooks[50]. This equivalence extends the amount of situations to which AIS idea can be applied, which goes beyond the mere thermal annealing processes. While resorting to AIS is expected to be useful in applications where simulated annealing is already in widespread use, such as structural determination from NMR data[90, 169], the extension to some other kind of annealing in a broader sense, like “mechanical annealing”, appears an intriguing perspective of the methodology. Here, the “mechanical” term should be thought as a generic way of involving mechanical variables (interatomic distances, torsion angles, volume, coordination numbers, etc.) to drive the system from an easily sampled state to another target state by means of nonequilibrium trajectories. In this respect, a representative example could be the folding process of a (bio)polymer exploiting the end-to-end distance. While sampling folded configurations may result very difficult at ordinary temperature, due to a manifold of free energy minima, the unfolded (elongated) state can present a less complex free energy surface, with evident benefits on the sampling. The second significant goal is to have shown that a thermal annealing based on a constant rate schedule outperforms stepwise protocols and that, for a given elapsed computer time, AIS performances are in general improved increasing the number of intermediate temperatures. This is indeed an important aspect for understanding the efficiency of the method, because thermal annealing is often thought and designed[127, 128] by alternating annealing steps to relaxing phases, the latter being performed with conventional molecular dynamics simulations.



---

## Computing free energy differences of configurational basins

---

### 7.1 Introduction

The Path-Linked Domains (PLD) approach is here developed and tested to estimate free energy differences between configurational states, following a procedure alternative to CDTS (chapter 5). The principles underlying both methodologies will be applied in the last chapter 8, in the framework of ligand receptor complexes. We consider hence a molecular system with many degrees of freedom, and classify a conformational state as a subensemble of the phase-space states accessible to the particles of the system. The relative chemical stability of two conformational states can always be formulated in terms of free energy difference, whose estimate can be made at different approximation degrees. In what follows, we introduce the concept of system microstate, corresponding to a specific vector  $\mathbf{x}$  in the  $3N$ -dimensional space of the coordinates relative to  $N$  atoms. A set of microstates sharing established chemical and structural properties will be referred to as a configuration. This may define a set of microstates relative to a given molecule which share specific structural features, but may identify also the chemical entity itself (such a definition may be employed in the study

of intramolecular and intermolecular reaction equilibria). Less generally, a configuration characterized by specific structural or geometrical features for a given chemical connectivity of the system will be called system conformation or conformational state. Note that such conformations can represent multiple configurations of stereoisomers, related to each other by some geometrical criterion, such as holding axial or equatorial substituents. Within this definition, a simple statistical mechanics calculation can then be used to estimate the free energy difference between the two conformational states. In a classical molecular system, the ultimate approach for calculating the free energy difference  $\Delta F$  between two conformational states at fixed temperature  $T$  and volume  $V$  involves the evaluation of two configuration integrals:

$$Q_A = \int_{\mathcal{V}_A} e^{-\beta U(\mathbf{x})} d\mathbf{x}, \quad Q_B = \int_{\mathcal{V}_B} e^{-\beta U(\mathbf{x})} d\mathbf{x}, \quad (7.1)$$

$$\Delta F_{AB} = F_B - F_A = -\beta^{-1} \ln \frac{Q_B}{Q_A}, \quad (7.2)$$

where  $U(\mathbf{x})$  is the system potential energy, dependent on the atomic coordinates  $\mathbf{x}$ , and  $\beta^{-1} = k_B T$ , with  $k_B$  being the Boltzmann constant. The symbols  $\mathcal{V}_A$  and  $\mathcal{V}_B$  represent the configurational volumes of the states  $A$  and  $B$ , which contain the microstates featuring the two states. We point out that eqs. 7.1 and 7.2 are even more general than what discussed here. In fact, they hold for a generic equilibrium  $A \rightleftharpoons B$  involving chemical species whose interconversion may occur through a chemical process, does not matter if it is a conformational change or a chemical reaction. These concepts have been widely applied to protein-ligand binding free energy calculations[126, 144, 203]. Direct evaluation of the ratio between configuration integrals for problems with high dimensionality is a challenge for most simulation methods also when developed for this specific aim. Indirect approaches utilizing various simulation techniques based on the free energy perturbation[119] and a smart Monte Carlo method termed jump-between-wells[170] have been used to calculate conformational free energy differences. Recently, methods based on non-instantaneous Monte Carlo moves[86, 147] have also been proposed, to overcome high free energy barriers connecting different configurational/conformational states of a system. The estimate of the ratio of configuration integrals  $Q_A$  and  $Q_B$  requires the definition of the conformational states as two subspaces of the whole hypersurface of the relevant torsional coordinates. For the simple case of the alanine dipeptide, used here as an example of our approach, the relevant torsional coordinates are the  $\phi$  and  $\psi$  angles of the peptide (fig. 7.1). In this space of

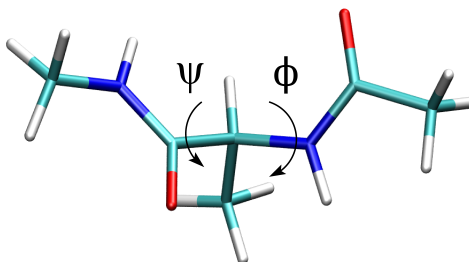


**Figure 7.1:** Representation of the  $\phi$  and  $\psi$  dihedral angles in the alanine dipeptide.

coordinates, in spite of the relative complexity of the free energy surface, we may identify several subspaces which correspond to different conformational domains. The hard issue of the problem is that, in order to calculate the configuration integrals, the system must explore the whole torsional space, with the risk of being trapped in some deep free energy minima with dramatic consequences on the quality of sampling. Even if this formidable task could be accomplished with effective sampling schemes such as serial or parallel generalized ensemble methods[149], it could be advantageous to restrain sampling (as much as possible) to the conformational volumes  $\mathcal{V}_A$  and  $\mathcal{V}_B$  for evaluating, separately, a sort of “site free energy contributions” for the two states. It is possible “to connect” these site free energies through potential of mean force (PMF) differences calculated along an established collective coordinate connecting the volume  $\mathcal{V}_A$  to  $\mathcal{V}_B$ , or viceversa. This is in summary the Path-Linked Domains (PLD) scheme proposed in the present. It is indeed possible to compute conformational free energy differences by sampling selectively the regions of interest and delineating a path connecting *a single couple of points* from one to the other configuration domain. This represents the fundamental variation from CDTs scheme (chapter 5), where two conformational states with arbitrary shape and size are connected by a series of intermediate domains in the space of the collective coordinates. In sec. 7.2, the method is presented. In sec. 7.3, alanine dipeptide system and simulation details are described, while results of simulation tests are reported in sec. 7.4. Concluding remarks are given in sec. 7.5.

## 7.2 Theory

Let us consider a dilute solution of a flexible molecule at constant volume and temperature, under the hypothesis that we are able to identify two conformational states of the molecule, say  $A$  and  $B$ , by means of some structural or energetical criterion, or a combination of the two. The constant  $K_{\text{eq}}$  of the chemical equilibrium  $A \rightleftharpoons B$  is defined as the ratio of the molar fractions  $n_A$  and  $n_B$  of the  $A$  and  $B$  states, *i.e.*,  $K_{\text{eq}} = n_B/n_A$ . From the statistical point of view,  $n_A$  and  $n_B$  correspond to the probabilities of finding the solute molecule in  $A$  and  $B$  conformations and therefore are proportional to the configuration integrals  $Q_A$  and  $Q_B$  of eq. 7.1. This allows us to write the equilibrium constant as  $K_{\text{eq}} = Q_B/Q_A$  and the free energy difference of the two conformers as  $\Delta F_{AB} = -\beta^{-1} \ln(Q_B/Q_A) = -\beta^{-1} \ln K_{\text{eq}}$ . Therefore, the basic quantities needed to evaluate  $K_{\text{eq}}$ , or equivalently  $\Delta F_{AB}$ , are the configuration integrals  $Q_A$  and  $Q_B$ . Calculating these integrals by, *e.g.*, conventional equilibrium simulations or accelerated sampling techniques[149, 188] may not be easy, especially due to the difficulty of reaching converging estimates in the high dimensional space of the atomic coordinates  $\mathbf{x}$  of the system[69]. In practice, we cannot evaluate numerically the configuration integrals, but only their ratio relative to subsets  $\mathcal{V}_A$  and  $\mathcal{V}_B$  of the atomic coordinates explored in the same simulation. As conformational states  $A$  and  $B$  refer to the same molecule, it is generally easier to define configuration domains in the  $M$ -dimensional space of independent dihedral angles characterizing the conformers ( $M = 2$  in the case of the alanine dipeptide; see fig. 7.1). Thus, defining the vector of the relevant dihedral angles as[5]  $\boldsymbol{\zeta}(\mathbf{x}) = (\zeta_1(\mathbf{x}), \zeta_2(\mathbf{x}), \dots, \zeta_M(\mathbf{x}))$ , the configuration integral  $Q_A$  can be written as

$$Q_A = \int_{D_A} \int_{\mathcal{V}} \delta(\mathbf{z} - \boldsymbol{\zeta}(\mathbf{x})) e^{-\beta U(\mathbf{x})} d\mathbf{x} d\mathbf{z}, \quad (7.3)$$

where the integral over  $\mathbf{x}$  is extended to the whole space  $\mathcal{V}$  of the atomic Cartesian coordinates and the integral over  $\mathbf{z}$  is extended to a limited domain  $D_A$  of the dihedral angle coordinates,  $\zeta_1(\mathbf{x})$ ,  $\zeta_2(\mathbf{x})$ , etc., for which the molecule is classified to belong to the conformational state  $A$ . Note that the integral over  $\mathbf{x}$  implicitly includes integration over the solvent coordinates. In eq. 7.3, we recognize the PMF as a function of the dihedral angles:

$$\Phi(\mathbf{z}) = -\beta^{-1} \ln \left( \int_{\mathcal{V}} \delta(\mathbf{z} - \boldsymbol{\zeta}(\mathbf{x})) e^{-\beta U(\mathbf{x})} d\mathbf{x} \right). \quad (7.4)$$

In general, the PMF is a function of a multidimensional vector  $\mathbf{z}$  representing the dihedral angles. Although the dimensions of  $\mathbf{z}$  can be very large in dependence of the size and flexibility of the molecule, we are often interested to a limited set of dihedral angles, greatly simplifying the problem (*e.g.*, the  $\phi$  and  $\psi$  angles of a peptide). This reduction of dimensionality does not lie in some intrinsic property of the system, but rather in the paradigm chosen to describe the physics of the system. Evaluation of the free energy difference between two states is a rather general problem[53, 120, 144, 205], which is related not only to sampling issues, but also to the arbitrariness of the criterion adopted to define the “state of a system”. In the following, we will not take care on how the  $\mathbf{z}$  space is defined, but we will develop the treatment under the assumption that such a space can somehow be specified. Moreover, we also assume that some criterion can be found for defining and choosing the conformational domain  $D_A$  appearing into eq. 7.3. These assumptions make the treatment quite general, so that referring to torsional degrees of freedom must only be viewed as a way of connecting the theory to the most important situation in which, we believe, this method could be applied. Upon substitution of eq. 7.4 into eq. 7.3, we obtain

$$Q_A = \int_{D_A} e^{-\beta\Phi(\mathbf{z})} d\mathbf{z}. \quad (7.5)$$

Therefore, the problem can be traced back to the calculation of  $\Phi(\mathbf{z})$  and then to numerically integrate its exponential  $\exp(-\beta\Phi(\mathbf{z}))$  over the domain  $D_A$  (or  $D_B$ , in the case of  $Q_B$ ). The calculation of the integral of eq. 7.5 could be computationally very expensive even in relatively simple molecules, basically due to the rapid increase of the number of torsional degrees of freedom with the number of atoms in the molecule. This leads to a manifold of minima in the  $\Phi(\mathbf{z})$  hypersurface, which need to be properly sampled in a computer simulation. For example, in n-alkanes, the PMF minima roughly increase with the number  $c$  of carbon atoms as  $3^{c-3}$ , including symmetrically equivalent conformations. The representation of the  $\Phi(\mathbf{z})$  surface of n-pentane as a function of the two inner C-C-C-C dihedral angles, obtained from a constant-pressure constant-temperature MD simulation of 64 molecules at room conditions, is reported in fig. 7.2A. Minima, corresponding to the conformers  $tt$ ,  $tg$ ,  $gt$ ,  $tg'$ ,  $g't$ ,  $gg'$ ,  $g'g$ ,  $g'g'$  and  $gg$ , appear in well-defined regions of the PMF surface. Supposing that we are interested to the free energy difference between, say,  $tt$  and  $tg$  conformers, we could select the integration domains  $D_{tt}$  and  $D_{tg}$  as the portions of the  $\mathbf{z}$  space around the corresponding minima, such that  $\Phi(\mathbf{z}) < 10 \text{ kJ mol}^{-1}$ . This would give the reduced

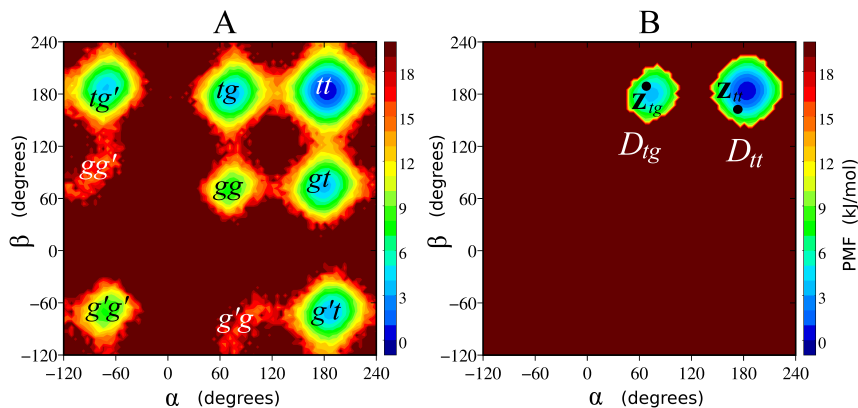


**Figure 7.2:** *Panel A:*  $\Phi(\mathbf{z})$  surface of n-pentane as a function of the two inner C-C-C-C torsion angles  $\alpha$  and  $\beta$ , obtained from a constant-pressure constant-temperature simulation of 64 molecules at room conditions. *Panel B:* integration domains  $D_{tt}$  and  $D_{tg}$ , defined as the portions of the  $\mathbf{z}$  space around the corresponding minima such that  $\Phi(\mathbf{z})$  is less than  $10 \text{ kJ mol}^{-1}$  above the minimum inside the  $D_{tt}$  domain. Domains  $D_{tg}/D_{tt}$  and points  $\mathbf{z}_{tg}/\mathbf{z}_{tt}$  correspond to  $D_A/D_B$  and  $\mathbf{z}_a/\mathbf{z}_b$  of eq. 7.6, respectively.

conformational domains of the  $tt$  and  $tg$  states shown in fig. 7.2B. Of course, a geometrical criterion based on the accessible values of the  $\alpha$  and  $\beta$  dihedral angles (*e.g.*,  $0^\circ < \alpha < 120^\circ$  and  $120^\circ < \beta < 240^\circ$  for the  $tg$  state) would also be suitable to establish the conformational states of interest. However, independently of the criterion adopted to define the  $\mathbf{z}$  domains, an estimate of the whole PMF should be provided to evaluate the configuration integrals, which could result a too expensive calculation. Alternatively, one could compute the ratio  $Q_B/Q_A$  with separate MD simulations. The procedure is based on a manipulated expression of  $\Delta F_{AB}$ , obtained by applying eq. 7.5 into eq. 7.2:

$$\Delta F_{AB} = \Delta \Phi_{AB} - \beta^{-1} \ln \left( \frac{\int_{D_B} e^{\beta[\Phi(\mathbf{z}_b) - \Phi(\mathbf{z})]} d\mathbf{z}}{\int_{D_A} e^{\beta[\Phi(\mathbf{z}_a) - \Phi(\mathbf{z})]} d\mathbf{z}} \right), \quad (7.6)$$

where  $\Delta \Phi_{AB} = \Phi(\mathbf{z}_b) - \Phi(\mathbf{z}_a)$ , with  $\mathbf{z}_a$  and  $\mathbf{z}_b$  being two any points of the conformational space located inside the  $D_A$  and  $D_B$  domains, respectively. In the n-pentane example, these

points could be, for instance, those reported in fig. 7.2B. The integrals of eq. 7.6 can be calculated by two independent MD simulations supplied with biasing potentials[188], which enforce, in turn, the sampling of restricted regions,  $R_A$  and  $R_B$ , encompassing  $D_A$  and  $D_B$  domains. We will denote these MD simulations, as eq- $R_A$  and eq- $R_B$ . In practice, the integrals into eq. 7.6 are approximated by sums over points taken on a regular grid in the  $\mathbf{z}$  space. Thus, for example,  $\int_{D_A} e^{\beta[\Phi(\mathbf{z}_a)-\Phi(\mathbf{z})]} d\mathbf{z} \simeq \sum_{\mathbf{z}_i \in D_A} e^{\beta[\Phi(\mathbf{z}_a)-\Phi(\mathbf{z}_i)]} \Delta\mathbf{z}$ , where the sum is limited to the grid points inside the  $D_A$  domain and  $\Delta\mathbf{z}$  is the finite volume whose dimensions correspond to the resolution sizes employed to estimate  $\Phi(\mathbf{z})$ . The other integral of eq. 7.6 is computed in analogous way. The possibility of computing the integrals of eq. 7.6 with independent MD simulations relies on the fact that they involve exponential functions of relative rather than absolute PMFs, and therefore do not depend on arbitrary additive constants. Choosing  $\mathbf{z}_a$  and  $\mathbf{z}_b$  inside  $D_A$  and  $D_B$  domains is necessary because it allows estimating the free energy differences  $\Phi(\mathbf{z}_a) - \Phi(\mathbf{z})$  and  $\Phi(\mathbf{z}_b) - \Phi(\mathbf{z})$  with single MD simulations that limit sampling to those domains. Actually, a less stringent condition is required in choosing  $\mathbf{z}_a$  and  $\mathbf{z}_b$ : they must be placed inside the  $R_A$  and  $R_B$  domains, respectively, namely where it is possible to evaluate the PMF via eq- $R_A$  and eq- $R_B$  simulations. In any case, in order to get statistically accurate outcomes,  $\mathbf{z}_a$  and  $\mathbf{z}_b$  should belong to intensively sampled regions of the conformational space. The PMF difference  $\Delta\Phi_{AB}$  can be calculated independently, by any method to estimate the PMF along an established collective coordinate[41, 69]. In this study, we have used nonequilibrium steered MD simulations[151], but other approaches based on equilibrium or quasi-equilibrium schemes[38, 121, 133, 188] are suitable as well. We will refer to these simulations as Linking Path (LP) simulations. A simplified representation of the PLD scheme is reported in fig. 7.3. We stress that the actual advantage of expressing  $\Delta F_{AB}$  as in eq. 7.6 relies on the possibility of calculating configuration integrals without performing a complete sampling of the conformational space, *i.e.*, without determining the whole  $\Phi(\mathbf{z})$  surface. We will apply eq. 7.6 to the calculation of the free energy difference between conformational basins of the alanine dipeptide, by the use of steered MD simulations to calculate  $\Delta\Phi_{AB}$  and umbrella sampling[188] (US) simulations for the configuration integrals. A comparable simulation procedure has been devised to compute binding free energies of, *e.g.*, protein-ligand complexes[53, 144].

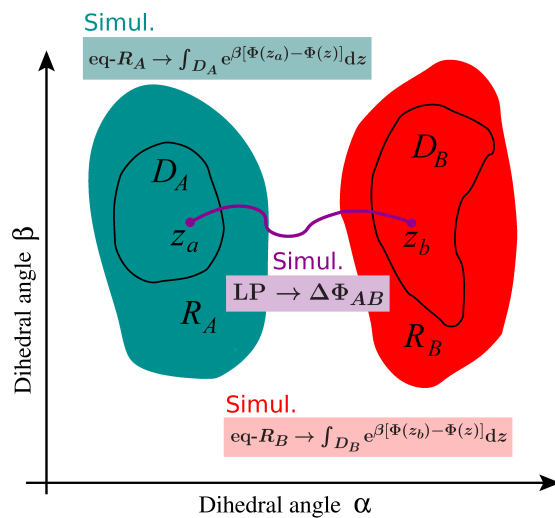


**Figure 7.3:** Schematic representation of the PLD protocol. The axes report the components  $\alpha$  and  $\beta$  of a generic bidimensional vector  $\mathbf{z}$  describing the degrees of freedom of interest. Green and red colors denote the configurational regions  $R_A$  and  $R_B$ , respectively, visited by the system during the equilibrium simulations  $\text{eq-}R_A$  and  $\text{eq-}R_B$ . The conformational domains  $D_A$  and  $D_B$  are enclosed by solid black lines. The magenta line represents the linking path, employed in LP simulations, connecting the points  $\mathbf{z}_a$  and  $\mathbf{z}_b$ .  $\text{eq-}R_A$ ,  $\text{eq-}R_B$  and LP simulations are used to compute the quantities entering eq. 7.6 (also reported in the above panel).

## 7.3 System and simulation details

### 7.3.1 System

Alanine dipeptide consists of an alanine residue terminated by acetyl and N-methyl capping groups (fig. 7.1). The small dimensions together with a quite complex conformational organization make this peptide perhaps the simplest model bearing most features of polypeptides. Its peculiar behavior is due to the presence of the flexible  $\phi$  and  $\psi$  dihedral angles and



of functional groups able to establish both intra and intermolecular hydrogen bonds[21, 180]. Although there are only two conformationally relevant degrees of freedom, *i.e.*, the  $\phi$  and  $\psi$  angles, the free energy surface  $\Phi(\mathbf{z})$  as a function of these angles,  $\mathbf{z} \equiv (\phi, \psi)$ , is rather complex, presenting various local minima and maxima. The  $\Phi(\mathbf{z})$  surface obtained from an US simulation taken from ref.[133] is reported in fig. 7.4. Thanks to its modest size,

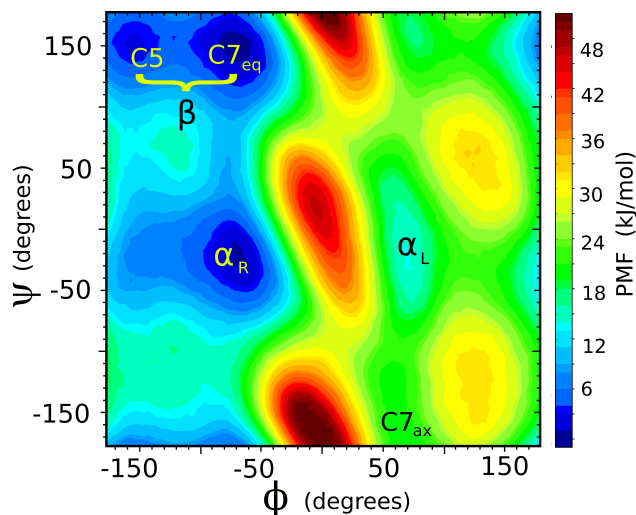


**Figure 7.4:**  $\Phi(\mathbf{z})$  surface of the alanine dipeptide as a function of the  $\phi$  and  $\psi$  dihedral angles. The relevant free energy minima are labeled on the panel. In this study, microstates into  $C5$  and  $C7_{eq}$  minima are considered to belong to a unique system configuration, labeled  $\beta$ . Calculations have been performed with an US simulation[133].

alanine dipeptide has been often employed as a benchmark system[67] to verify sampling methods[133, 180, 186, 198] or to evaluate the accuracy of force fields[57]. We apply the PLD scheme to calculate free energy differences between conformational states, or conformers, whose characterization in terms of  $\phi$  and  $\psi$  angles is reported in fig. 7.4. Specifically, the target free energy differences are  $F_{\alpha_L} - F_{\beta}$  and  $F_{\alpha_L} - F_{\alpha_R}$ . Note that the conformers  $C5$  and  $C7_{eq}$ , well distinguishable as separate free energy basins in  $\Phi(\mathbf{z})$ , are considered

here as a unique conformational state, indicated with  $\beta$ . A quantitative definition of the conformational states related to  $\alpha_L$ ,  $\alpha_R$  and  $\beta$  minima will be given in sec. 7.3.3. In order to get a feedback on the efficiency of the PLD scheme, the outcomes are compared to those obtained from a Serial Generalized Ensemble (SGE) simulation[146], whose performances are almost equivalent to those of the popular replica-exchange method[38, 39].

### 7.3.2 Shared simulation setup

In this study, several MD simulations of either equilibrium or nonequilibrium type have been carried out. The equilibrium simulations are (i) the eq- $R_A$  and eq- $R_B$  simulations, realized with conventional and US methods (some further details will be given in sec. 7.3.3), (ii) the simulations with restrained  $\phi$  and  $\psi$  dihedral angles aimed at producing the initial microstates for the steered MD simulations and (iii) the SGE simulation performed for a comparative aim. Nonequilibrium simulations are the steered MD simulations (LP simulations) employed to compute the quantity  $\Delta\Phi_{AB}$  into eq. 7.6. All these MD simulations share the setup described in the following. The system consists of one alanine dipeptide and 288 water molecules simulated in the constant volume and temperature thermodynamic ensemble using the program ORAC[134]. A cubic box of 21 Å side-length with standard periodic boundary conditions has been adopted. The temperature control (298 K) has been achieved through a Nosé-Hoover thermostat[99]. The dipeptide is modeled by the AMBER03 force field[57], while TIP3P potential has been used for water[112]. Electrostatics has been accounted for by the smooth particle mesh Ewald method[60], adopting a fourth order B-spline interpolation polynomial for the charges, an Ewald parameter of 0.43 Å<sup>-1</sup> and a grid spacing of 0.875 Å for the fast Fourier transform calculation of the charge weighted structure factor. A cutoff distance of 9.5 Å has been set for nonbonded interactions. A five time-step r-RESPA integrator[191] has been used for integrating the equations of motion.

### 7.3.3 Path-Linked Domains scheme

Owing to the high barriers featuring the  $\{\phi, \psi\}$  free energy surface of the alanine dipeptide and to the large free energy difference between the  $\alpha_L$  and the  $\beta/\alpha_R$  conformations[6] (see fig. 7.4), statistical sampling generated from conventional MD simulations does not allow for quantitative free energy estimates[38]. PLD approach to the free energy difference

between  $\alpha_L$  and  $\beta/\alpha_R$  conformational states, *i.e.*  $F_{\alpha_L} - F_{\beta/\alpha_R}$ , consists of three independent, and hence simultaneously affordable, stages: (i) an equilibrium MD simulation in which  $\phi$  and  $\psi$  are restrained within a region  $R_{\beta/\alpha_R}$  encompassing the  $D_{\beta/\alpha_R}$  conformational domain (the eq- $R_{\beta/\alpha_R}$  simulation in our terminology); (ii) the analogous eq- $R_{\alpha_L}$  simulation related to the  $\alpha_L$  conformational state; (iii) a bidirectional set of nonequilibrium steered MD simulations, the LP simulations, for estimating the difference between  $\Phi(\mathbf{z})$  values computed at established points,  $\mathbf{z}_{\beta/\alpha_R}$  and  $\mathbf{z}_{\alpha_L}$ , inside the  $R_{\beta/\alpha_R}$  and  $R_{\alpha_L}$  regions.

### Definition of conformational states and eq- $R_x$ simulations

The first problem to handle is to formulate operational definitions of the conformational states of interest, namely to establish the exact meaning of  $\beta$ ,  $\alpha_R$  and  $\alpha_L$  conformational states. Obviously, such definitions identify the  $D_\beta$ ,  $D_{\alpha_R}$  and  $D_{\alpha_L}$  domains and are somehow arbitrary, because, in general,  $\Phi(\mathbf{z})$  varies smoothly with the set of coordinates  $\mathbf{z} \equiv (\phi, \psi)$  chosen to describe the system states. We define the conformational state  $D_{\alpha_R}$  as follows

$$D_{\alpha_R} \begin{cases} \mathbf{z} \equiv (\phi, \psi) \in \mathcal{M}_{\alpha_R} \cap \mathcal{N}_{\alpha_R} \\ \mathcal{M}_{\alpha_R} = \{\mathbf{z} : -180^\circ \leq \phi \leq 0^\circ \wedge -90^\circ \leq \psi \leq 90^\circ\} \\ \mathcal{N}_{\alpha_R} = \{\mathbf{z} : \Phi(\mathbf{z}) - \min(\Phi(\mathbf{z}')) < 10 \text{ kJ/mol} \wedge \mathbf{z}' \in \mathcal{M}_{\alpha_R}\} \end{cases} \quad (7.7)$$

Analogous definitions are adopted for  $D_\beta$  and  $D_{\alpha_L}$ :

$$D_\beta \begin{cases} \mathbf{z} \equiv (\phi, \psi) \in \mathcal{M}_\beta \cap \mathcal{N}_\beta \\ \mathcal{M}_\beta = \{\mathbf{z} : -180^\circ \leq \phi \leq 0^\circ \wedge -180^\circ \leq \psi \leq -100^\circ\} \cup \\ \{\mathbf{z} : -180^\circ \leq \phi \leq 0^\circ \wedge 100^\circ \leq \psi \leq 180^\circ\} \cup \\ \{\mathbf{z} : 120^\circ \leq \phi \leq 180^\circ \wedge 100^\circ \leq \psi \leq 180^\circ\} \\ \mathcal{N}_\beta = \{\mathbf{z} : \Phi(\mathbf{z}) - \min(\Phi(\mathbf{z}')) < 10 \text{ kJ/mol} \wedge \mathbf{z}' \in \mathcal{M}_\beta\} \end{cases} \quad (7.8)$$

$$D_{\alpha_L} \begin{cases} \mathbf{z} \equiv (\phi, \psi) \in \mathcal{M}_{\alpha_L} \cap \mathcal{N}_{\alpha_L} \\ \mathcal{M}_{\alpha_L} = \{\mathbf{z} : 0^\circ \leq \phi \leq 120^\circ \wedge -100^\circ \leq \psi \leq 100^\circ\} \\ \mathcal{N}_{\alpha_L} = \{\mathbf{z} : \Phi(\mathbf{z}) - \min(\Phi(\mathbf{z}')) < 10 \text{ kJ/mol} \wedge \mathbf{z}' \in \mathcal{M}_{\alpha_L}\} \end{cases} \quad (7.9)$$

Denoting with “x” a generic label  $\alpha_R$ ,  $\alpha_L$  or  $\beta$ , it is worth noting that, for a given conformational state  $D_x$ , the definition of the region  $\mathcal{N}_x$  does not depend on the (arbitrary) additive

constant featuring  $\Phi(\mathbf{z})$ , because it relies on a PMF difference rather than an absolute PMF. Here,  $\Phi(\mathbf{z})$  in a region  $R_x$  is computed through the corresponding eq- $R_x$  simulation. In particular, to determine  $D_{\alpha_R}$  and  $D_\beta$  it was enough to perform a unique conventional MD simulation (*i.e.*, without biasing potential), because the alanine dipeptide has been found to span a wide conformational basin, larger than the extended region  $(\mathcal{M}_{\alpha_R} \cap \mathcal{N}_{\alpha_R}) \cup (\mathcal{M}_\beta \cap \mathcal{N}_\beta)$ . Therefore, the simulations eq- $R_{\alpha_R}$  and eq- $R_\beta$  are actually the same. Starting from a dipeptide conformation such that  $\mathbf{z} \simeq (-45.7^\circ, 152.7^\circ)$ , a simulation lasting 156 ns explored the region highlighted in green color in fig. 7.5A, which corresponds to  $R_{\alpha_R}$  or, equivalently,  $R_\beta$  (the  $R_A$  domain in fig. 7.3). The conformational states  $D_{\alpha_R}$  and  $D_\beta$  resulting from applying eqs. 7.7 and 7.8 are shown with brown color in fig. 7.5A. The PMF has been computed

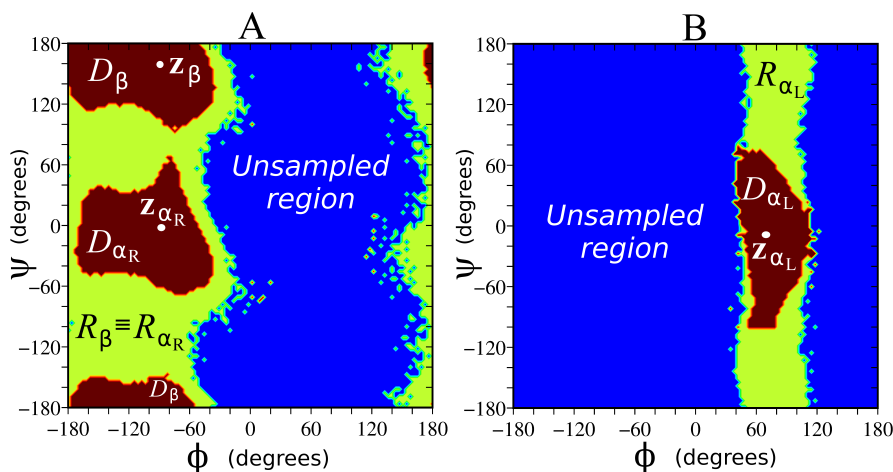


**Figure 7.5:** Green color:  $R_x$  regions explored during eq- $R_x$  simulations. Brown color:  $D_x$  conformational domains resulting from applying criteria of eqs. 7.7, 7.8 and 7.9. Blue color:  $\mathbf{z}$  configurations unexplored during the eq- $R_x$  simulations. Note that the  $R_x$  regions encompass the  $D_x$  domains. The  $\mathbf{z}_\beta$ ,  $\mathbf{z}_{\alpha_R}$  and  $\mathbf{z}_{\alpha_L}$  points connected through LP simulations are also shown. *Panel A:* data related to the eq- $R_{\alpha_R}$  simulation (the same as eq- $R_\beta$ ). *Panel B:* data related to the eq- $R_{\alpha_L}$  simulation.

from the two-dimensional  $g(\mathbf{z})$  distribution function as

$$\Phi(\mathbf{z}) = -\beta^{-1} \ln g(\mathbf{z}), \quad (7.10)$$

with angular resolution  $\Delta\phi = \Delta\psi = 3.6^\circ$ . The  $D_{\alpha_L}$  domain has been achieved through an US simulation (eq- $R_{\alpha_L}$ ) applying the biasing potential  $U_{\text{us}}(\mathbf{x}) = k_{\text{us}}(\phi(\mathbf{x}) - \phi_0)^2$ , where  $\phi(\mathbf{x})$  is the  $\phi$  dihedral angle of the microstate  $\mathbf{x}$ ,  $\phi_0 = 75^\circ$  and  $k_{\text{us}} = 1.27 \cdot 10^{-2}$  kJ mol $^{-1}$  degrees $^{-2}$ . This setup leads to sample the  $R_{\alpha_L}$  region shown in green color in fig. 7.5B. The corresponding  $D_{\alpha_L}$  domain (from eq. 7.9) is highlighted in brown color in fig. 7.5B. The  $\Phi(\mathbf{z})$  surface is recovered using eq. 7.10, with  $g(\mathbf{z})$  being computed through the reweighting formula[188]

$$g(\mathbf{z}) = \frac{\sum_{i=1}^{N_s} \delta(\mathbf{z} - \zeta(\mathbf{x}_i)) e^{\beta U_{\text{us}}(\mathbf{x}_i)}}{\sum_{j=1}^{N_s} e^{\beta U_{\text{us}}(\mathbf{x}_j)}}, \quad (7.11)$$

where  $\zeta(\mathbf{x}_i) \equiv (\phi(\mathbf{x}_i), \psi(\mathbf{x}_i))$  is the vector of the dihedral angles associated with the  $\mathbf{x}_i$  microstate and  $N_s$  is the number of microstates sampled in the US simulation. The PMFs limited to the conformational states  $D_{\alpha_R}$  and  $D_\beta$  are drawn in fig. 7.6A, while the PMF limited to the conformational state  $D_{\alpha_L}$  is shown in fig. 7.6B. Hence, both figs. 7.6A and 7.6B display the free energy boundaries employed in eqs. 7.7, 7.8 and 7.9 to define  $\mathcal{N}_{\alpha_R}$ ,  $\mathcal{N}_\beta$ , and  $\mathcal{N}_{\alpha_L}$ , respectively. We notice that the latter PMF is shifted by an arbitrary constant with respect to the former ones, since it is yielded by an independent MD simulation.

### LP simulations

As discussed in sec. 5.2, free energy surfaces computed from independent MD simulations, *i.e.* the eq- $R_x$  simulations, are quantitatively consistent each to the other only after determining the PMF difference between two any arbitrary points of such surfaces, (the  $\mathbf{z}_a$  and  $\mathbf{z}_b$  points of eq. 7.6). For the three conformational states under consideration, we have chosen  $\mathbf{z}_{\alpha_R} \equiv (-90^\circ, 0^\circ)$ ,  $\mathbf{z}_\beta \equiv (-90^\circ, 160^\circ)$  and  $\mathbf{z}_{\alpha_L} \equiv (70^\circ, 0^\circ)$ . A view of their positions within the respective  $D_x$  domains is reported in both figs. 7.5 and 7.6. Once these points are defined, numerical computation of the integrals of eq. 7.6 is straightforward. To calculate  $\Delta\Phi_{\alpha_R, \alpha_L} = \Phi(\mathbf{z}_{\alpha_L}) - \Phi(\mathbf{z}_{\alpha_R})$ , namely the  $\Delta\Phi_{AB}$  quantity of eq. 7.6, we have used steered MD simulations (LP simulations) linking  $\mathbf{z}_{\alpha_L}$  to  $\mathbf{z}_{\alpha_R}$  with a linear path. Analogous treatment has been adopted for  $\Delta\Phi_{\beta, \alpha_L}$ . Specifically, an external time-dependent potential

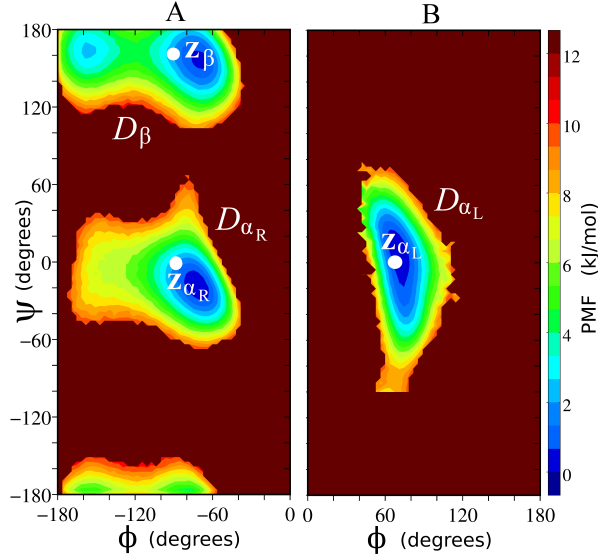


**Figure 7.6:** *Panel A:*  $D_{\alpha_R}$  and  $D_\beta$  conformational domains, recovered from the eq- $R_{\alpha_R}$  simulation (the same as eq- $R_\beta$ ), are highlighted together with the corresponding  $\Phi(\mathbf{z})$  free energy profiles. The  $\mathbf{z}_\beta$  and  $\mathbf{z}_{\alpha_R}$  points are also shown. *Panel B:* same information as panel A recovered from the eq- $R_{\alpha_L}$  simulation. Different panels are used for data from eq- $R_{\beta/\alpha_R}$  and eq- $R_{\alpha_L}$  simulations because PMFs are shifted by an arbitrary constant.

$E(\mathbf{z}, t)$  is applied in a series of nonequilibrium simulated trajectories to guide the coordinate  $\mathbf{z}$  from an initial value  $\mathbf{z}_i$  to the final value  $\mathbf{z}_f$ , according to a defined linear time schedule:

$$E(\mathbf{z}, t) = k_{\text{LP}} \left| \mathbf{z} - \mathbf{z}_i - \frac{t}{\tau_{\text{pull}}} (\mathbf{z}_f - \mathbf{z}_i) \right|^2, \quad (7.12)$$

where  $k_{\text{LP}} = 0.255 \text{ kJ mol}^{-1} \text{ degrees}^{-2}$  and the pulling time  $\tau_{\text{pull}}$  is 9 ps. Clearly,  $\mathbf{z}_i$  and  $\mathbf{z}_f$  may correspond, respectively, to  $\mathbf{z}_{\beta/\alpha_R}$  and  $\mathbf{z}_{\alpha_L}$  or viceversa, depending on the pulling direction. Initial system microstates of the guided trajectories have been picked at regular time intervals of 0.6 ps from two equilibrium MD simulations, one for each pulling direction, enforcing an external potential of  $k_{\text{LP}}|\mathbf{z} - \mathbf{z}_i|^2$  type. Then, 6000 trajectories for each direction

of the process have been carried out by using inverse time schedules. For each realization of the process, the work performed on the system is computed as

$$W = \int_0^{\tau_{\text{pull}}} \frac{\partial E(\mathbf{z}, t)}{\partial t} dt. \quad (7.13)$$

The two sets of works are exploited to estimate  $\Delta\Phi_{\alpha_R, \alpha_L}$  and  $\Delta\Phi_{\beta, \alpha_L}$  according to the bidirectional PMF estimator by Minh and Adhib (eq.10 of ref.[137]; almost identical outcomes have been obtained by using the PMF estimator of ref.[25]).

### 7.3.4 Serial generalized ensemble simulation

Although several implementations of SGE simulation techniques have been provided during the years[95, 102, 129, 138, 150], in our comparative analysis we have adopted the scheme proposed in Refs.[38, 146], which is based on a “on the fly” update of ensemble free energies according to the Bennett acceptance ratio method[18, 174]. The simulation run considered here results from extending in time the SGE simulation reported in ref.[38], to which reference is made for a detailed description of the simulation setup. In brief, the SGE simulation has been performed with 8 replicas of the system evolving independently through a generalized ensemble consisting of 8 thermodynamic ensembles, which differ for the intramolecular potential energy of the alanine dipeptide, progressively scaled from 1 to 0.01 (for details on partitioning of the scaling factors among the thermodynamic ensembles, see Table I of ref.[38]). The simulation time per replica is 252 ns. Since the simulation allows exploring the whole  $\{\phi, \psi\}$  space, it is possible to compute every possible free energy difference  $\Delta F_{AB}$  by direct integration of an exponential function of  $\Phi(\mathbf{z})$ :

$$\Delta F_{AB} = -\beta^{-1} \ln \left( \frac{\int_{D_B} e^{-\beta\Phi(\mathbf{z})} d\mathbf{z}}{\int_{D_A} e^{-\beta\Phi(\mathbf{z})} d\mathbf{z}} \right). \quad (7.14)$$

Note however that, in the calculation of  $\Phi(\mathbf{z})$ , each microstate contributes according to a variable weight factor. Each weight is determined from the simulation by using the multistate Bennett acceptance ratio methodology[175] and depends on which thermodynamic ensemble, out of the 8 forming the generalized ensemble, the corresponding microstate is picked.

## 7.4 Simulation tests

The purpose of the present simulation tests is to compare the performances of the PLD scheme to those of a SGE simulation[38, 146], in relation to estimates of conformational free energy differences of alanine dipeptide conformers in aqueous solution. In this respect, it is worth noting that the adopted SGE methodology has already been proved to be comparable in accuracy to the popular replica exchange method[94, 104, 179, 182, 183, 187], as the estimate of  $\Phi(\mathbf{z})$  is concerned[38]. Moreover, we point out that it is not our aim here to present the PLD scheme as the best approach to study conformational distributions in peptides, or biopolymers in general, also because no systematic comparison is provided with other important methods for free energy calculations[41]. Rather, we limit our conclusions to observe that, in the treatment of small peptides, the PLD scheme outperforms the quite popular family of generalized ensemble simulations, offering interesting perspectives, alternative to methodologies already in use, for free energy calculations. Specifically, we report on a comparative analysis of PLD and SGE methods concerning the calculation of free energy differences as a function of sampling times, assuming the outcomes of the US simulation reported in ref.[133] as a reference. The computer time  $\tau_{\text{cdlp}}$  needed to apply the PLD scheme is the sum of the times  $\tau_A$ ,  $\tau_B$  and  $\tau_{\text{LP}}$  associated with the eq- $R_A$ , eq- $R_B$  and LP simulations, respectively. The time  $\tau_{\text{LP}}$  can, in turn, be viewed as a sum of various contributions:  $\tau_{\text{LP}} = 2N(\tau_s + \tau_{\text{pull}})$ , where  $\tau_s = 0.6$  ps is the time needed to sample a single system microstate taken to initialize a pulling trajectory (the same  $\tau_s$  is used for forward and backward directions),  $\tau_{\text{pull}} = 9$  ps is the pulling time defined in eq. 7.12 and  $N$  is the number of pulling trajectories in one direction; although not necessary, we have taken the same number of forward and backward trajectories. In fig. 7.7, we show  $\Delta\Phi_{\alpha_R, \alpha_L}$  and  $\Delta\Phi_{\beta, \alpha_L}$  contributions to  $\Delta F_{\alpha_R, \alpha_L}$  and  $\Delta F_{\beta, \alpha_L}$  (eq. 7.6), respectively, as a function of the number of pulling trajectories  $N$ . In both cases, good convergence appears to be reached with about few thousands of trajectories per direction. However, even adopting  $N = 200$  (see arrows in fig. 7.7), estimates within only  $0.2$  kJ mol $^{-1}$  about the limit values of  $\Delta\Phi_{\alpha_R, \alpha_L} \simeq 12.0$  kJ mol $^{-1}$  and  $\Delta\Phi_{\beta, \alpha_L} \simeq 12.4$  kJ mol $^{-1}$  are obtained. On the basis of these results, we may consider  $N = 4000$  as the number of forward and backward trajectories beyond which convergent estimates are gained. Therefore, in order to simplify the analysis of the dependence of  $\Delta F_{\alpha_R, \alpha_L}$  and  $\Delta F_{\beta, \alpha_L}$  on the sampling time, we have fixed  $\tau_{\text{LP}}$  to 76.8 ns, which is



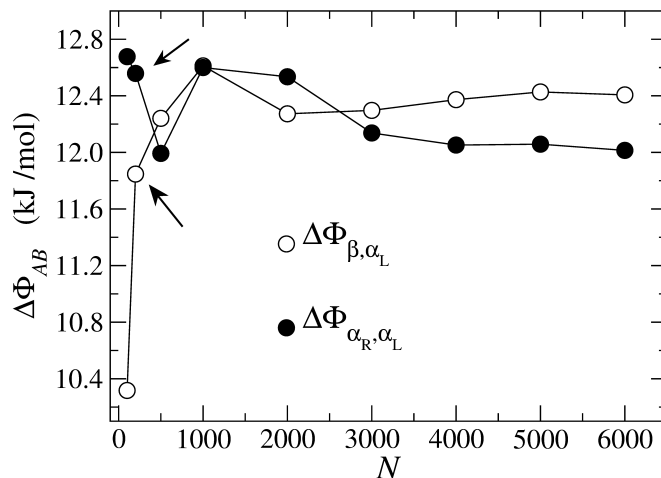


**Figure 7.7:** PMF differences  $\Delta\Phi_{\alpha_R,\alpha_L}$  and  $\Delta\Phi_{\beta,\alpha_L}$  as functions of the number  $N$  of pulling trajectories, estimated from LP simulations. The arrows indicate the data corresponding to  $N = 200$ . Lines are guides for the eyes.

the time needed to realize 4000 forward and backward pulling trajectories. Note that  $\tau_{LP}$ ,  $\tau_A$  and  $\tau_B$ , as well as  $\tau_{sge}$ , *i.e.* the total SGE simulation time[7], do not account for the equilibration time. A comparison of the efficiency of PLD and SGE methods is given in fig. 7.8, where we report  $\Delta F_{\alpha_R,\alpha_L}$  and  $\Delta F_{\beta,\alpha_L}$  as functions of the sampling times  $\tau_{cdlp}$  and  $\tau_{sge}$ . The free energy differences estimated through the US simulation[133] by using eq. 7.14 are also shown in the figure as a reference. We note that, while free energy deviations of PLD from US do not exceed  $0.2 \text{ kJ mol}^{-1}$ , SGE estimates of  $\Delta F_{\beta,\alpha_L}$  and  $\Delta F_{\alpha_R,\alpha_L}$  deviate by about  $0.5$  and  $1 \text{ kJ mol}^{-1}$ , respectively. This clearly points to a better accuracy of the PLD scheme with respect to the SGE approach. Such a conclusion is supported from a further observation leading to infer poor convergence of SGE calculations. In fact, in spite of the large SGE sampling time ( $\tau_{sge}$ ) reached in our calculations, which is nearly one order of magnitude greater than  $\tau_{cdlp}$ , the dependence of SGE free energies on  $\tau_{sge}$  is clearly featured by a monotonically increasing trend. However, although SGE free energy estimates appear poorly convergent from a comparative standpoint, they are indeed satisfactory, as

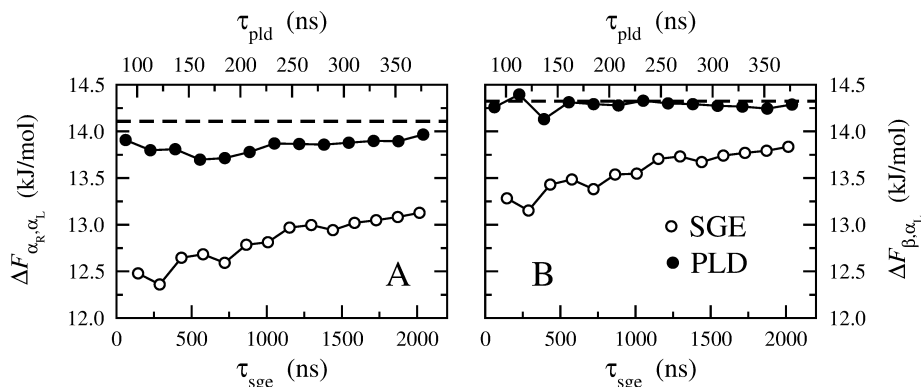


**Figure 7.8:** *Panel A:* Free energy difference  $\Delta F_{\alpha_R, \alpha_L}$  as a function of the simulation time estimated from both PLD and SGE simulations (full and open circles, respectively).  $\tau_{\text{sge}}$ , reported in the bottom axis, indicates the total SGE simulation time obtained by summing all replica times.  $\tau_{\text{edlp}}$ , reported in the top axis, is the total PLD time including contributions from eq- $R_{\alpha_R}$ , eq- $R_{\alpha_L}$  and LP simulations. The dashed line marks the value obtained from the US simulation of ref.[133]. *Panel B:* Free energy difference  $\Delta F_{\beta, \alpha_L}$  as a function of the simulation time. Lines are guides for the eyes.

the deviations from the reference values are of the order of the chemical accuracy. A detailed view on the reason why the PLD scheme outperforms SGE method for the system under study can be gained from the analysis of the single terms of eq. 7.6 (PLD) and eq. 7.14 (SGE) contributing to  $\Delta F_{\beta, \alpha_L}$  and  $\Delta F_{\alpha_R, \alpha_L}$ . To simplify the discussion, we will use the following notation:  $f_A = -\beta^{-1} \ln(\int_{D_A} e^{\beta[\Phi(\mathbf{z}_a) - \Phi(\mathbf{z})]} d\mathbf{z})$  and  $F_A = -\beta^{-1} \ln(\int_{D_A} e^{-\beta\Phi(\mathbf{z})} d\mathbf{z})$ , with  $A \equiv \alpha_R, \alpha_L, \beta$ . With these definitions, eq. 7.6 becomes  $\Delta F_{AB} = \Delta\Phi_{AB} + f_B - f_A$  and eq. 7.14  $\Delta F_{AB} = F_B - F_A$ . The contributions  $f_\beta$ ,  $f_{\alpha_R}$  and  $f_{\alpha_L}$  to PLD free energy differences and  $F_\beta$ ,  $F_{\alpha_R}$  and  $F_{\alpha_L}$  to SGE free energy differences are reported in fig. 7.9. All  $f_x$  quantities have a modest dependence on time, their spread ranging around 0.1-0.2  $\text{kJ mol}^{-1}$ . The SGE outcomes show a different pattern. In fact, while the spreads of  $F_\beta$  and  $F_{\alpha_R}$  are comparable to those obtained with the PLD scheme,  $F_{\alpha_L}$  exhibits an evident increasing trend from  $\sim 8.3$  to  $\sim 9$   $\text{kJ mol}^{-1}$ , which is at the origin of poor convergence of

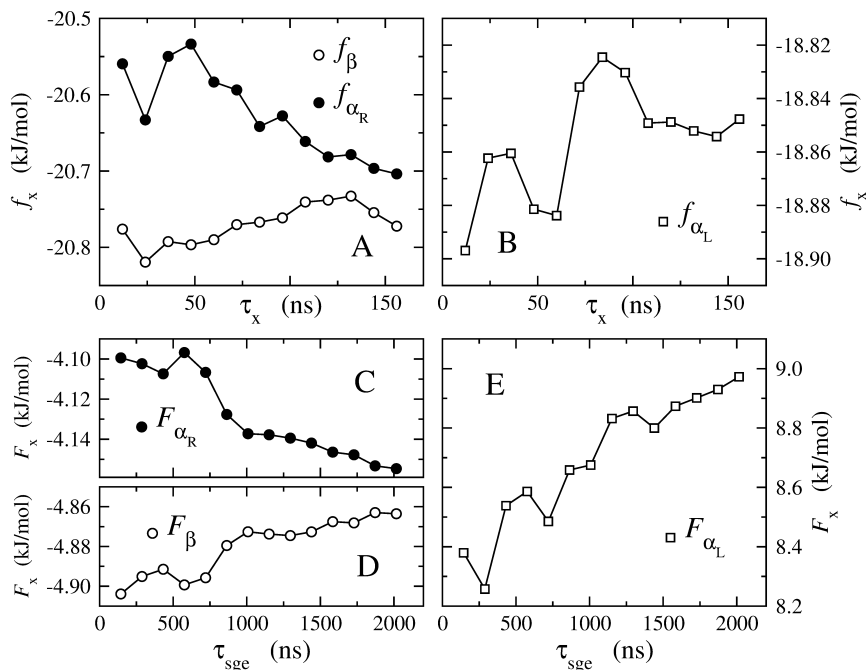


**Figure 7.9:** *Panels A and B:* Free energy contributions  $f_\beta$ ,  $f_{\alpha_R}$  and  $f_{\alpha_L}$  (see legend) to  $\Delta F_{\alpha_R, \alpha_L}$  and  $\Delta F_{\beta, \alpha_L}$ , computed via PLD scheme (see eq. 7.6), as functions of the eq- $R_x$  simulation time  $\tau_x$ . *Panels C, D and E:* Free energy contributions  $F_\beta$ ,  $F_{\alpha_R}$  and  $F_{\alpha_L}$  (see legend) to  $\Delta F_{\alpha_R, \alpha_L}$  and  $\Delta F_{\beta, \alpha_L}$ , computed via SGE scheme (see eq. 7.14), as functions of the SGE simulation time  $\tau_{\text{sge}}$ . Lines are guides for the eyes.

$\Delta F_{\beta, \alpha_L}$  and  $\Delta F_{\alpha_R, \alpha_L}$  in fig. 7.8. To understand the reason of the low accuracy in evaluating  $F_{\alpha_L}$  by using SGE schemes, we compare in fig. 7.10 estimates of  $\Phi(\mathbf{z})$ , limited to  $D_\beta$ ,  $D_{\alpha_R}$  and  $D_{\alpha_L}$  domains, obtained through PLD and SGE methods. PMFs in fig. 7.10A have been determined from eq- $R_x$  simulations lasting 156 ns, while the PMF in fig. 7.10B is obtained by the SGE simulation of 2016 ns. A simple visual inspection of fig. 7.10 allows us to notice the noisy sampling of the  $D_{\alpha_L}$  domain obtained with the SGE simulation in comparison

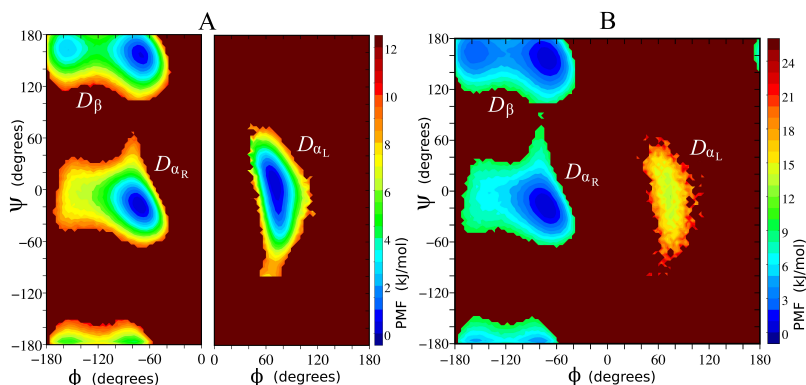


**Figure 7.10:** *Panel A:*  $\Phi(\mathbf{z})$  obtained via PLD scheme with eq- $R_x$  simulations lasting 156 ns. The plot, limited to  $D_\beta$ ,  $D_{\alpha_R}$  and  $D_{\alpha_L}$  conformational domains, is taken from fig. 7.6. Different panels are used for data from eq- $R_{\beta/\alpha_R}$  and eq- $R_{\alpha_L}$  simulations because PMFs are shifted up to an arbitrary constant. *Panel B:*  $\Phi(\mathbf{z})$  obtained from the SGE simulation lasting 2016 ns. The same angular resolution has been used in all plots ( $\Delta\phi = \Delta\psi = 3.6^\circ$ ).

to the eq- $R_{\alpha_L}$  simulation. Consistently with the data of fig. 7.9, which show comparable deviations with time of  $f_{\beta/\alpha_R}$  and  $F_{\beta/\alpha_R}$ , less remarkable sampling differences between PLD and SGE are observed in fig. 7.10 for the domains  $D_{\alpha_R}$  and  $D_\beta$ . These results point to identify the cause of SGE inaccuracy in the low statistical weights of microstates featuring the  $D_{\alpha_L}$  domain, ultimately due to the large free energy difference between the  $D_{\alpha_L}$  free energy basin and the  $D_{\alpha_R}$  and  $D_\beta$  basins ( $\sim 15 \text{ kJ mol}^{-1}$ ; see fig. 7.10B). In fact, owing to this free energy difference, the  $D_{\alpha_L}$  basin can be populated significantly during a SGE simulation only when replicas visit ensembles with downscaled intramolecular potential energy, whose microstates are featured by low weight factors. Borrowing the terminology from simulated tempering[129, 132] or temperature replica exchange[94, 104] methods, these downscaled energy ensembles correspond somehow to high temperature thermodynamic states. A detailed analysis of the statistical error in reweighting-based simulations was reported by Shen and Hamelberg in ref.[173].

## 7.5 Conclusive remarks

A simulation protocol, called Path-Linked Domains (PLD) scheme, is proposed to estimate free energy differences between configurational states, defined in terms of the hypersurface of (arbitrary) collective coordinates chosen to describe the molecular system. The basic purpose of the PLD simulation scheme is to tackle the difficulty of conventional equilibrium molecular dynamics and Monte Carlo simulations in exploring free energy hypersurfaces featured by manifold barriers and minima, and to limit sampling to defined subsets in the space of the collective coordinates chosen to describe the configurational states of interest (in our calculations, the  $\phi$  and  $\psi$  dihedral angles of the alanine dipeptide). To this aim, a first strategy was proposed in chapter 5, where we described the CDTS scheme, an extension of Steered Molecular Dynamics[151]. By definition of proper transition kernels, nonequilibrium paths connect two states with arbitrary shape and size, designing a series of intermediate domains in the space of the collective coordinates and giving access to their free energy difference. According to PLD algorithm, the restrained sampling is instead realized by means of two independent simulations, that allow to compute local configuration integrals associated with the two states. These integrals correspond to a sort of vibrational contributions to the free energy. It is possible to “make a link” in the space of collective coordinates, determining the difference of potential of mean force between a single couple of arbitrary points within the domains featuring the configurational states. The linking path in the space of collective coordinates can be chosen arbitrarily and computed with any method available in the literature, starting from adaptive biasing potential/force methods[41], to nonequilibrium techniques, such as those employed in this study. PLD technique, in addition to sets of linking-domains trajectories like CDTS, requires to perform equilibrium simulations, to determine the probability density at the chosen points of initial and final states. On the other hand, CDTS sampling of the initial microstates has to account for the variability of the controlled degree of freedom, enhancing the phase space to be sampled, and hence the error with respect to the linking path phase of PLD protocol. Although the PLD methodology is illustrated by the analysis of conformational states of a small peptide, nothing prevents from applying it in wider contexts, including chemical and biochemical problems involving complexation processes and drug-receptor interactions[53, 120, 126]. In the next chapter 8, both PLD and CDTS protocols will be adapted and compared in the

framework of ligand-receptor equilibria. As discussed in the next chapter, the extra computational effort required by PLD may lead in this context to a relevant enhancement of accuracy. A drawback that we envisage in both PLD and CDTS schemes, with respect to methods based on full sampling of the free energy hypersurface, is the prior knowledge of the two target configurational states. When it can be difficult to gain such a knowledge from simple intuition, one may however resort to short equilibrium simulations or to some accelerated sampling technique[69] to roughly probe the free energy landscape in the space of collective coordinates.

---

## Binding free energies of host-guest systems by nonequilibrium alchemical simulations with constrained dynamics

---

### 8.1 Introduction

The fundamental role of standard absolute binding free energy (ABFE) of ligand-receptor complexes in chemistry, biology and, especially, in drug discovery has stimulated an intensive research to design efficient computational strategies for fast and accurate free energy estimates[41, 42, 53, 118, 155, 197] and for reliable ligand screening[122, 178]. In the framework of molecular dynamics (MD) simulations, several approaches exploiting biasing potentials or restrained dynamics have been devised[25, 44, 58, 66, 121, 144, 156, 172, 181, 195, 203, 205]. An important class of methodologies revolves around alchemical transformations[28, 46, 53, 75, 80, 89, 93, 113, 114, 141, 153, 158, 176, 200], whose efficacy relies on the possibility of splitting the ABFE calculation of a ligand-receptor complex in two parts, one based on decoupling[80] or annihilation[111, 113] of the ligand from the solvent in a simulation of the solvated ligand and the other on the decoupling of the ligand

from its environment in a simulation of the solvated ligand-receptor complex. Alchemical transformations can in turn be performed by using equilibrium[20, 52, 80, 111, 113] and nonequilibrium[28, 46, 141, 157] MD simulations. In equilibrium simulations, the intermolecular potential energy between ligand and environment changes reversibly through a series of independent simulations, called replicas, characterized by ligand-environment potential energies different to each other. These potential energies are associated to specific values of a parameter  $\lambda$ , where the extremes correspond to the fully coupled and uncoupled states of the ligand. The free energy difference between coupled and uncoupled state is determined through thermodynamic integration[116], free energy perturbation[211] or Bennett acceptance ratio[18, 174]. In fast-switching alchemical transformations[164], the free energies relative to decoupling processes are computed according to prescriptions of nonequilibrium work theorems[106] applied to MD simulations[41]. Initial microstates are sampled at equilibrium fixing  $\lambda = 0$  (coupled state). Starting from each microstate, a set of nonequilibrium alchemical trajectories is realized by varying  $\lambda$  from 0 to 1 with a fixed time schedule. During such trajectories, the work performed on the system is computed and the set of work values is employed into Nonequilibrium Work Theorems (NWTs) [157] to find the free energy difference between final ( $\lambda = 1$ ) and initial state ( $\lambda = 0$ ). In this article, we supplement the fast-switching decoupling method[153, 164] with the possibility of performing alchemical trajectories during which the ligand is constrained to a fixed position relative to the receptor. Two types of approach are presented. The first, called binded-domain alchemical-path (BiD-AP) scheme, is based on a MD simulation protocol that allows to estimate free energy differences between coupled and uncoupled states of the ligand-receptor complex by means of nonequilibrium MD simulations, exploiting the extension of NWTs described in chapter 5. With respect to the fast-switching decoupling method without constraints[153, 164], the present approach prevents the ligand from leaving the binding site, but still requires an estimate of the binding-site volume. The second alchemical method, called single-point alchemical-path (SiP-AP) scheme, resembles the Path-Linked Domains (PLD) scheme developed in the previous chapter 7 in the context of conformational equilibria: a reference configuration of the ligand-receptor complex is introduced to split the ligand to receptor/solvent decoupling contribution to the ABFE into two separate energetic terms, one computed from an equilibrium MD simulation of the fully-coupled bound state of the complex and the other from fast-switching alchemical simulations of the complex



constrained in the reference configuration. The SiP-AP scheme allows to avoid the calculation of the positional binding-site volume, which is related to the change in free energy when the constrained gas-phase ligand is allowed to expand to occupy the standard volume,  $V^\circ = 1661 \text{ \AA}^3$ . These rotational and positional contributions to the ABFE do not simply “disappear” from the calculation, but are accounted for in implicit way, through a potential of mean force as a function of the ligand position (rotational contribution) and through the integration domain of an integral entering the probability density as a function of the ligand position (positional contribution). The proposed methodologies are numerically tested here on ABFE estimates of the Zn(II)·N-hydroxypropanamide complex, and applied to the study of two complexes of  $\beta$ -cyclodextrin ( $\beta$ -CD) with aromatic compounds, specifically benzene and naphthalene. All calculations refer to ligand-receptor systems into water solution, simulated using explicit-atom models. This study is also intended to provide an illustration of technical and theoretical aspects of the methodology, concerning, for example, the paradigm for the definition of binding, which can be based either on the vector position of the ligand relative to a receptor-frame (Zn(II)·anion case) or on the magnitude of the distance between specific points of ligand and receptor ( $\beta$ -CD·benz and  $\beta$ -CD·naph cases). The differences between BiD-AP and SiP-AP schemes, adapting respectively Configurational Domains Transition Scheme CDTS (chapter 5) and PLD (chapter 7) schemes to the context of alchemical reactions, are also outlined and discussed in terms of computational efficiency.

## 8.2 Thermodynamics of the noncovalent binding

BiD-AP and SiP-AP schemes are developed starting from the theory of noncovalent binding association by Gilson and coworkers[80]. In this section, we review the basic relationships for the calculation of the standard ABFE through alchemical transformations, preserving the notation of ref.[80] whenever possible. The reaction we are interested to is the association of a ligand L with a receptor R to form a noncovalent complex RL in solution,



At equilibrium, the chemical potentials of L, R, and RL into solution are equalized, namely

$$\mu_{\text{sol,R}} + \mu_{\text{sol,L}} = \mu_{\text{sol,RL}}. \quad (8.2)$$

The chemical potential of a species  $i$  at a given concentration  $C_i$  can be expressed as

$$\mu_{\text{sol},i} = \mu_{\text{sol},i}^{\circ} + RT \ln \frac{\gamma_i C_i}{C^{\circ}}, \quad (8.3)$$

where  $\mu_{\text{sol},i}^{\circ}$  is the standard chemical potential,  $\gamma_i$  is the activity coefficient,  $C^{\circ}$  is the standard concentration in the same units as  $C_i$  (1 M or 1 molecule/1661 Å<sup>3</sup>),  $R$  is the gas constant and  $T$  is the absolute temperature. As Gilson and coworkers noted,  $\mu_{\text{sol},i}^{\circ}$  is the chemical potential in a hypothetical standard state in which each species is at standard concentration in the solvent, but does not interact with other solute molecules. It is worth noting that, in the infinite dilution limit, the activity coefficients of the solute species approach unity[87, 124]. Recasting eqs. 8.2 and 8.3, the relation between the standard free energy of binding and the binding constant  $K$  is obtained

$$\Delta G^{\circ} \equiv \mu_{\text{sol,RL}}^{\circ} - \mu_{\text{sol,R}}^{\circ} - \mu_{\text{sol,L}}^{\circ} = -RT \ln \left( \frac{\gamma_{\text{RL}}}{\gamma_{\text{R}}\gamma_{\text{L}}} \frac{C^{\circ} C_{\text{RL}}}{C_{\text{R}} C_{\text{L}}} \right) \equiv -RT \ln K. \quad (8.4)$$

A relationship to link the ABFE ( $\Delta G^{\circ}$ ), and hence  $K$ , to statistical thermodynamic quantities has been derived by Hill in ref.[98] and revised by Gilson and coworkers[80] to include explicitly the standard concentration,

$$\mu_{\text{sol,R}}^{\circ} = -RT \ln \left( \frac{1}{V_{N,\text{R}} C^{\circ}} \frac{Q_{N,\text{R}}(V_{N,\text{R}})}{Q_{N,0}(V_{N,0})} \right) + P^{\circ} \bar{V}_{\text{R}}, \quad (8.5)$$

with analogous expressions for the ligand L and the complex RL. In the previous equation,  $Q_{N,\text{R}}(V_{N,\text{R}})$  is the canonical partition function for a solution consisting of  $N$  solvent molecules and one molecule R at volume  $V_{N,\text{R}}$ , which is the volume of this solution when it is at equilibrium at the temperature  $T$  and standard pressure  $P^{\circ}$ . Analogously,  $Q_{N,0}(V_{N,0})$  is the canonical partition function of  $N$  solvent molecules alone at the volume  $V_{N,0}$ , namely the equilibrium volume of the pure-solvent sample at  $T$  and  $P^{\circ}$  conditions. Finally, for large values of  $N$ ,  $\bar{V}_{\text{R}}/N_A = V_{N,\text{R}} - V_{N,0}$  is the volume change occurring when one molecule R is added to  $N$  molecules of solvent ( $N_A$  being the Avogadro's number). It is worth noting that the term  $P^{\circ} \bar{V}_{\text{R}}$  into eq. 8.5 is typically very small[17], because of small values of  $\bar{V}_{\text{R}}$ . We now report on a more detailed expression of the standard chemical potentials  $\mu_{\text{sol,R}}^{\circ}$  and  $\mu_{\text{sol,L}}^{\circ}$ , by exploiting the representation of the canonical partition functions in terms of the classical statistical thermodynamics[24, 136]. In this framework, the partition function

$Q_{N,R}(V_{N,R})$  can be written as a phase-space integral separable as the product of an integral over the positional variables, *i.e.* the atomic coordinates, and two integrals over the dynamical variables, *i.e.* the conjugate momenta related to the solute and solvent atoms:

$$Q_{N,R}(V_{N,R}) = \frac{1}{\sigma_{\text{sol},R} \sigma_{\text{S}}^N} \int e^{-\beta U(\mathbf{r}'_{\text{R}}, \mathbf{r}_{\text{S}})} d\mathbf{r}'_{\text{R}} d\mathbf{r}_{\text{S}} \\ \times \int \exp\left(-\beta \sum_{i=1}^{M_{\text{R}}} \frac{p_i^2}{2m_{\text{R},i}}\right) d\mathbf{p}_{\text{R}} \int \exp\left(-\beta \sum_{i=1}^{N_{\text{S}}N} \frac{p_i^2}{2m_{\text{S},i}}\right) d\mathbf{p}_{\text{S}}, \quad (8.6)$$

where  $\beta$  is the inverse temperature,  $p_i^2$  is the squared magnitude of the momentum of the generic atom  $i$ ,  $M_{\text{R}}$  is the number of atoms of R,  $\mathbf{r}'_{\text{R}}$  and  $\mathbf{p}_{\text{R}}$  denote the atomic coordinates and conjugate momenta of R, respectively, while  $\mathbf{r}_{\text{S}}$  and  $\mathbf{p}_{\text{S}}$  are the analogous variables for the  $N_{\text{S}}N$  solvent atoms (here,  $N_{\text{S}}$  is the number of atoms for one solvent molecule). Also,  $m_{\text{R},i}$  and  $m_{\text{S},i}$  indicate the mass of atom  $i$  belonging to receptor and solvent, respectively. We note that, at variance with the integral over the conjugate momenta, the integral over  $\mathbf{r}'_{\text{R}}$  and  $\mathbf{r}_{\text{S}}$  cannot be split, because the coordinates of solute and solvent are inextricably connected through mixed terms into  $U(\mathbf{r}'_{\text{R}}, \mathbf{r}_{\text{S}})$ . In eq. 8.6,  $\sigma_{\text{sol},R}$  and  $\sigma_{\text{S}}$  are the symmetry numbers of R into solution and of a solvent molecule into a pure solvent sample. Specifying that the symmetry number of R is related to the solution environment is mandatory, because similar factors will be introduced for the gas phase and the complex RL. It is worth considering that the factor arising from the quantum-mechanical correction is not included in the expression of  $Q_{N,R}(V_{N,R})$ , because it cancels out with other analogous contributions to the ABFE. We now introduce a molecular axis system to separate the lab-frame coordinates  $\mathbf{r}'_{\text{R}}$  into internal and external. This molecular axis system is built taking as reference three atoms of R. Atom 1 becomes the origin of the molecular coordinates, denoted as  $\mathbf{R}_{\text{R}}$ . The vector joining atom 1 with atom 2 defines the  $x$ -axis. The direction of the  $y$ -axis is given by the direction of the vector joining atoms 2 and 3, minus the  $x$ -component of this vector. The  $z$ -axis is constructed as the cross-product of the unit vectors along the  $x$  and  $y$ -axes. The six coordinates thus fixed, namely  $\mathbf{R}_{\text{R}}$  plus the Eulerian angles  $\xi_{\text{R},1}$ ,  $\xi_{\text{R},2}$  and  $\xi_{\text{R},3}$  that specify the orientation of the molecular frame relative to the lab-frame, correspond to the external coordinates of R. The set of  $3M_{\text{R}} - 6$  internal coordinates of R will be indicated with  $\mathbf{r}_{\text{R}}$ . Noting that the integrals over  $\mathbf{r}_{\text{R}}$  and  $\mathbf{r}_{\text{S}}$  do not depend upon the position and orientation of R, the integrals over  $\mathbf{R}_{\text{R}}$ ,  $\xi_{\text{R},1}$ ,  $\xi_{\text{R},2}$  and  $\xi_{\text{R},3}$  can be done at once. Considering that R is typically a polyatomic nonlinear molecule, the integrals yield  $8\pi^2 V_{N,R}$ . Moreover,

considering that the integral over the momenta components of an atom of mass  $m$  yields a factor  $(2\pi mRT)^{3/2}$ , the partition function of eq. 8.6 can be written as

$$Q_{N,R}(V_{N,R}) = \frac{8\pi^2 V_{N,R} Z_{N,R}}{\sigma_{\text{sol},R}^N \sigma_S^N} \prod_{i=1}^{M_R} (2\pi m_{R,i} RT)^{3/2} \prod_{i=1}^{N_S N} (2\pi m_{S,i} RT)^{3/2}, \quad (8.7)$$

where

$$Z_{N,R} = \int e^{-\beta U(\mathbf{r}_R, \mathbf{r}_S)} d\mathbf{r}_R d\mathbf{r}_S \quad (8.8)$$

is the configuration integral for a system consisting of one R molecule into  $N$  solvent molecules. In a similar way, we may express the partition function of  $N$  solvent molecules as

$$\begin{aligned} Q_{N,0}(V_{N,0}) &= \frac{1}{\sigma_S^N} \int e^{-\beta U(\mathbf{r}_S)} d\mathbf{r}_S \int \exp\left(-\beta \sum_{i=1}^{N_S N} \frac{p_i^2}{2m_{S,i}}\right) d\mathbf{p}_S \\ &= \frac{Z_{N,0}}{\sigma_S^N} \prod_{i=1}^{N_S N} (2\pi m_{S,i} RT)^{3/2}, \end{aligned} \quad (8.9)$$

where  $Z_{N,0}$  is the configuration integral for the solvent sample

$$Z_{N,0} = \int e^{-\beta U(\mathbf{r}_S)} d\mathbf{r}_S. \quad (8.10)$$

Upon substitution of eqs. 8.7 and 8.9 into eq. 8.5, we obtain

$$\mu_{\text{sol},R}^\circ = -RT \ln \left( \frac{8\pi^2}{C^\circ \sigma_{\text{sol},R}} \prod_{i=1}^{M_R} (2\pi m_{R,i} RT)^{\frac{3}{2}} \frac{Z_{N,R}}{Z_{N,0}} \right) + P^\circ \bar{V}_R. \quad (8.11)$$

Similar arguments lead to a relationship for  $\mu_{\text{sol},L}^\circ$ . However considering that the ligand can be also linear in shape and even a single atom, integration over the orientational degrees of freedom can give  $8\pi^2$ ,  $4\pi$  and 1, respectively (from now on, this geometry factor will be denoted as  $\mathcal{V}_{\xi_L}$ ). Therefore, the expression for  $\mu_{\text{sol},L}^\circ$  is

$$\mu_{\text{sol},L}^\circ = -RT \ln \left( \frac{\mathcal{V}_{\xi_L}}{C^\circ \sigma_{\text{sol},L}} \prod_{i=1}^{M_L} (2\pi m_{L,i} RT)^{\frac{3}{2}} \frac{Z_{N,L}}{Z_{N,0}} \right) + P^\circ \bar{V}_L, \quad (8.12)$$

where, the product is extended to the  $M_L$  atoms of the ligand and  $m_{L,i}$  is the mass of atom  $i$  of the ligand. The calculation of the standard chemical potential of the complex  $\mu_{\text{sol},RL}^\circ$

requires a specific treatment of the external and internal coordinates of RL. The former are assumed to be the external coordinates of R, while the external coordinates of L, indicated as  $\zeta_L \equiv (\mathbf{R}_L, \xi_{L,1}, \xi_{L,2}, \xi_{L,3})$ , are taken to be defined relative to R, so that they become internal coordinates of the complex. The arguments adopted to determine  $\mu_{\text{sol,R}}^\circ$  and  $\mu_{\text{sol,L}}^\circ$  may also be used here with the difference that the configuration integral of the complex must be restricted to the configurations for which R and L are complexed[24]. This can be realized introducing a step function  $I(\zeta_L)$  that holds 1 for bound configurations and 0 otherwise. We then obtain the following expression,

$$\begin{aligned} \mu_{\text{sol,RL}}^\circ &= -RT \ln \left( \frac{8\pi^2}{C^\circ \sigma_{\text{cp,L}} \sigma_{\text{cp,R}}} \frac{Z_{N,\text{RL}}}{Z_{N,0}} \right) \\ &\quad - RT \ln \left( \prod_{i=1}^{M_L} (2\pi m_{L,i} RT)^{\frac{3}{2}} \prod_{i=1}^{M_R} (2\pi m_{R,i} RT)^{\frac{3}{2}} \right) + P^\circ \bar{V}_{\text{RL}}. \end{aligned} \quad (8.13)$$

In the previous equation,  $Z_{N,\text{RL}}$  is the configuration integral of RL into solution

$$Z_{N,\text{RL}} = \int I(\zeta_L) J_{\zeta_L} e^{-\beta U(\zeta_L, \mathbf{r}_L, \mathbf{r}_R, \mathbf{r}_S)} d\zeta_L d\mathbf{r}_L d\mathbf{r}_R d\mathbf{r}_S, \quad (8.14)$$

where  $J_{\zeta_L}$  is the absolute value of the Jacobian determinant for the rotation and translation of L relative to R. In eq. 8.13,  $\sigma_{\text{cp,L}}$  and  $\sigma_{\text{cp,R}}$  are the symmetry numbers associated with L and R when the complex is in place. Recasting eqs. 8.11, 8.12 and 8.13 into eq. 8.4, the expression for the standard ABFE is recovered

$$\Delta G^\circ = -RT \ln \left( \frac{C^\circ}{V_{\xi_L}} \frac{\sigma_{\text{sol,L}} \sigma_{\text{sol,R}}}{\sigma_{\text{cp,L}} \sigma_{\text{cp,R}}} \frac{Z_{N,\text{RL}} Z_{N,0}}{Z_{N,\text{R}} Z_{N,\text{L}}} \right) + P^\circ (\bar{V}_{\text{RL}} - \bar{V}_{\text{R}} - \bar{V}_{\text{L}}). \quad (8.15)$$

### 8.3 The double-decoupling method

The double-decoupling method is a route to the estimate of  $\Delta G^\circ$  and is based on the calculation of the free energy differences associated with two independent processes entering the thermodynamic cycle represented in fig. 8.1. One process, related to the free energy change  $\Delta G_1^\circ$ , is the decoupling of L from the solvated RL complex (right process in fig. 8.1). The other process, related to the free energy change  $\Delta G_2^\circ$ , is the decoupling of L from the solvent (left process in fig. 8.1). While the former process is physically meaningless, the latter corresponds to the desolvation free energy of L. In the former case, decoupling is

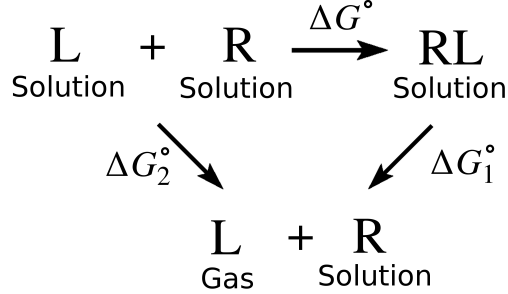


**Figure 8.1:** Thermodynamic cycle describing the double-decoupling method.

accomplished by turning off the interactions of L with solvent and receptor R in a solution of RL, while in the latter case decoupling is realized by turning off the interactions of L with the solvent in a solution of L. It is important to remark that, in both situations, we do not deal with a total annihilation of L, because its intramolecular interactions are left in place, and hence L is virtually “transformed” in a ideal-gas molecule. Before discussing the decoupling processes and in particular the details of our approach, it is mandatory to relate  $\Delta G^\circ$  to the quantities  $\Delta G_1^\circ$  and  $\Delta G_2^\circ$ . According to Gilson and coworkers[80],  $\Delta G_1^\circ$  and  $\Delta G_2^\circ$  can be written as

$$\Delta G_1^\circ = \mu_{\text{sol,R}}^\circ + \mu_{\text{gas,L}}^\circ - \mu_{\text{sol,RL}}^\circ, \quad (8.16)$$

$$\Delta G_2^\circ = \mu_{\text{gas,L}}^\circ - \mu_{\text{sol,L}}^\circ, \quad (8.17)$$

where  $\mu_{\text{gas,L}}^\circ$  is the standard chemical potential of L in the ideal-gas phase and the other standard chemical potentials are defined in eqs. 8.11, 8.12 and 8.13. Considering eq. 8.4 together with eqs. 8.16 and 8.17, it is immediate to show that

$$\Delta G^\circ = \Delta G_2^\circ - \Delta G_1^\circ. \quad (8.18)$$

Such a relation is also inferred straightforwardly by the thermodynamic cycle reported in fig. 8.1. In the next sections, we will show how  $\Delta G_1^\circ$  and  $\Delta G_2^\circ$  can be expressed in terms of configuration integrals, ultimately allowing for a description through potentials of mean force.

### 8.3.1 Decoupling the ligand from solvent and receptor: $\Delta G_1^\circ$ calculation

The standard chemical potential of L in the ideal-gas phase,  $\mu_{\text{gas,L}}^\circ$ , is related to the natural logarithm of the molecular partition function as

$$\mu_{\text{gas,L}}^\circ = -RT \ln Q_{0,\text{L}}(V^\circ), \quad (8.19)$$

where it is explicitly reported that the partition function must be evaluated in the phase space limited to the standard volume  $V^\circ = 1/C^\circ$ . Following the arguments leading to eq. 8.12, we get

$$\mu_{\text{gas,L}}^\circ = -RT \ln \left( \frac{\mathcal{V}_{\xi_{\text{L}}}}{C^\circ} \frac{Z_{0,\text{L}}}{\sigma_{\text{gas,L}}} \prod_{i=1}^{M_{\text{L}}} (2\pi m_{\text{L},i} RT)^{\frac{3}{2}} \right). \quad (8.20)$$

In the previous equation,  $\mathcal{V}_{\xi_{\text{L}}}$  is from the integral over the orientation of L ( $\mathcal{V}_{\xi_{\text{L}}} = 8\pi^2, 4\pi, 1$  for non linear, linear and single-atom ligands, respectively),  $\sigma_{\text{gas,L}}$  is the symmetry number of L in the ideal-gas phase and  $Z_{0,\text{L}}$  is the configuration integral in the internal coordinates:

$$Z_{0,\text{L}} = \int e^{-\beta U(\mathbf{r}_{\text{L}})} d\mathbf{r}_{\text{L}}. \quad (8.21)$$

The external coordinates of L are integrated in eq. 8.20, giving the contribution  $\mathcal{V}_{\xi_{\text{L}}}/(C^\circ \sigma_{\text{gas,L}})$ . Substituting eqs. 8.11, 8.13 and 8.20 into eq. 8.16, we obtain

$$\Delta G_1^\circ = -RT \ln \left( \frac{\mathcal{V}_{\xi_{\text{L}}}}{C^\circ} \frac{\sigma_{\text{cp,L}} \sigma_{\text{cp,R}}}{\sigma_{\text{gas,L}} \sigma_{\text{sol,R}}} \frac{Z_{\text{N,R}} Z_{0,\text{L}}}{Z_{\text{N,RL}}} \right) + P^\circ (\bar{V}_{\text{R}} - \bar{V}_{\text{RL}}). \quad (8.22)$$

In the double-decoupling method, an artificial energy function  $U(\lambda, \zeta_{\text{L}}, \mathbf{r}_{\text{L}}, \mathbf{r}_{\text{R}}, \mathbf{r}_{\text{S}})$  dependent on a control parameter  $\lambda \in [0, 1]$  is introduced, whose functional form is rather arbitrary. The only requirements are that for  $\lambda = 0$  and  $\lambda = 1$  the function must correspond to the energy functions of the coupled and uncoupled states of the ligand in the complex, respectively:

$$U(0, \zeta_{\text{L}}, \mathbf{r}_{\text{L}}, \mathbf{r}_{\text{R}}, \mathbf{r}_{\text{S}}) = U(\zeta_{\text{L}}, \mathbf{r}_{\text{L}}, \mathbf{r}_{\text{R}}, \mathbf{r}_{\text{S}}), \quad (8.23)$$

$$U(1, \zeta_{\text{L}}, \mathbf{r}_{\text{L}}, \mathbf{r}_{\text{R}}, \mathbf{r}_{\text{S}}) = U(\mathbf{r}_{\text{R}}, \mathbf{r}_{\text{S}}) + U(\mathbf{r}_{\text{L}}). \quad (8.24)$$

Exploiting the artificial energy function, a free energy function dependent parametrically on  $\lambda$  can be built as

$$g(\lambda) = -RT \ln \left( \int I(\zeta_{\text{L}}) J_{\zeta_{\text{L}}} e^{-\beta U(\lambda, \zeta_{\text{L}}, \mathbf{r}_{\text{L}}, \mathbf{r}_{\text{R}}, \mathbf{r}_{\text{S}})} d\zeta_{\text{L}} d\mathbf{r}_{\text{L}} d\mathbf{r}_{\text{R}} d\mathbf{r}_{\text{S}} \right). \quad (8.25)$$

According to  $g(\lambda)$  and to the requirements of eqs. 8.23 and 8.24, the free energy difference between the final and initial states is

$$\begin{aligned} g(1) - g(0) &= -RT \ln \left( \frac{\int I(\zeta_L) J_{\zeta_L} e^{-\beta U(\mathbf{r}_R, \mathbf{r}_S)} e^{-\beta U(\mathbf{r}_L)} d\zeta_L d\mathbf{r}_L d\mathbf{r}_R d\mathbf{r}_S}{\int I(\zeta_L) J_{\zeta_L} e^{-\beta U(\zeta_L, \mathbf{r}_L, \mathbf{r}_R, \mathbf{r}_S)} d\zeta_L d\mathbf{r}_L d\mathbf{r}_R d\mathbf{r}_S} \right) \\ &= -RT \ln \left( \frac{V_{\zeta_L} Z_{N,R} Z_{0,L}}{Z_{N,RL}} \right), \end{aligned} \quad (8.26)$$

where the definitions of the configuration integrals, eqs. 8.8, 8.14 and 8.21, have been used in deriving the second line of eq. 8.26, after integrating the numerator over  $\zeta_L$ . This operation is allowed for being the exponential functions in the numerator independent of  $\zeta_L$ . Such an integration gives the binding-site volume  $\int I(\zeta_L) J_{\zeta_L} d\zeta_L = V_{\zeta_L}$ , a quantity to be estimated numerically. Substituting eq. 8.26 into eq. 8.22, leads to

$$\Delta G_1^\circ = g(1) - g(0) - RT \ln \left( \frac{\mathcal{V}_{\xi_L}}{C^\circ V_{\zeta_L}} \frac{\sigma_{cp,L} \sigma_{cp,R}}{\sigma_{gas,L} \sigma_{sol,R}} \right) + P^\circ (\bar{V}_R - \bar{V}_{RL}). \quad (8.27)$$

We have considered the possibility of dealing with linear molecules or single atoms as ligands. This is disclosed by the introduction of the parameter  $\mathcal{V}_{\xi_L}$  instead of the factor  $8\pi^2$  of ref. [80], being the latter valid only for nonlinear ligands. The quantity  $g(1) - g(0)$  can be evaluated via equilibrium MD simulations exploiting the method of thermodynamic integration[80]. However, to gain an estimate of  $\Delta G_1^\circ$  one must also determine  $V_{\zeta_L}$ , which may not be a straightforward task. Also, it is worth noting that eq. 8.27 strictly holds for simulations performed in the canonical (NVT) ensemble, since only the artificial potential energy function appears in the exponential function of  $g(\lambda)$  (see eq. 8.25). When MD simulations are performed by adopting equations of motion which preserve NPT conditions, we are actually employing a free energy function supplemented with a  $P^\circ V$  term in the exponential function. The use of a NPT-like free energy function allows us to access directly to  $\Delta G_1^\circ$  without any correction for the partial molar volumes  $\bar{V}_R$  and  $\bar{V}_{RL}$ . In the following, in order to adhere to the Gilson and coworkers' treatment[80], we preserve the assumptions for the canonical ensemble, keeping in mind that the pressure-times-volume corrections must not be considered when simulating in the NPT conditions. In this study, we propose to modify the paradigm for the ligand-receptor binding, adopting a criterion based only on the position of L relative to R, previously denoted as  $\mathbf{R}_L$ . This corresponds to turn from a binding function expressed in terms of position and orientation of L, *i.e.*  $I(\zeta_L) \equiv I(\mathbf{R}_L, \xi_{L,1}, \xi_{L,2}, \xi_{L,3})$ , to a



binding function expressed in terms of the position of L alone, *i.e.*  $I(\mathbf{R}_L)$ . This assumption is consistent with the common idea that binding occurs basically when ligand and receptor come into contact, regardless the mutual orientation defined by the variables  $\xi_{L,1}$ ,  $\xi_{L,2}$  and  $\xi_{L,3}$ . Of course, for a generic position  $\mathbf{R}_L$  satisfying the binding condition  $I(\mathbf{R}_L) = 1$ , most orientations of L relative to R will have a negligible probability of being observed in the coupled state, because of strong atomic overlaps between R and L. As a consequence, these configurations will contribute negligibly to the denominator of eq. 8.26. This scheme allows us to rewrite the free energy function of eq. 8.25 as

$$g(\lambda) = -RT \ln \left( \int I(\mathbf{R}_L) J_{\mathbf{R}_L} J_{\xi_L} e^{-\beta U(\lambda, \mathbf{R}_L, \xi_L, \mathbf{r}_L, \mathbf{r}_R, \mathbf{r}_S)} d\mathbf{R}_L d\xi_L d\mathbf{r}_L d\mathbf{r}_R d\mathbf{r}_S \right), \quad (8.28)$$

where  $\xi_L$  is a shorthand for  $(\xi_{L,1}, \xi_{L,2}, \xi_{L,3})$ ,  $J_{\xi_L}$  and  $J_{\mathbf{R}_L}$  are the absolute values of the Jacobian determinants for the (external) rotational and translational coordinates of L, respectively, and  $d\xi_L \equiv d\xi_{L,1} d\xi_{L,2} d\xi_{L,3}$ . As noted below eq. 8.14, the Jacobian determinant  $J_{\mathbf{R}_L}$  is in general different from 1, being 1 only when  $\mathbf{R}_L$  is expressed in a Cartesian reference system. The free energy difference  $g(1) - g(0)$  of eq. 8.26 is then restated as,

$$\begin{aligned} g(1) - g(0) &= -RT \ln \left( \frac{\int I(\mathbf{R}_L) J_{\mathbf{R}_L} J_{\xi_L} e^{-\beta U(\mathbf{r}_R, \mathbf{r}_S)} e^{-\beta U(\mathbf{r}_L)} d\mathbf{R}_L d\xi_L d\mathbf{r}_L d\mathbf{r}_R d\mathbf{r}_S}{\int I(\mathbf{R}_L) J_{\mathbf{R}_L} J_{\xi_L} e^{-\beta U(\mathbf{R}_L, \xi_L, \mathbf{r}_L, \mathbf{r}_R, \mathbf{r}_S)} d\mathbf{R}_L d\xi_L d\mathbf{r}_L d\mathbf{r}_R d\mathbf{r}_S} \right) \\ &= -RT \ln \left( V_I \mathcal{V}_{\xi_L} \frac{Z_{N,R} Z_{0,L}}{Z_{N,RL}} \right). \end{aligned} \quad (8.29)$$

In the second line of eq. 8.29, we have carried out the integration over  $\mathbf{R}_L$  and  $\xi_L$  in the numerator, obtaining  $V_I = \int I(\mathbf{R}_L) J_{\mathbf{R}_L} d\mathbf{R}_L$  and  $\mathcal{V}_{\xi_L} = \int J_{\xi_L} d\xi_L$ , the latter being  $8\pi^2$ ,  $4\pi$  or 1, according to the structure of L. Contrarily to eq. 8.26, separation of these integrals can be done into eq. 8.29 because the adopted binding criterion does not involve the rotational coordinates  $\xi_L$ . Since the bound states of the complex are identified on the basis of  $\mathbf{R}_L$ , it is convenient to introduce a potential of mean force as a function of  $\lambda$ , which includes the internal coordinates of R and L, the coordinates of the solvent and the orientational coordinates of L. This potential results to be a function of both  $\lambda$  and  $\mathbf{R}_L$ :

$$e^{-\beta \phi(\lambda, \mathbf{R}_L)} = \int J_{\xi_L} e^{-\beta U(\lambda, \mathbf{R}_L, \xi_L, \mathbf{r}_L, \mathbf{r}_R, \mathbf{r}_S)} d\xi_L d\mathbf{r}_L d\mathbf{r}_R d\mathbf{r}_S. \quad (8.30)$$

According to the above definition of potential of mean force, the free energy function  $g(\lambda)$  (eq. 8.28) takes the following simplified form

$$g(\lambda) = -RT \ln \left( \int I(\mathbf{R}_L) J_{\mathbf{R}_L} e^{-\beta\phi(\lambda, \mathbf{R}_L)} d\mathbf{R}_L \right). \quad (8.31)$$

Using the definition 8.31 of  $g(\lambda)$  into eq. 8.29, we obtain

$$g(1) - g(0) = -RT \ln \left( \frac{\int I(\mathbf{R}_L) J_{\mathbf{R}_L} e^{-\beta\phi(1, \mathbf{R}_L)} d\mathbf{R}_L}{\int I(\mathbf{R}_L) J_{\mathbf{R}_L} e^{-\beta\phi(0, \mathbf{R}_L)} d\mathbf{R}_L} \right). \quad (8.32)$$

It is worthwhile to note that, in the previous equation,  $\phi(1, \mathbf{R}_L)$  does not depend on  $\mathbf{R}_L$ [8]. Nonetheless, in order to preserve consistency of notation, from now on the symbol  $\mathbf{R}_L$  will be explicitly indicated into  $\phi(\lambda, \mathbf{R}_L)$ , regardless of  $\lambda$ .

### BiD-AP scheme in nonequilibrium alchemical transformations

In the following two sections, we report on two alternative schemes to compute  $\Delta G_1^\circ$ . The first, termed BiD-AP (binded-domain alchemical-path) scheme, is based on the direct estimate of  $g(1) - g(0)$  (eq. 8.32). In this aspect the methodology is analogous to that of Gilson and coworkers[80]. In particular,  $g(1) - g(0)$  is computed from nonequilibrium MD simulations, instead of using thermodynamic integration via equilibrium MD simulations. In nonequilibrium alchemical transformations, according to the fact that the end states must be related to the complex RL (see eq. 8.32), the initial microstates have to represent bound RL configurations sampled at equilibrium[164]. Moreover, in order to attain a bound RL configuration in the final microstate, we must prevent the ligand from leaving the binding site during the sampling. When dealing with a strongly bound complex, the correct sampling weight of the initial microstates can be guaranteed implicitly by an equilibrium MD simulation, without enforcing any constraint to keep the binding in place. In such a case, a precise definition of bound-complex configurations is unimportant so long as binding is tight and all the statistically important bound configurations are sampled during the simulation[80]. For weak complexes, preserving bound configurations during a standard equilibrium MD simulation can instead be difficult. This requires that bound RL configurations are sampled by enforcing some hard-walled potential matching  $I(\mathbf{R}_L)$ . This equilibrium sampling provides an amount of isothermally and isobarically sampled microstates, say  $N_{\text{traj}}$ , to be taken

as initial phase-space points for the nonequilibrium alchemical trajectories. Equation 8.32 establishes that L must be in the same binding site in both the initial and final states. This can be accomplished by creating a bijective mapping between these states, with the aim of preventing the ligand from leaving the binding site. Generalization of Nonequilibrium Work Theorems [48, 50, 106, 108], operated in chapter 5, allows indeed the estimate of free energy differences between two configurational domains by means of steered MD simulations. A phase-space mapping is applied during the nonequilibrium trajectories, whether to the control parameter employed to switch the system from the initial to the final state or to some phase-space variable (not directly correlated to the control parameter) taken to define the two configurational domains. The latter is just the situation that we may apply to the alchemical transformations. Evolving in time the  $\lambda$  control parameter from 0 (coupled ligand) to 1 (uncoupled ligand) according to some established time schedule, the coordinate  $\mathbf{R}_L$  of the ligand relative to the receptor is mapped to bring the system from a coupled to an uncoupled configuration within the binding site. This is accomplished by fixing the  $\mathbf{R}_L$  coordinate to the initial value (obtained from the equilibrium sampling) during the alchemical transformation, thus preventing the ligand from leaving the binding site. A constraint to  $\mathbf{R}_L$  can be applied whether using some constraining method, such as RATTLE[13] or SHAKE[163], or more simply by enforcing stiff (harmonic) potentials to the three components of  $\mathbf{R}_L$ . Using this simulation scheme, we thus produce  $N_{\text{traj}}$  alchemical trajectories that allow to compute the free energy difference  $g(1) - g(0)$  by using the Jarzynski equality[106]:

$$g(1) - g(0) = -RT \ln \langle e^{-\beta W} \rangle, \quad (8.33)$$

where the average is performed over the  $N_{\text{traj}}$  work values  $W$  associated to the alchemical trajectories. For a generic trajectory, the work is computed with the standard formula[41]

$$W = \int_0^\tau \frac{\partial U(\lambda, \mathbf{R}_L, \xi_L, \mathbf{r}_L, \mathbf{r}_R, \mathbf{r}_S)}{\partial t} dt, \quad (8.34)$$

where  $\mathbf{R}_L$  is fixed to the value of the initial microstate and  $\tau$  is the duration time of the alchemical trajectory. We outline that the explicit dependence on time lies only on the  $\lambda$  parameter, while the other variables are uncontrolled degrees of freedom. Once the quantity  $g(1) - g(0)$  is estimated, the contribution  $\Delta G_1^o$  to the ABFE can be computed through the

following relationship (use the second line of eq. 8.29 into eq. 8.22)

$$\Delta G_1^\circ = g(1) - g(0) - RT \ln \left( \frac{1}{V_I C^\circ} \frac{\sigma_{\text{cp,L}} \sigma_{\text{cp,R}}}{\sigma_{\text{gas,L}} \sigma_{\text{sol,R}}} \right) + P^\circ (\bar{V}_R - \bar{V}_{\text{RL}}). \quad (8.35)$$

It is important to note that, as in the thermodynamic integration method, the calculation of the binding-site volume  $V_I$  needs to be carried out. A schematic illustration of the BiD-AP scheme is reported and shortly described in fig. 8.2.

### SiP-AP scheme in nonequilibrium alchemical transformations

In order to avoid the calculation of  $V_I$ , which implies to know a way of evaluating the function  $I(\mathbf{R}_L)$ , we propose a different way to compute the ratio of integrals appearing in the first line of eq. 8.29. This second approach, termed SiP-AP (single-point alchemical-path) scheme, has some similarity with other alchemical methods based on equilibrium MD simulations[20, 52, 78]. Noting that  $e^{-\beta\phi(1,\mathbf{R}_L)}$  does not depend on  $\mathbf{R}_L$ [8] and that  $\int I(\mathbf{R}_L) J_{\mathbf{R}_L} d\mathbf{R}_L = V_I$ , we can rewrite eq. 8.32 as

$$g(1) - g(0) = -RT \ln \left( \frac{V_I e^{-\beta\phi(1,\mathbf{R}_L)}}{\int I(\mathbf{R}_L) J_{\mathbf{R}_L} e^{-\beta\phi(0,\mathbf{R}_L)} d\mathbf{R}_L} \right). \quad (8.36)$$

In the previous equation, the quantity  $\mathcal{V}_{\xi_L}$  does not appear in the numerator because the integral over the orientational coordinates of L is included into  $e^{-\beta\phi(1,\mathbf{R}_L)}$  (see eq. 8.30). Substituting eq. 8.36 into eq. 8.35 yields

$$\Delta G_1^\circ = -RT \ln \left( \frac{\sigma_{\text{cp,L}} \sigma_{\text{cp,R}}}{C^\circ \sigma_{\text{gas,L}} \sigma_{\text{sol,R}}} \frac{e^{-\beta\phi(1,\mathbf{R}_L)}}{\int I(\mathbf{R}_L) J_{\mathbf{R}_L} e^{-\beta\phi(0,\mathbf{R}_L)} d\mathbf{R}_L} \right) + P^\circ (\bar{V}_R - \bar{V}_{\text{RL}}). \quad (8.37)$$

With respect to the BiD-AP scheme represented by eq. 8.35, explicit knowledge of the positional binding-site volume  $V_I$  is not necessary in eq. 8.37. On the other side, here we need to compute the integral over  $\mathbf{R}_L$ , which implies to determine the difference between the potentials of mean force for the coupled and uncoupled systems as a function of  $\mathbf{R}_L$ , *i.e.*  $\phi(0, \mathbf{R}_L) - \phi(1, \mathbf{R}_L)$ . Indeed, this may not be a simple task. To tackle this problem, we resort to a reference configuration of the complex RL featured by an established position of L, say  $\mathbf{R}'_L$ . The definition of this configurational state allows us to write

$$\frac{e^{-\beta\phi(1,\mathbf{R}_L)}}{\int I(\mathbf{R}_L) J_{\mathbf{R}_L} e^{-\beta\phi(0,\mathbf{R}_L)} d\mathbf{R}_L} = \frac{e^{\beta[\phi(0,\mathbf{R}'_L) - \phi(1,\mathbf{R}'_L)]}}{\int I(\mathbf{R}_L) J_{\mathbf{R}_L} e^{\beta[\phi(0,\mathbf{R}'_L) - \phi(0,\mathbf{R}_L)]} d\mathbf{R}_L}, \quad (8.38)$$

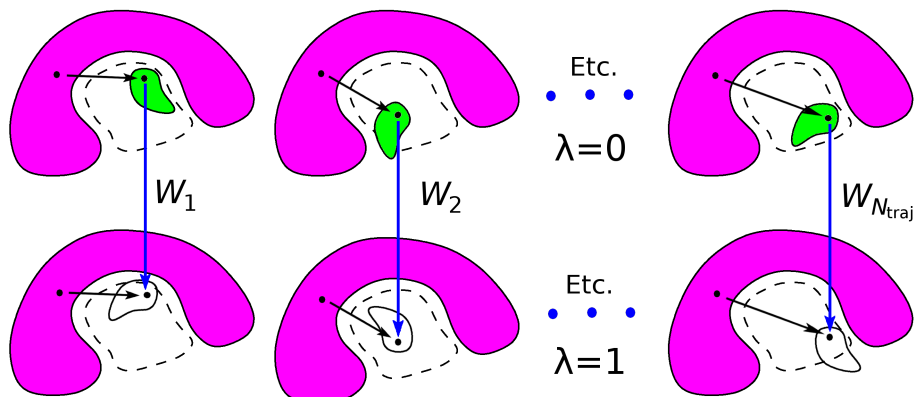


**Figure 8.2:** Schematic illustration of the BiD-AP scheme. R is displayed in magenta, while L in the coupled and uncoupled states is in green and white, respectively. The black circles are the origins of the R and L-frames. The volume  $V_I = \int I(\mathbf{R}_L) J_{\mathbf{R}_L} d\mathbf{R}_L$  entering eq. 8.35 is computed from an equilibrium simulation of the complex in the binding site defined by the dashed lines. The initial microstates of the alchemical trajectories are represented by the top configurations. They are sampled from an equilibrium simulation of the complex in the binding site, with L coupled to R and solvent ( $\lambda = 0$ ). Such a simulation is the one also adopted for computing  $V_I$ . The position of the L-frame relative to the R-frame,  $\mathbf{R}_L$  (black arrows), is fixed during each alchemical trajectory. The final microstates of the alchemical trajectories are represented by the bottom configurations (with L decoupled from R and solvent, *i.e.*,  $\lambda = 1$ ). The work values  $W_1, W_2, \dots, W_{N_{\text{traj}}}$  performed on the system during the alchemical trajectories are calculated using eq. 8.34 and employed into eq. 8.33 to recover  $g(1) - g(0)$ , to be finally used into eq. 8.35.

where, considering that  $\phi(1, \mathbf{R}_L)$  is independent of  $\mathbf{R}_L$ , the equality  $\phi(1, \mathbf{R}_L) = \phi(1, \mathbf{R}'_L)$  has been used. Numerator and denominator of the right hand side of eq. 8.38 can be computed separately. The denominator can be computed from an equilibrium MD simulation of the RL complex (for tight binding), or using some method to sample preferentially bound configurations of the complex, such as the umbrella sampling method[188] (for weak bind-

ing). In any case, regardless of the employed simulation method, configurations featured by  $\mathbf{R}_L = \mathbf{R}'_L$  must be sampled during the equilibrium MD simulation, for being the function  $\phi(0, \mathbf{R}_L)$  defined at the configuration  $\mathbf{R}'_L$ . Therefore, even if the position  $\mathbf{R}'_L$  of the reference configuration can in principle be chosen arbitrarily, it is statistically convenient that  $I(\mathbf{R}'_L) = 1$ , or better that  $\mathbf{R}'_L$  falls in a binding-site region with small value of the potential of mean force (high probability region). We point out that the denominator of the right hand side of eq. 8.38 corresponds to the probability density of finding the ligand at the position  $\mathbf{R}'_L$  once the complex RL is formed. This can be recognized writing the denominator as follows

$$\rho(\mathbf{R}'_L) \equiv \frac{e^{-\beta\phi(0, \mathbf{R}'_L)}}{\int I(\mathbf{R}_L) J_{\mathbf{R}_L} e^{-\beta\phi(0, \mathbf{R}_L)} d\mathbf{R}_L} = \frac{\delta p(\mathbf{R}'_L)}{J_{\mathbf{R}'_L} \delta \mathbf{R}_L}, \quad (8.39)$$

where  $\delta p(\mathbf{R}'_L)$  is the infinitesimal probability that L is found in the volume element  $J_{\mathbf{R}'_L} \delta \mathbf{R}_L$  centered into  $\mathbf{R}'_L$  during an equilibrium sampling of the complex in the bound state. Note that the Jacobian determinant  $J_{\mathbf{R}'_L}$  is computed at the position  $\mathbf{R}'_L$ . Let suppose that the bound state of the complex is sampled through an equilibrium simulation, or, more generally, through a simulation adopting some biasing potential, *e.g.*, using umbrella sampling[188]. In such a situation, we can define a position  $\mathbf{R}'_L$  of L and a resolution  $\delta \mathbf{R}_L$  for establishing when the system takes that position. Denoting the number of times the system visits the configuration  $\mathbf{R}'_L$  as  $\delta \mathcal{N}_{\mathbf{R}'_L}$  and the total number of bound configurations sampled during the MD simulation as  $\mathcal{N}_{\text{tot}}$ , the probability of interest is simply computed as

$$\delta p(\mathbf{R}'_L) = \frac{\delta \mathcal{N}_{\mathbf{R}'_L}}{\mathcal{N}_{\text{tot}}}. \quad (8.40)$$

As stated above,  $\delta p(\mathbf{R}'_L)$  must be computed from an equilibrium MD simulation of the bound complex. This requirement leads to the sampling problems already discussed for the BiD-AP scheme, specifically when dealing with a weakly bound complex. As suggested in sec. 8.3.1, we may resort to hard-walled or restraining potentials to enforce sampling of bound configurations. Additionally, we can employ soft potentials, combined to reweighting procedures[188], to restrain the ligand in the binding site[97, 162, 208]. The numerator of the right hand side of eq. 8.38 is estimated through an alchemical transformation. Concerning instead the state  $\lambda = 1$ , the reciprocal binding site volume  $V_I^{-1}$  is the constant probability density at each  $\mathbf{R}_L$ . Analogously to the BiD-AP scheme, a number of initial microstates are sampled at equilibrium by fixing the position of L to  $\mathbf{R}'_L$ . Starting from these microstates,

nonequilibrium trajectories are performed with an established time schedule for  $\lambda$ , from  $\lambda = 0$  to  $\lambda = 1$ . The works computed from these trajectories via eq. 8.34 are thus employed in the Jarzynski equality[106] (eq. 8.33) to evaluate the free energy difference between the initial and final states, which corresponds to  $\phi(1, \mathbf{R}'_L) - \phi(0, \mathbf{R}'_L)$ . Exploiting now the independence of  $\phi(1, \mathbf{R}_L)$  on the position  $\mathbf{R}_L$ , we may write  $V_I = \int I(\mathbf{R}_L) J_{\mathbf{R}_L} e^{\beta(\phi(1, \mathbf{R}'_L) - \phi(1, \mathbf{R}_L))} d\mathbf{R}_L$ . Moreover, combining eqs. 8.36 and 8.38, we gain the following estimate of  $g(1) - g(0)$ :

$$g(1) - g(0) = \phi(1, \mathbf{R}'_L) - \phi(0, \mathbf{R}'_L) - RT \ln \left( \frac{\int I(\mathbf{R}_L) J_{\mathbf{R}_L} e^{\beta(\phi(1, \mathbf{R}'_L) - \phi(1, \mathbf{R}_L))} d\mathbf{R}_L}{\int I(\mathbf{R}_L) J_{\mathbf{R}_L} e^{\beta(\phi(0, \mathbf{R}'_L) - \phi(0, \mathbf{R}_L))} d\mathbf{R}_L} \right). \quad (8.41)$$

It is straightforward to note that eq. 8.41 formally resembles eq. 7.6 for PLD estimate of free energy difference  $\Delta F_{AB}$  between  $D_A$  and  $D_B$  conformational domains (sec. 7.2), replaced respectively by the states  $\lambda = 0$  and  $\lambda = 1$ , in the domain of configurations  $\mathbf{R}_L$  for which  $I(\mathbf{R}_L) = 1$ . Moreover,  $\phi(1, \mathbf{R}'_L) - \phi(0, \mathbf{R}'_L)$ , calculated in the single point  $\mathbf{R}'_L$ , replaces pmf difference  $\Delta\Phi_{AB} = \Phi(\mathbf{z}_b) - \Phi(\mathbf{z}_a)$ , with  $\mathbf{z}_a$  and  $\mathbf{z}_b$  being two any points of the conformational space located inside the  $D_A$  and  $D_B$  domains. We see, hence, that SiP-AP consists of adaptation of PLD scheme (chapter 7), conceived in the context of conformational studies, to calculation of  $g(1) - g(0)$ . In summary, considering the introduction of a reference configuration (eq. 8.38) and the definition of probability density (eq. 8.39),  $\Delta G_1^\circ$  can be rewritten as

$$\Delta G_1^\circ = \phi(1, \mathbf{R}'_L) - \phi(0, \mathbf{R}'_L) - RT \ln \left( \rho(\mathbf{R}'_L) \frac{\sigma_{\text{cp,L}} \sigma_{\text{cp,R}}}{C^\circ \sigma_{\text{gas,L}} \sigma_{\text{sol,R}}} \right) + P^\circ (\bar{V}_R - \bar{V}_{\text{RL}}), \quad (8.42)$$

where  $\rho(\mathbf{R}'_L)$  and the difference  $\phi(1, \mathbf{R}'_L) - \phi(0, \mathbf{R}'_L)$  are computed as described above. A schematic illustration of the SiP-AP scheme is shown and shortly described in fig. 8.3. We point out that, when NPT simulations are performed in the place of NVT simulations, eq. 8.42 still holds, with the only difference that no corrections dependent upon the partial molar volumes  $\bar{V}_R$  and  $\bar{V}_{\text{RL}}$  have to be considered. Moreover, it is important to note that the SiP-AP scheme can be applied with both equilibrium (*e.g.*, thermodynamic integration[20]) and nonequilibrium alchemical simulations, while the BiD-AP methodology is intrinsically a nonequilibrium simulation technique. As a matter of fact, applying the SiP-AP scheme in an equilibrium simulation framework, which simply corresponds to enforce a constraint to the translations of the ligand, is straightforward, as shown, for example, by Deng and Roux in ref. [52]. In this regard, eq. 8.42 may be viewed[158] as an original reformulation of the

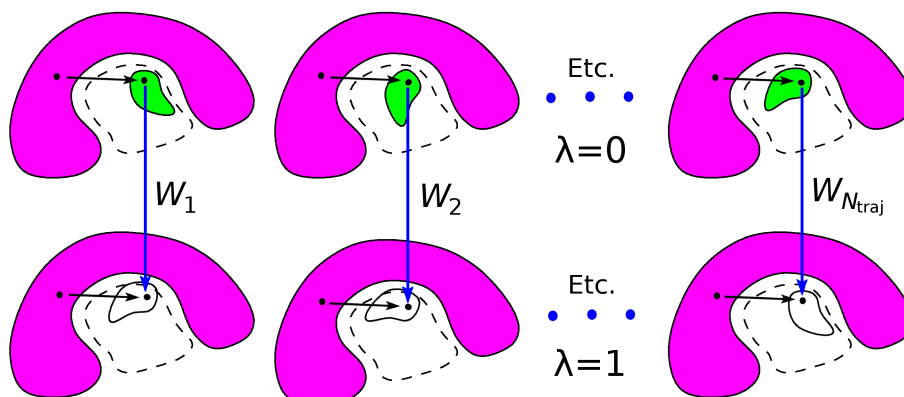


**Figure 8.3:** Schematic illustration of the SiP-AP scheme. R is displayed in magenta, while L in the coupled and uncoupled states is in green and white, respectively. The black circles are the origins of the R and L-frames. The quantity  $\rho(\mathbf{R}'_L)$  entering eq. 8.42 is computed from an equilibrium simulation of the complex in the binding site defined by the dashed lines (no constraints are applied to L). The initial microstates of the alchemical trajectories are represented by the top configurations. They are sampled from an equilibrium simulation of the complex in which L is fixed at the position  $\mathbf{R}'_L$  (black arrows) and coupled to R and solvent ( $\lambda = 0$ ). The position of L,  $\mathbf{R}'_L$ , is fixed during each alchemical trajectory and is the same for all trajectories. The final microstates of the alchemical trajectories are represented by the bottom configurations (with L decoupled from R and solvent, *i.e.*,  $\lambda = 1$ ). The work values  $W_1, W_2, \dots, W_{N_{\text{traj}}}$  performed on the system during the alchemical trajectories are calculated using eq. 8.34 and employed into eq. 8.33 to recover  $\phi(1, \mathbf{R}'_L) - \phi(0, \mathbf{R}'_L)$ , to be finally used into eq. 8.42.

Deng and Roux approach in the limit of strong restraints, where only the ligand position vector is held fixed at  $\mathbf{R}'_L$  during the alchemical decoupling.

### 8.3.2 Decoupling the ligand from the solvent: $\Delta G_2^\circ$ calculation

The contribution  $\Delta G_2^\circ$  to  $\Delta G^\circ$  corresponds to the free energy difference between the state in which L is decoupled from the solvent (L in gas phase and pure solvent in condensed phase)



and the state in which L is coupled to the solvent (solution of L in the solvent). From the physical standpoint,  $\Delta G_2^\circ$  therefore represents the desolvation free energy of L. It is obtained substituting eqs. 8.12 and 8.20 into eq. 8.17,

$$\Delta G_2^\circ = -RT \ln \left( \frac{\sigma_{\text{sol,L}}}{\sigma_{\text{gas,L}}} \frac{Z_{N,0} Z_{0,L}}{Z_{N,L}} \right) - P^\circ \bar{V}_L, \quad (8.43)$$

where  $Z_{N,L}$ ,  $Z_{N,0}$  and  $Z_{0,L}$  are the usual configuration integrals. At variance with  $\Delta G_1^\circ$ , the contribution  $\Delta G_2^\circ$  does not depend upon the choice of the standard concentration. In this case, the artificial energy function  $U(\lambda, \zeta_L, \mathbf{r}_L, \mathbf{r}_S)$  does not depend upon the internal coordinates of R, as we simply deal with L in the solvent. The requirements on  $U$  are that for  $\lambda = 0$  and  $\lambda = 1$  the artificial energy function must correspond to the energy functions of the coupled and uncoupled states of L in the solvent, respectively:

$$U(0, \zeta_L, \mathbf{r}_L, \mathbf{r}_S) = U(\zeta_L, \mathbf{r}_L, \mathbf{r}_S), \quad (8.44)$$

$$U(1, \zeta_L, \mathbf{r}_L, \mathbf{r}_S) = U(\mathbf{r}_S) + U(\mathbf{r}_L), \quad (8.45)$$

where the external coordinates of L are now relative to the lab-frame. A free energy function dependent parametrically on  $\lambda$  can be built exploiting the artificial energy function as

$$g(\lambda) = -RT \ln \left( \int J_{\zeta_L} e^{-\beta U(\lambda, \zeta_L, \mathbf{r}_L, \mathbf{r}_S)} d\zeta_L d\mathbf{r}_L d\mathbf{r}_S \right). \quad (8.46)$$

According to  $g(\lambda)$  and to the requirements of eqs. 8.44 and 8.45, the free energy difference between the final and initial states is

$$\begin{aligned} g(1) - g(0) &= -RT \ln \left( \frac{\int J_{\zeta_L} e^{-\beta U(\mathbf{r}_S)} e^{-\beta U(\mathbf{r}_L)} d\zeta_L d\mathbf{r}_L d\mathbf{r}_S}{\int J_{\zeta_L} e^{-\beta U(\zeta_L, \mathbf{r}_L, \mathbf{r}_S)} d\zeta_L d\mathbf{r}_L d\mathbf{r}_S} \right) \\ &= -RT \ln \left( \frac{Z_{N,0} Z_{0,L}}{Z_{N,L}} \right). \end{aligned} \quad (8.47)$$

Note that the integrals over the internal coordinates of the solute,  $\mathbf{r}_L$ , and over the coordinates of the solvent,  $\mathbf{r}_S$ , do not depend upon the position or orientation of the solute,  $\zeta_L$ , and hence the integrals over  $\zeta_L$  may be carried out at once yielding  $V \mathcal{V}_{\zeta_L}$ , where  $V$  is the volume of the container (simulation box) and arises from the integral over the position  $\mathbf{R}_L$ , while  $\mathcal{V}_{\zeta_L}$  arises from the integral over the orientation  $(\xi_{L,1}, \xi_{L,2}, \xi_{L,3})$ . As this volume term

appears in both numerator and denominator of eq. 8.47, it cancels out. We may now define the free energy function  $g(\lambda)$  in terms of the potential of mean force as a function of position and orientation of the ligand:

$$g(\lambda) = -RT \ln \left( \int J_{\zeta_L} e^{-\beta\Phi(\lambda, \zeta_L)} d\zeta_L \right), \quad (8.48)$$

where

$$e^{-\beta\Phi(\lambda, \zeta_L)} = \int e^{-\beta U(\lambda, \zeta_L, \mathbf{r}_L, \mathbf{r}_S)} d\mathbf{r}_L d\mathbf{r}_S. \quad (8.49)$$

As observed above, the integrals over  $\mathbf{r}_L$  and  $\mathbf{r}_S$  into eq. 8.49 do not depend upon  $\zeta_L$ . For this reason, the potential of mean force  $\Phi(\lambda, \zeta_L)$  is independent of  $\zeta_L$  and hence it will be denoted as  $\Phi(\lambda)$ . This allows to write eq. 8.48 as

$$g(\lambda) = \Phi(\lambda) - RT \ln(V\mathcal{V}_{\zeta_L}). \quad (8.50)$$

Using eq. 8.50 into eq. 8.47 for expressing  $g(0)$  and  $g(1)$  and substituting the resulting equation into eq. 8.43 yields

$$\Delta G_2^\circ = \Phi(1) - \Phi(0) - RT \ln \left( \frac{\sigma_{\text{sol,L}}}{\sigma_{\text{gas,L}}} \right) - P^\circ \bar{V}_L. \quad (8.51)$$

We notice that the knowledge of  $\sigma_{\text{gas,L}}$  is not mandatory, because it drops out when eq. 8.51 is recombined with eq. 8.35 (if using BiD-AP) or eq. 8.42 (if using SiP-AP) to recover  $\Delta G^\circ$  via eq. 8.18. Operatively,  $\Delta G_2^\circ$  can be computed using nonequilibrium MD simulations in the usual way. First, a set of initial microstates is produced through an equilibrium MD simulation of one L molecule into  $N$  solvent molecules (without any constraint). Starting from these microstates, nonequilibrium trajectories are performed with an established time schedule for  $\lambda$ , starting from  $\lambda = 0$  (coupled ligand) and ending to  $\lambda = 1$  (uncoupled ligand). The works computed from these alchemical trajectories by means of a relationship analogous to eq. 8.34[9] are then employed in the Jarzynski equality[106] (eq. 8.33) to evaluate the free energy difference  $\Phi(1) - \Phi(0)$ , to be finally used into eq. 8.51.

## 8.4 Using the ligand-receptor distance as binding descriptor in the double-decoupling method

The alchemical schemes presented in Secs. 8.3.1 and 8.3.1 are based on a binding descriptor relying on the position of a reference atom of L relative to an atom of R, specifically the  $\mathbf{R}_L$  vector. A special important case of such an approach is to use a binding descriptor based on the magnitude of  $\mathbf{R}_L$ . In this section, we discuss how the basic relationships of the method, namely eq. 8.35 for the BiD-AP scheme and eq. 8.42 (together with the companion eqs. 8.39 and 8.40) for the SiP-AP scheme, are modified upon using  $|\mathbf{R}_L|$  as binding descriptor. To simplify the notation, let define the distance between the origins of the L and R-frames as  $r$ , namely  $r \equiv |\mathbf{R}_L|$ . Without loss of generality, the origin of the L-frame, as well as that of the R-frame, can be an atom, the centroid of a subset of atoms or the center of mass. The distance  $r$  is the parameter taken to establish when the complex is or is not in place, according to the value of the step function  $I(r)$ , which can be 1 or 0. In principle, to apply this criterion, we need to define two threshold distances, say  $r_1$  and  $r_2$ , such that  $I(r) = 1$  if  $r_1 < r < r_2$  and  $I(r) = 0$  otherwise. However, as emerged from the previous discussion, the step function enters the double-decoupling method in no explicit way. This suggests that one may not need to define  $r_1$  and  $r_2$ , provided that a “way” can be devised to sample most of the bound configurations during an equilibrium MD simulation. As already discussed in Secs. 8.3.1 and 8.3.1, for complexes with large binding constants, this “way” can be guaranteed from the equilibrium simulation itself, because the complex, owing to its stability, never dissociates during the simulation. Problems may instead occur when dealing with weakly bound complexes. These situations can be treated only introducing some external information on shape and size of the binding site, through a geometrical definition of  $I(r)$ , via hard-walled or soft restraining potentials. Of course, in these restraining strategies, significant errors can be introduced, arising from being the binding free energy basin ill defined. For this reason, the weaker the binding, the greater the error. In the limit case of an almost flat free energy binding basin, one has to resort to some arbitrary criterion to define  $I(r)$ , calling into play physical features of the complex, which do not include the mere energetical stability. Considering that the coordinate  $r$  corresponds to the distance between the origins of the R and L-frames, it is a natural choice to use spherical polar coordinates for representing  $\mathbf{R}_L$ , *i.e.*  $\mathbf{R}_L \equiv (r, \theta, \varphi)$ , where  $\theta$  is the angle between  $\mathbf{R}_L$  and the  $z$ -axis

of the R-frame and  $\varphi$  is the angle formed by the projection of  $\mathbf{R}_L$  on the  $xy$ -plane of the R-frame and the  $x$ -axis of the same frame. Then, we make explicit the coordinates  $r$ ,  $\theta$  and  $\varphi$  into eq. 8.28, expressing the step function  $I(\mathbf{R}_L)$  in terms of the  $r$  coordinate:

$$g(\lambda) = -RT \ln \left( \int I(r) r^2 \sin \theta J_{\xi_L} e^{-\beta U(\lambda, \mathbf{R}_L, \xi_L, \mathbf{r}_L, \mathbf{r}_R, \mathbf{r}_S)} d\mathbf{R}_L d\xi_L d\mathbf{r}_L d\mathbf{r}_R d\mathbf{r}_S \right), \quad (8.52)$$

where  $r^2 \sin \theta$  is the Jacobian determinant  $J_{\mathbf{R}_L}$  and, for the sake of compactness,  $\mathbf{R}_L \equiv (r, \theta, \varphi)$  and  $d\mathbf{R}_L \equiv dr d\theta d\varphi$ . The other symbols in eq. 8.52 preserve their original meaning. Thus, the free energy difference  $g(1) - g(0)$  of eq. 8.29 becomes

$$\begin{aligned} g(1) - g(0) &= -RT \ln \left( \frac{\int I(r) r^2 \sin \theta J_{\xi_L} e^{-\beta U(\mathbf{r}_R, \mathbf{r}_S)} e^{-\beta U(\mathbf{r}_L)} d\mathbf{R}_L d\xi_L d\mathbf{r}_L d\mathbf{r}_R d\mathbf{r}_S}{\int I(r) r^2 \sin \theta J_{\xi_L} e^{-\beta U(\mathbf{R}_L, \xi_L, \mathbf{r}_L, \mathbf{r}_R, \mathbf{r}_S)} d\mathbf{R}_L d\xi_L d\mathbf{r}_L d\mathbf{r}_R d\mathbf{r}_S} \right) \\ &= -RT \ln \left( 4\pi V_I \mathcal{V}_{\xi_L} \frac{Z_{N,R} Z_{0,L}}{Z_{N,RL}} \right). \end{aligned} \quad (8.53)$$

In the second line of the previous equation, the factor  $4\pi$  arises from integration over  $\theta$  and  $\varphi$ , the factor  $\mathcal{V}_{\xi_L}$  (equal to  $8\pi^2$ ,  $4\pi$  or 1 according to the structure of L) arises from integration over the orientational coordinates of L (*i.e.*,  $\xi_L$ ) and  $V_I = \int I(r) r^2 dr$ . The second line of eq. 8.53 allows us to write  $\Delta G_1^\circ$  of eq. 8.22 as (*viz.* eq. 8.35)

$$\Delta G_1^\circ = g(1) - g(0) - RT \ln \left( \frac{1}{4\pi V_I C^\circ} \frac{\sigma_{cp,L} \sigma_{cp,R}}{\sigma_{gas,L} \sigma_{sol,R}} \right) + P^\circ (\bar{V}_R - \bar{V}_{RL}). \quad (8.54)$$

This relationship allows to estimate  $\Delta G_1^\circ$  through the BiD-AP scheme, as explained in sec. 8.3.1. In order to adopt the SiP-AP scheme, we have to recognize that the unnormalized average probability of finding the ligand in a generic point at a distance  $r$  from the origin of the R-frame (for a given  $\lambda$ ) corresponds, up to a multiplication factor, to the radial distribution function, which, in turn, equals the exponential of the potential of mean force,  $e^{-\beta\phi(\lambda,r)}$ :

$$e^{-\beta\phi(\lambda,r)} = \frac{1}{4\pi} \int \sin \theta J_{\xi_L} e^{-\beta U(\lambda, r, \theta, \phi, \xi_L, \mathbf{r}_L, \mathbf{r}_R, \mathbf{r}_S)} d\theta d\phi d\xi_L d\mathbf{r}_L d\mathbf{r}_R d\mathbf{r}_S. \quad (8.55)$$

The quantity  $4\pi r^2 e^{-\beta\phi(\lambda,r)} dr$  is therefore proportional to the probability of finding L into a spherical shell of radius  $r$  and thickness  $dr$  centered at the origin of the R-frame. According to the above definition of potential of mean force, the free energy function  $g(\lambda)$  (eq. 8.52)

becomes

$$g(\lambda) = -RT \ln \left( \int I(r) 4\pi r^2 e^{-\beta\phi(\lambda,r)} dr \right). \quad (8.56)$$

Used in the first line of eq. 8.53, the previous equation gives the free energy difference  $g(1) - g(0)$

$$g(1) - g(0) = -RT \ln \left( \frac{4\pi V_I e^{-\beta\phi(1,r)}}{\int I(r) 4\pi r^2 e^{-\beta\phi(0,r)} dr} \right). \quad (8.57)$$

In this equation, integration over  $r$  is carried out because  $\phi(1,r)$  does not depend on  $r$  (analogously to  $\phi(1, \mathbf{R}_L)$  in eq. 8.36). Using eq. 8.57 into eq. 8.54 yields

$$\Delta G_1^\circ = -RT \ln \left( \frac{\sigma_{\text{cp,L}} \sigma_{\text{cp,R}}}{C^\circ \sigma_{\text{gas,L}} \sigma_{\text{sol,R}}} \frac{e^{-\beta\phi(1,r)}}{\int I(r) 4\pi r^2 e^{-\beta\phi(0,r)} dr} \right) + P^\circ (\bar{V}_R - \bar{V}_{\text{RL}}). \quad (8.58)$$

As done in sec. 8.3.1, we introduce a reference configuration corresponding to  $r = r'$ , with  $r'$  being an arbitrary established value of  $r$  (in analogy with  $\mathbf{R}'_L$  of sec. 8.3.1). This allows to write

$$\frac{e^{-\beta\phi(1,r)}}{\int I(r) 4\pi r^2 e^{-\beta\phi(0,r)} dr} = \frac{e^{\beta[\phi(0,r') - \phi(1,r')]} e^{-\beta\phi(0,r')}}{\int I(r) 4\pi r^2 e^{-\beta\phi(0,r)} dr}, \quad (8.59)$$

where, the equality  $\phi(1,r) = \phi(1,r')$  has been used. According to the SiP-AP scheme, the free energy difference  $\phi(1,r') - \phi(0,r')$  in the numerator of eq. 8.59 is estimated by means of alchemical transformations. A number of initial microstates of the coupled system ( $\lambda = 0$ ) are sampled at the fixed  $r = r'$ . Starting from these microstates, nonequilibrium trajectories are performed with an established time schedule for  $\lambda$ , from  $\lambda = 0$  to  $\lambda = 1$ . The works computed from these trajectories via eq. 8.34 are thus employed in the Jarzynski equality[106] (eq. 8.33). The remaining part of eq. 8.59 is computed upon considering that it corresponds to the probability density of finding L in a generic point at the distance  $r'$  from the origin of the R-frame, once the complex is in a bound configuration, *i.e.*,  $I(r) = 1$ :

$$\rho(r') = \frac{e^{-\beta\phi(0,r')}}{\int I(r) 4\pi r^2 e^{-\beta\phi(0,r)} dr} = \frac{\delta p(r')}{4\pi r'^2 \delta r}, \quad (8.60)$$

where  $\delta p(r')$  is the infinitesimal probability that L is found in a spherical shell of radius  $r'$  and volume  $4\pi r'^2 \delta r$  (the center being the reference R point) during an equilibrium MD simulation with the complex restrained in the bound state. This simulation can be carried

out as explained in sec. 8.3.1 (see discussion of eq. 8.40). In summary, considering the introduction of a reference configuration (eq. 8.59) and the definition of probability density (eq. 8.60),  $\Delta G_1^\circ$  of eq. 8.58 can be rewritten as

$$\Delta G_1^\circ = \phi(1, r') - \phi(0, r') - RT \ln \left( \rho(r') \frac{\sigma_{\text{cp,L}} \sigma_{\text{cp,R}}}{C^\circ \sigma_{\text{gas,L}} \sigma_{\text{sol,R}}} \right) + P^\circ (\bar{V}_R - \bar{V}_{\text{RL}}). \quad (8.61)$$

As discussed previously, the quantity  $\phi(1, r') - \phi(0, r')$  is computed evaluating the difference of the potential of mean force of coupled and uncoupled states via nonequilibrium alchemical transformations by constraining the ligand-receptor distance  $r$  to the value of  $r'$ . The quantity  $\rho(r')$  is computed from eq. 8.60.

## 8.5 Zn(II)-anion complex

### 8.5.1 Computational details

The first example considered to illustrate and to numerically test the BiD-AP and SiP-AP alchemical schemes is a ligand-receptor system formed by a Zn(II) cation, the ligand, and a N-hydroxypropanamide monovalent anion, the receptor (fig. 8.4). Simulations were performed in a solvent consisting of 336 rigid water molecules modeled by the TIP3P force field[112]. For the anion, the AMBER-like ff99sb force field is used[101] in combination with atomic charges computed through a RESP fit[15] at the B3LYP/6-31G(d) level[16, 123]. The Lennard-Jones parameters for Zn(II) are from ref. [164]. A cubic simulation box is used with periodic boundary conditions. Constant-pressure constant-temperature equations of motion are adopted for both equilibrium and nonequilibrium simulations, setting the pressure to 0.1 MPa and the temperature to 300 K. Constant pressure is enforced isotropically using a modification of the Parrinello-Rahman Lagrangian[131], while temperature control is achieved through a Nosé-Hoover thermostat[99, 100]. The electrostatic interactions are accounted for by using the smooth particle mesh Ewald method[60], with a convergence parameter of  $0.5 \text{ \AA}^{-1}$ . The grid along each direction of the space is partitioned into 16 points, giving a grid spacing slightly above  $1 \text{ \AA}$ , and a fourth order B-spline interpolation is used for evaluating the gridded charge array. The equations of motion are integrated using a multiple time-step r-RESPA scheme[191], with greatest time-step equal to 10 fs. The cutoff for Lennard-Jones and direct lattice electrostatic interactions is  $9.7 \text{ \AA}$ . Constraints are applied

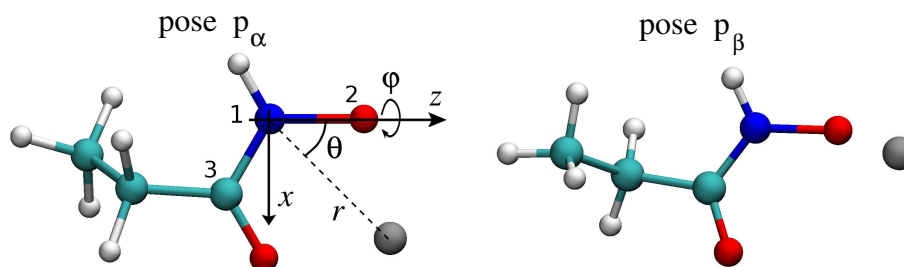


**Figure 8.4:** Structure of the Zn(II)·N-hydroxypropanamide complex. The atoms involved in the definition of the Cartesian R-frame are numbered according to the text. The  $x$  and  $z$  axes are displayed, while the  $y$  axis, orthogonal to the  $xz$  plane, is oriented in agreement with the right-hand rule. The spherical polar coordinates associated with the Cartesian frame are also shown. The two configurations of the complex represent the  $p_\alpha$  and  $p_\beta$  poses considered in the present study. The poses are defined on the basis of the R-frame position of Zn(II). Therefore, the orientational arrangement of the ethyl group is immaterial.

to C-H covalent bonds. Simulations were performed with the ORAC program[134, 154], while DFT calculations were performed with the Gaussian 09 program[71]. To establish when a bound configuration of the RL complex occurs, we need to specify the external coordinates  $\mathbf{R}_L$  of L (the cation) relative to R (the anion). In our case, such coordinates are simply those of the cation. From a general point of view, to get a proper representation of bound and unbound configurations in terms of  $\mathbf{R}_L$ , it is convenient to choose reference atoms of R involved in the RL binding[80]. Moreover, one has to assume that the flexibility of R does not affect significantly the binding and hence care should be taken in selecting R reference atoms forming an almost rigid frame[20, 80]. Here, considering that the binding site does not involve the ethyl group of R and that such a moiety is highly flexible, the atoms candidate to define the R-frame are the nitrogen, oxygen and the carbon of the carbonyl group. Specifically, the R-frame is defined according to the positions of the atoms labeled with 1, 2 and 3 in fig. 8.4. Denoting the coordinates of these atoms in the lab-frame as  $\mathbf{r}_1$ ,  $\mathbf{r}_2$  and  $\mathbf{r}_3$ , the origin of the R-frame is taken on the atom 1, the  $z$  axis is along the vector  $\mathbf{r}_2 - \mathbf{r}_1$ , the  $x$  axis is along the projection of  $\mathbf{r}_3 - \mathbf{r}_2$  on the plane orthogonal to  $\mathbf{r}_2 - \mathbf{r}_1$  and

the  $y$  axis is orthogonal to the  $xz$  plane and oriented according to right-hand rule. On the basis of the R-frame defined above, we more conveniently assign the position of L through its spherical polar coordinates, so that  $\mathbf{R}_L \equiv (r, \theta, \varphi)$ . The coordinates  $r$ ,  $\theta$  and  $\varphi$  are also displayed in fig. 8.4. In the present tests, we compute the ABFEs for the poses of the RL complex represented in fig. 8.4, from now on referred to as  $p_\alpha$  and  $p_\beta$ . The pose  $p_\alpha$  is characterized by two H-bonds between L and the oxygen atoms of R and is represented by a configurational distribution within the following ranges of coordinates:  $r \in (2.5, 2.8) \text{ \AA}$ ,  $\theta \in (42, 55)$  degrees and  $\varphi \in [(0, 30) \cup (330, 360)]$  degrees. The pose  $p_\beta$  is instead associated with configurations in the ranges of coordinates  $r \in (2.7, 3.4) \text{ \AA}$ ,  $\theta \in (15, 40)$  degrees and  $\phi \in [(0, 100) \cup (260, 360)]$  degrees, all being featured by a single H-bond. Such ranges are in agreement with outcomes of equilibrium simulations described below. We point out that, in the present simulations, no conformational transition around the C-N covalent bond has been observed due to the high rotational barrier featuring the amide bond. Thus, the  $p_\alpha$  and  $p_\beta$  poses are exclusively those for which oxygen atoms are in cis position. In the system under study, the symmetry numbers of R and L do not vary upon a change of phase (gas/solution), or going in the solvated RL complex, namely  $\sigma_{\text{cp,L}} = \sigma_{\text{gas,L}} = \sigma_{\text{sol,L}}$  and  $\sigma_{\text{cp,R}} = \sigma_{\text{sol,R}}$ . This implies that the symmetry numbers cancel out into eqs. 8.35, 8.42 and 8.51 and hence do not affect the ABFE. Moreover, as the volumes  $\bar{V}_L$ ,  $\bar{V}_R$  and  $\bar{V}_{\text{RL}}$  do not enter when NPT simulations are performed, the above relationships are further simplified:

$$\Delta G_1^\circ = g(1) - g(0) + RT \ln(C^\circ V_I) \text{ BiD-AP}, \quad (8.62)$$

$$\Delta G_1^\circ = \phi(1, \mathbf{R}'_L) - \phi(0, \mathbf{R}'_L) - RT \ln(\rho(\mathbf{R}'_L)/C^\circ) \text{ SiP-AP}, \quad (8.63)$$

$$\Delta G_2^\circ = \Phi(1) - \Phi(0). \quad (8.64)$$

Evaluating the ABFE (eq. 8.18) requires three independent series of calculations, using either BiD-AP or SiP-AP scheme. One series involves the use of alchemical simulations to estimate  $g(1) - g(0)$  (BiD-AP) or  $\phi(1, \mathbf{R}'_L) - \phi(0, \mathbf{R}'_L)$  (SiP-AP). A further calculation is necessary for the complete evaluation of  $\Delta G_1^\circ$ , which consists of an equilibrium simulation of the solvated RL system to estimate the binding-site volume  $V_I$  (BiD-AP) or the probability density  $\rho(\mathbf{R}'_L)$  (SiP-AP). The third type of calculation, common to both BiD-AP and SiP-AP schemes, is aimed at evaluating, through alchemical transformations, the desolvation free energy of L, namely the quantity  $\Phi(1) - \Phi(0)$  (eq. 8.51). To test numerically the present



alchemical approaches, we again apply PLD scheme (chapter 7) in its original context of conformational equilibria. The computational protocol is organized into three stages that can be carried on simultaneously. Two of them consist of independent simulations aimed at sampling  $p_\alpha$  and  $p_\beta$  poses to estimate local configuration integrals. Actually, these two stages are not realized, because they correspond to the evaluation of  $\rho(\mathbf{R}_L)$  for the two poses. The calculation is completed by the linking-path stage, in which the Potential of Mean Force (PMF) difference is estimated between the  $\mathbf{R}'_L$  points of the two poses. The linking path in the space of the collective coordinates is arbitrary and is computed with nonequilibrium techniques. By means of the PLD method we get  $\Delta G_{\alpha\beta}^\circ = G_\beta^\circ - G_\alpha^\circ$ , where  $G_\alpha^\circ$  and  $G_\beta^\circ$  are the free energies of the complex in the  $p_\alpha$  and  $p_\beta$  poses. On the basis of a thermodynamic cycle, we can compare  $\Delta G_{\alpha\beta}^\circ$  to the difference  $\Delta G_\beta^\circ - \Delta G_\alpha^\circ$ , with  $\Delta G_\beta^\circ$  and  $\Delta G_\alpha^\circ$  being the ABFEs of the complex in the  $p_\beta$  and  $p_\alpha$  poses computed by means of alchemical transformations.

## 8.5.2 Results

### BiD-AP: Binding-site volume contribution to the ABFE

In order to evaluate the uncertainty on the free energy contribution  $RT \ln(C^\circ V_I)$  to the ABFE (eq. 8.62),  $V_I$  is determined according to a criterion based on a maximum free-energy threshold. In the following, such a threshold will be indicated as  $\phi_{\text{thr}}$ . The dependence of  $RT \ln(C^\circ V_I)$  on  $\phi_{\text{thr}}$  is reported in fig. 8.5A. Increasing  $\phi_{\text{thr}}$ , a systematic enhancement of  $V_I$  is expected, because more configurations of the complex are accounted for in the calculation. This implies that the quantity  $RT \ln(C^\circ V_I)$  also increases, ultimately leading to a decrease of  $\Delta G^\circ$ . Such a trend is clearly observed in fig. 8.5A. For both poses, the growth of  $\phi_{\text{thr}}$  from  $RT$  to  $8 RT$  corresponds to a free energy increase of approximately  $8 \text{ kJ mol}^{-1}$ . For higher  $\phi_{\text{thr}}$  values,  $RT \ln(C^\circ V_I)$  appears to converge. Convergence is due to the fact that no configuration of the complex is sampled in PMF regions above the minimum by more than 10 and  $8 RT$  for the  $p_\alpha$  and  $p_\beta$  poses, respectively. This trend is however spurious in unrestrained simulations such as ours. As a matter of fact, for a very long equilibrium simulation of the unrestrained R and L compounds, one would expect that also unbound configurations are sampled with a probability dependent on the size of the simulation box. Thus, in the infinite time limit,  $V_I$  would correspond to the volume of the simulation box.

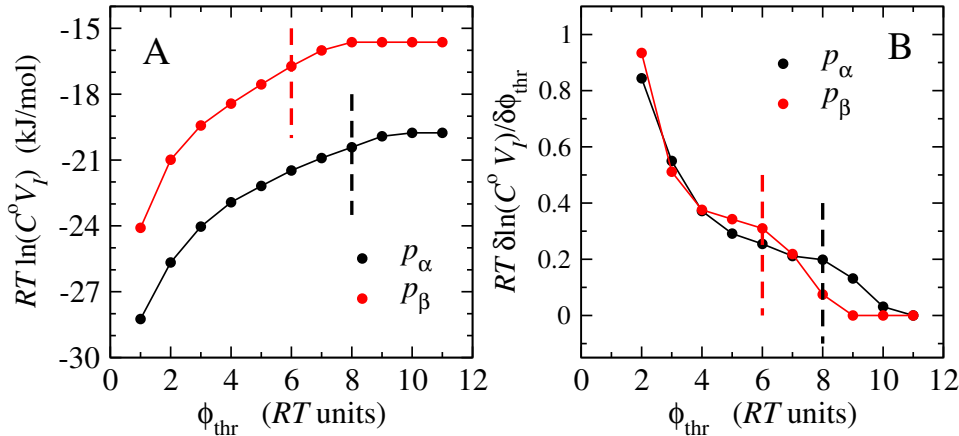


**Figure 8.5:** *Panel A.* ABFE contribution arising from  $V_I$ , namely  $RT \ln(C^\circ V_I)$ , as a function of the PMF threshold  $\phi_{\text{thr}}$ , computed for the  $p_\alpha$  and  $p_\beta$  poses (see legend). *Panel B.* Numerical derivative of  $RT \ln(C^\circ V_I)$  with respect to  $\phi_{\text{thr}}$  (eq. 8.65) as a function of  $\phi_{\text{thr}}$ , computed for the  $p_\alpha$  and  $p_\beta$  poses (see legend). Solid lines are guides for eyes. Dashed lines represent the values of  $\phi_{\text{thr}}$  taken as final values to compute the ABFE of the two poses.

This effect should be observed more easily for weakly bound ligand-receptor systems, because dissociation is more frequent. The dissociation of the RL complex could be avoided introducing some restraint to force L to remain within the binding site[52]. Nonetheless, the value of  $V_I$  would depend on the strength of the restraining potential, which is in principle arbitrary. Such a drawback is hard to be avoided, since even in the theory[83] there is no statement aimed at identifying univocally bound configurations of the complex. In some sense, this “decision” is left to the researcher. Strictly speaking, the size of the binding site is somehow related to the property employed to estimate the ABFE experimentally. Typically, in experimental measurements, a property changing upon complexation is probed (*e.g.*, fluorescence). Therefore, the bound configurations “seen” in the experiment depend on how large is the change of the probed property when varying the mutual arrangement of ligand and receptor. In this picture, the volume  $V_I$  is related to the region of the configurational space, in general unknown, where the probed property takes some well-defined value,

which differs significantly from that measured when the receptor and the ligand are far apart (unbound configurations). The computational problem of defining bound configurations of the complex is less dramatic when tight binding is established, like in our case. In this situation, one can leave the natural affinity between L and R to act as a sort of “implicit restraint”, provided that dissociation is not observed during the simulation[80]. However, we must be aware that such a procedure is virtually of nonequilibrium, being based on the relatively short duration of the simulation. In spite of this, it is arguable that single dissociation events are usually very fast, even if occurring with a low rate. This fact allows us to identify more easily  $V_I$  as the volume explored by the ligand before the first dissociation event. In our case, dissociation is never observed during the equilibrium simulations and hence all sampled configurations can in principle be taken to compute  $V_I$ . However, as anticipated above, to quantify the uncertainty on  $V_I$ , we set the boundaries of the binding site, by limiting  $\phi_{\text{thr}}$  to a value beyond which no significant change of  $RT \ln(C^\circ V_I)$  is observed. This change of regime of  $RT \ln(C^\circ V_I)$  against  $\phi_{\text{thr}}$  can be more conveniently identified through the derivative, computed numerically as the incremental ratio

$$RT \left[ \frac{\delta \ln(C^\circ V_I)}{\delta \phi_{\text{thr}}} \right]_{\phi_{\text{thr}}} = RT \frac{[\ln C^\circ V_I]_{\phi_{\text{thr}} + \Delta \phi_{\text{thr}}} - [\ln C^\circ V_I]_{\phi_{\text{thr}} - \Delta \phi_{\text{thr}}}}{2 \Delta \phi_{\text{thr}}}. \quad (8.65)$$

In this equation, the subscripts indicate the threshold used to compute the quantities into square brackets and  $\Delta \phi_{\text{thr}} = RT$ . The free energy derivative as a function of  $\phi_{\text{thr}}$  is reported in fig. 8.5B for the two poses. In both cases, a rapid damping is observed till about  $\phi_{\text{thr}} = 4 RT$ . For greater  $\phi_{\text{thr}}$ , the derivative continues to decrease slowly till  $\phi_{\text{thr}} = 8 RT$  ( $p_\alpha$  pose) and  $\phi_{\text{thr}} = 6 RT$  ( $p_\beta$  pose). The irregular drop of the derivatives for higher values of  $\phi_{\text{thr}}$  reveals a sudden depletion of sampling ultimately due to the large free energy. In fact, for the above PMF thresholds, almost all the sampled configurations of the complex contribute to  $V_I$  (99.9% and 99.1% for  $p_\alpha$  and  $p_\beta$ , respectively). These considerations lead us to choose the values of  $8 RT$  and  $6 RT$  as PMF thresholds for the  $p_\alpha$  and  $p_\beta$  poses, respectively (dashed lines in fig. 8.5). The error on  $RT \ln(C^\circ V_I)$  arising from using the above PMF thresholds, is propagated on the basis of the derivative of eq. 8.65 according to the resolution  $\Delta \phi_{\text{thr}} = RT$

$$\Delta [RT \ln(C^\circ V_I)] = RT \left| \left[ \frac{\delta \ln(C^\circ V_I)}{\delta \phi_{\text{thr}}} \right]_{\phi'_{\text{thr}}} \right| \Delta \phi_{\text{thr}}, \quad (8.66)$$

Pose	$g(1) - g(0)$	$RT \ln(C^\circ V_I)$	$\Delta G_2^\circ$	$\Delta G^\circ$
$p_\alpha$	$1826.1 \pm 0.8$	$-20.4 \pm 0.5$	$1698.1 \pm 0.1$	$-107.6 \pm 1.4$
$p_\beta$	$1775.3 \pm 1.5$	$-16.7 \pm 0.8$	$1698.1 \pm 0.1$	$-60.5 \pm 2.4$
$\Delta G_{\alpha\beta}^\circ$ (PLD)		$\Delta G_{\alpha\beta}^\circ$ (BiD-AP)		
$43.3 \pm 0.9$		$47.1 \pm 3.6$		

**Table 8.1:** ABFEs ( $\Delta G^\circ$  column) and free energy contributions ( $g(1) - g(0)$  and  $RT \ln(C^\circ V_I)$  columns; eq. 8.62) related to the  $p_\alpha$  and  $p_\beta$  poses, obtained by using the BiD-AP scheme. The contribution from desolvation free energy is shown ( $\Delta G_2^\circ$  column; eq. 8.64). A comparison between the PLD method and the BiD-AP scheme concerning  $\Delta G_{\alpha\beta}^\circ$  (difference between the free energies of the  $p_\alpha$  and  $p_\beta$  poses; see end of sec. 8.5.1) is also reported. The errors are computed as described in the text. Free energies are in  $\text{kJ mol}^{-1}$ .

where  $\phi'_{\text{thr}}$  is  $8 RT$  for  $p_\alpha$  and  $6 RT$  for  $p_\beta$ . In this way, we estimate  $RT \ln(C^\circ V_I) = -20.4 \pm 0.5$  for  $p_\alpha$  and  $-16.7 \pm 0.8 \text{ kJ mol}^{-1}$  for  $p_\beta$ .

### BiD-AP: Alchemical contribution to the ABFE

The results on  $\Delta G^\circ$  together with the single contributions  $g(1) - g(0)$ ,  $RT \ln(C^\circ V_I)$  and  $\Delta G_2^\circ$ , recovered from using the BiD-AP scheme, are reported in table 8.1. The errors on  $g(1) - g(0)$  and  $\Delta G_2^\circ$  are expressed, in turn, as the standard deviation of 1000 estimations, each being calculated from a block of 1000 work values. A single block is built by picking work samples from the original set of works, under an uniform sampling with repetition[59]. The greater error on  $g(1) - g(0)$  associated to the  $p_\beta$  pose with respect to the  $p_\alpha$  one can be ascribed to the larger spread of the PMF around the binding site in this pose, which leads to a poorer statistical sampling of the initial microstates. The error on  $RT \ln(C^\circ V_I)$  is computed as reported in sec. 8.5.2. The ABFE presents a quite small uncertainty,  $\sim 2 \text{ kJ mol}^{-1}$ , obtained by summing the errors of the three independent free energy terms. The ABFEs for the  $p_\alpha$  and  $p_\beta$  poses allow to compare the stability of the two poses relative to

one another as the difference  $\Delta G_{\alpha\beta}^{\circ} = \Delta G_{\beta}^{\circ} - \Delta G_{\alpha}^{\circ}$ , namely

$$\Delta G_{\alpha\beta}^{\circ} = [g(1) - g(0)]_{\alpha} - [g(1) - g(0)]_{\beta} + RT \ln \left( \frac{[V_I]_{\alpha}}{[V_I]_{\beta}} \right), \quad (8.67)$$

where the subscripts  $\alpha$  and  $\beta$  indicate the poses related to the quantities into square brackets. According to eq. 8.67, the error on  $\Delta G_{\alpha\beta}^{\circ}$  corresponds to the sum of the errors on  $g(1) - g(0)$  and  $RT \ln(C^{\circ}V_I)$  related to the two poses, as  $\Delta G_2^{\circ}$  does not enter  $\Delta G_{\alpha\beta}^{\circ}$ . As stated at the end of sec. 8.5.1, the  $\Delta G_{\alpha\beta}^{\circ}$  outcome from BiD-AP can be compared to that obtained from the PLD method (chapter 7). On the basis of this last equation, the error done in using the PLD approach corresponds to the sum of the errors on  $\Delta\phi_{\alpha\beta}$ ,  $RT \ln \rho(\mathbf{R}'_{L,\alpha})$  and  $RT \ln \rho(\mathbf{R}'_{L,\beta})$ . For the last two quantities, such errors hold 0.02 and 0.03 kJ mol<sup>-1</sup>, as reported in sec. 8.5.2. The error on  $\Delta\phi_{\alpha\beta}$  is computed using bootstrapping, in analogy with the procedure employed for  $g(1) - g(0)$  and  $\Delta G_2^{\circ}$  (see above, in this section). As we can infer from the data of table 8.1, upon considering the small errors arising from  $\rho(\mathbf{R}'_{L,\alpha})$  and  $\rho(\mathbf{R}'_{L,\beta})$ , the global error on  $\Delta G_{\alpha\beta}^{\circ}$  is essentially due to the calculation of  $\Delta\phi_{\alpha\beta}$ . The  $\Delta G_{\alpha\beta}^{\circ}$  values obtained with the BiD-AP and PLD methods are compared in the bottom of table 8.1. Although the two estimations differ by about 4 kJ mol<sup>-1</sup>, they are fully consistent, being within the range of uncertainty of the calculation.

### SiP-AP: Probability density contribution to the ABFE

In the SiP-AP scheme, the free energy contribution to the ABFE computed through the equilibrium simulation is  $-RT \ln(\rho(\mathbf{R}'_L)/C^{\circ})$  (eq. 8.63), from now on indicated as  $\mathcal{G}_{\rho}$ . In fig. 8.6A, we report  $\mathcal{G}_{\rho}$  against  $\phi_{\text{thr}}$ . Above  $\phi_{\text{thr}} = 3 RT$ ,  $\mathcal{G}_{\rho}$  is virtually independent on  $\phi_{\text{thr}}$ . Moreover, increasing the threshold from  $RT$  to  $3 RT$ , the change of  $\mathcal{G}_{\rho}$  does not overwhelm 2.5 kJ mol<sup>-1</sup>. This moderate dependence of  $\mathcal{G}_{\rho}$  on  $\phi_{\text{thr}}$  has to be compared with the change observed for the corresponding quantity,  $RT \ln(C^{\circ}V_I)$ , entering the BiD-AP scheme (fig. 8.5A), which is almost double. Indeed,  $\mathcal{G}_{\rho}$  is calculated from the number of configurations featured by  $\mathbf{R}_L = \mathbf{R}'_L$ , divided by the total number of configurations in the bound state. This ratio is weakly affected by an increase of  $\phi_{\text{thr}}$ , because, just a few  $RT$  above the PMF minimum, the probability of sampling bound configurations is small. Therefore, such configurations contribute marginally to  $\mathcal{N}_{\text{tot}}$  and ultimately to  $\mathcal{G}_{\rho}$ . On the contrary, the term  $RT \ln(C^{\circ}V_I)$  featuring the BiD-AP scheme accounts for the global sampling of the

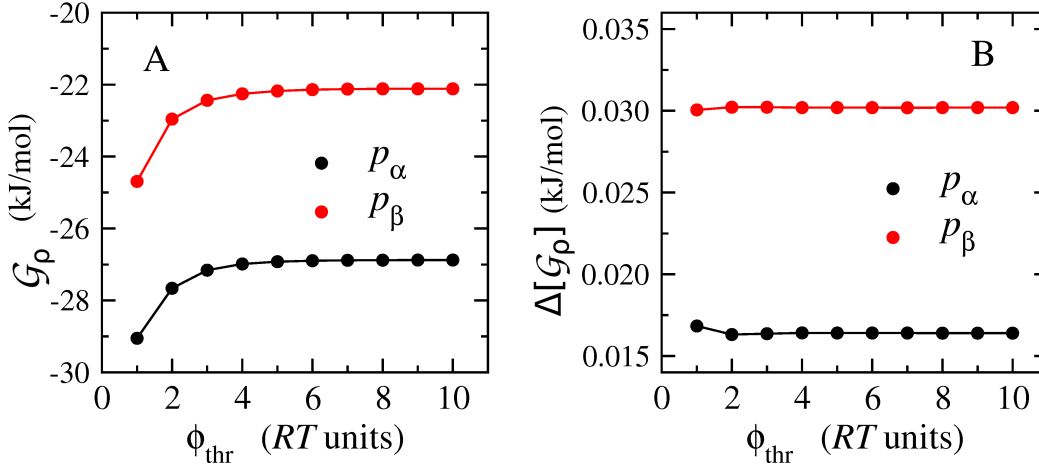


**Figure 8.6:** *Panel A.* ABFE contribution arising from  $\rho(\mathbf{R}'_L)$ , namely  $\mathcal{G}_\rho \equiv -RT \ln(\rho(\mathbf{R}'_L)/C^\circ)$ , as a function of the PMF threshold  $\phi_{\text{thr}}$ , computed for the  $p_\alpha$  and  $p_\beta$  poses (see legend). *Panel B.* Numerical error on the  $\mathcal{G}_\rho$  estimates,  $\Delta[\mathcal{G}_\rho]$ , as a function of the of the PMF threshold  $\phi_{\text{thr}}$ , computed for the  $p_\alpha$  and  $p_\beta$  poses (see legend). Lines are guides for eyes.

bound configurations, whose weight to  $V_I$  does not depend on their probability provided they are sampled at least one time. This results in a significant dependence of  $V_I$ , and hence of  $RT \ln(C^\circ V_I)$ , on configurations widespread also in high free-energy levels. Owing to the substantial invariance of  $\mathcal{G}_\rho$  on  $\phi_{\text{thr}}$ , the error associated to  $\rho(\mathbf{R}'_L)$ , denoted as  $\Delta[\rho(\mathbf{R}'_L)]$ , has been related to the uncertainty arising from sampling, rather than to that arising from the choice of the PMF threshold. In particular,  $\Delta[\rho(\mathbf{R}'_L)]$  is taken as the standard deviation of 1000 estimates of  $\rho(\mathbf{R}'_L)$  obtained by using bootstrapping[59]. Each estimate of  $\rho(\mathbf{R}'_L)$  has been obtained from a calculation made on  $1.15 \cdot 10^6$  configurations of the system picked from the original set containing a total of  $1.15 \cdot 10^6$  configurations, under an uniform sampling with repetition. Configurations featured by a PMF greater than  $\phi_{\text{thr}}$  are excluded from the calculation. The error on  $\mathcal{G}_\rho$  is related to  $\Delta[\rho(\mathbf{R}'_L)]$  through the standard propagation relationship, namely  $\Delta[\mathcal{G}_\rho] = RT \Delta[\rho(\mathbf{R}'_L)]/\rho(\mathbf{R}'_L)$ , and is plotted against  $\phi_{\text{thr}}$  in fig. 8.6B. The error is almost independent on  $\phi_{\text{thr}}$  and much lower than  $0.1 \text{ kJ mol}^{-1}$ . Taking an

Pose	$\phi(1, \mathbf{R}'_L) - \phi(0, \mathbf{R}'_L)$	$-RT \ln(\rho(\mathbf{R}'_L)/C^\circ)$	$\Delta G_2^\circ$	$\Delta G^\circ$
$p_\alpha$	$1831.9 \pm 0.2$	$-26.88 \pm 0.02$	$1698.1 \pm 0.1$	$-106.9 \pm 0.3$
$p_\beta$	$1783.2 \pm 0.2$	$-22.14 \pm 0.03$	$1698.1 \pm 0.1$	$-63.0 \pm 0.3$
$\Delta G_{\alpha\beta}^\circ$ (PLD)		$\Delta G_{\alpha\beta}^\circ$ (SiP-AP)		
$43.3 \pm 0.9$		$43.9 \pm 0.4$		

**Table 8.2:** ABFEs ( $\Delta G^\circ$  column) and free energy contributions ( $\phi(1, \mathbf{R}'_L) - \phi(0, \mathbf{R}'_L)$  and  $-RT \ln(\rho(\mathbf{R}'_L)/C^\circ)$  columns; eq. 8.63) related to the  $p_\alpha$  and  $p_\beta$  poses, obtained by using the SiP-AP scheme. The contribution from desolvation free energy is shown ( $\Delta G_2^\circ$  column; eq. 8.64). A comparison between the PLD method and the SiP-AP scheme concerning  $\Delta G_{\alpha\beta}^\circ$  (difference between the free energies of the  $p_\alpha$  and  $p_\beta$  poses; see end of sec. 8.5.1) is also reported. The errors are computed as described in the text. Free energies are in  $\text{kJ mol}^{-1}$ .

arbitrarily large value of  $\phi_{\text{thr}}$  ( $5 RT$ ), we estimate  $-RT \ln(\rho(\mathbf{R}'_L)/C^\circ) = -26.88 \pm 0.02$  and  $-22.14 \pm 0.03 \text{ kJ mol}^{-1}$  for the  $p_\alpha$  and  $p_\beta$  poses, respectively. In conclusion, we observe that the SiP-AP scheme allows for a virtual independence of the free energy contribution  $-RT \ln(\rho(\mathbf{R}'_L)/C^\circ)$  on the choice of  $\phi_{\text{thr}}$ , thus guaranteeing a better accuracy with respect to the analogous term  $RT \ln(C^\circ V_I)$  entering the BiD-AP scheme.

### SiP-AP: Alchemical contribution to the ABFE

Table 8.2 reports on  $\Delta G^\circ$  of the two poses along with the various free energy contributions evaluated according to the SiP-AP methodology (eq. 8.63). It is important to remark that in using SiP-AP, contrarily to BiD-AP, the bidirectional nonequilibrium approach has been exploited to compute  $\phi(1, \mathbf{R}'_L) - \phi(0, \mathbf{R}'_L)$ . As proved in early studies[137, 177], combining the two directions of a nonequilibrium process allows to improve the accuracy of free energy estimates. The error on  $\phi(1, \mathbf{R}'_L) - \phi(0, \mathbf{R}'_L)$  is computed using bootstrapping as done for  $g(1) - g(0)$  in the BiD-AP approach, while for  $-RT \ln(\rho(\mathbf{R}'_L)/C^\circ)$  it is reported in sec 8.5.2. Comparing the errors on the alchemical free energy contributions entering the SiP-AP and BiD-AP schemes,  $\phi(1, \mathbf{R}'_L) - \phi(0, \mathbf{R}'_L)$  and  $g(1) - g(0)$  respectively, we note an important

difference, being the latter four times larger, or more. The origin of this difference can be ascribed, at the first instance, by the fact that in SiP-AP bidirectionality of the process has been applied, whereas a monodirectional calculation has been performed with BiD-AP. In the second instance, we have to consider that in SiP-AP a stiff restraining potential is enforced to L when sampling the initial microstates for alchemical trajectories, while in BiD-AP these microstates are sampled without constraints in place. Thus, in using the SiP-AP scheme, the phase-space region to be sampled for producing the initial microstates is significantly reduced, ultimately providing a better sampling of such microstates. The error on  $\Delta G^\circ$ , computed as the sum of the three free energy contributions, is around  $0.3 \text{ kJ mol}^{-1}$  for both poses. The values of  $\Delta G^\circ$  obtained for the two poses from using BiD-AP and SiP-AP schemes are in very good agreement being their differences ( $0.7$  and  $2.5 \text{ kJ mol}^{-1}$  for the  $p_\alpha$  and  $p_\beta$  poses, respectively) within the corresponding error bars ( $1.7$  and  $2.7 \text{ kJ mol}^{-1}$ ). In the bottom of table 8.2, we compare the free energy difference  $\Delta G_{\alpha\beta}^\circ$  computed by using the PLD method and the SiP-AP scheme. The latter is calculated in analogy with eq. 8.67. Also in this case, the error on  $\Delta G_2^\circ$  does not matter, being  $\Delta G_{\alpha\beta}^\circ$  obtained from a sum involving only the quantities  $\phi(1, \mathbf{R}'_L) - \phi(0, \mathbf{R}'_L)$  and  $-RT \ln(\rho(\mathbf{R}'_L)/C^\circ)$  related to the  $p_\alpha$  and  $p_\beta$  poses. The agreement is very satisfactory, thus providing a sound numerical support to our methodology. Concerning  $\Delta G_{\alpha\beta}^\circ$ , the best agreement between the PLD method and the SiP-AP scheme, compared to BiD-AP, may again be ascribed to the improved accuracy arising from exploiting the bidirectionality of the process.

## 8.6 $\beta$ -cyclodextrin with aromatic compounds

### 8.6.1 Computational details

For the  $\beta$ -CD·benz and  $\beta$ -CD·naph complexes in water solution, ABFEs have been computed using only the SiP-AP scheme, while the geometrical parameter considered to identify bound configurations of the complex is the distance between the centers of mass of the aromatic compound (ligand) and  $\beta$ -CD (receptor). The relationships at the basis of this approach are given in sec. 8.3.1 and discussed in detail in ref. [83]. All simulations were performed with the general setup also employed for the Zn(II)·anion system (sec. 8.5.1), apart from temperature, which is 298 K. The GLYCAM06 force field[117] is used for the



$\beta$ -CD, combined with an atomic charge distribution obtained through a RESP fit[15] at the B3LYP/6-31G(d) level[16, 123]. Benzene and naphthalene are modeled through the ff99sb force field[101], with the atomic charges being evaluated as for  $\beta$ -CD. The initial structure of the  $\beta$ -CD·benz complex is taken from the 2Y4S PDB file[196], while the  $\beta$ -CD·naph complex was built by dragging naphthalene into the  $\beta$ -CD cavity through a molecular modelling program[96]. To avoid large stress in the initial configurations of the complexes, a few steps of structural optimization have been carried out. Then, 922 water molecules have been added as a cubic box, taking care of avoiding interatomic overlap. As stated above, the coordinate considered to identify the position of L relative to R is the distance  $r$  between the centers of mass of R and L. For the  $\beta$ -CD·naph system, the calculation of the probability density  $\rho(r)$ [10] needed to determine the reference distance  $r'$  and hence the  $\rho(r')$  free energy contribution to the ABFE (eq. 8.61), has been realized through an equilibrium simulation of the solvated complex lasting 30 ns. Like the Zn(II)·anion case, owing to tight binding between R and L, no restraints have been necessary. In fact, the RL complex did not dissociate during the whole duration of the simulation. Instead, in the simulation of the  $\beta$ -CD·benz complex, dissociation was observed after a few hundred ps, suggesting for a low affinity between the two moieties. Thus, in order to keep the complex in the bound state, as required for the calculation of  $\rho(r')$ , an umbrella sampling simulation[188] of 30 ns has been carried out by applying a restraining potential  $U_{\text{us}}(r) = k_{\text{us}}r^2$  on the coordinate  $r$ , with a force constant  $k_{\text{us}}$  of  $0.2 \text{ kcal mol}^{-1} \text{ \AA}^{-2}$ . The proper reweighting procedure for umbrella sampling[188] has been applied to compute  $\rho(r)$ . The PMF as a function of  $r$ , computed as  $\phi(r) = -RT \ln \rho(r)$ , is reported in fig. 8.7A for both systems. The chosen reference distance  $r'$  is  $1 \text{ \AA}$ , even if the minimum value of  $\phi(r)$  falls at  $r = 0 \text{ \AA}$ . In fact, it is mandatory that good sampling is achieved for  $r = r'$  configurations, namely that the sampling probability at  $r'$ , defined as  $\delta p(r') = 4\pi r'^2 \rho(r') \delta r$ , is not negligible. This is indeed obtained at a good extent for  $r' = 1 \text{ \AA}$ , as inferred by inspecting fig. 8.7B, where the probability  $\delta p(r)$  is reported. In this respect, we note that  $\delta p(r)$  for  $r = 0 \text{ \AA}$  is negligible owing to the small volume element  $4\pi r^2 \delta r$ . Since, in using the SiP-AP scheme, the calculation of  $\rho(r')$  resulted substantially insensitive to the boundaries of the binding site[11], all configurations sampled during the equilibrium simulations have been included in the calculation of  $\rho(r')$ . Evaluation of  $\phi(1, r') - \phi(0, r')$  (eq. 8.61) has been done through nonequilibrium simulations during which the ligand, benzene or naphthalene, has been decoupled from the rest of the

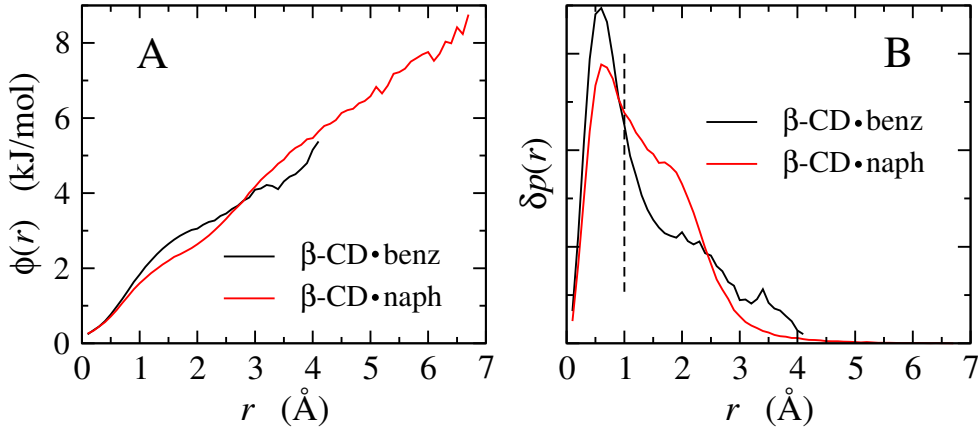


**Figure 8.7:** *Panel A.* PMF as a function of the distance  $r$  between the centers of mass of ligand and receptor for the  $\beta$ -CD•benz and  $\beta$ -CD•naph systems. *Panel B.* Probability  $\delta p(r)$  (cf. eq. 8.60) as a function of the distance  $r$  for the  $\beta$ -CD•benz and  $\beta$ -CD•naph systems. The dashed line marks the chosen reference distance  $r'$ .

system, namely  $\beta$ -CD and solvent. The initial microstates have been sampled from an equilibrium simulation of the fully coupled system, enforcing a stiff harmonic restraint of the type  $U_{\text{res}}(r) = k(r - r')^2$ . The equilibrium distance is clearly  $r' = 1 \text{ \AA}$ , while the force constant  $k$  is  $1000 \text{ kcal mol}^{-1} \text{ \AA}^{-2}$ . For both systems, 1000 microstates have been stored at regular time intervals of 0.6 ps, after an equilibration phase of 0.6 ns. Nonequilibrium alchemical trajectories have been realized in analogous way to the Zn(II)•anion case. During each trajectory, the interaction potential of L with the rest of the system is externally modulated under an established linear protocol of  $\lambda$ , leading the system from the coupled to the uncoupled state, while leaving in place the restraining potential  $U_{\text{res}}(r)$ . In particular, all nonequilibrium alchemical trajectories have been realized by switching off the electrostatic interactions in the first half of the run, *i.e.* from 0 to  $\tau/2$ , while the Lennard-Jones interactions have been switched off in the second half of the run, *i.e.* from  $\tau/2$  to  $\tau$ . The functional form of the switched interaction potential is in accord to ref. [156]. Alchemical trajectories with different durations have been carried out:  $\tau = 30, 60, 120, 240, 540$  ps. To calculate  $\Delta G_2^\circ$ , alchemical transformations of the only decoupling process have been realized. Initial microstates are

sampled from an equilibrium simulation of L (benzene or naphthalene) in aqueous solution, without enforcing any restraint to L. A total of 1000 microstates were stored every 0.6 ps. The functional form of the switched interaction potential, as well as the time schedule for  $\lambda$ , are equal to those applied in the SiP-AP alchemical trajectories described above. Three series of alchemical trajectories have been carried out using, in turn, a time  $\tau$  of 30, 240 and 540 ps. The calculation of the decoupling free energies, namely  $\phi(1, r') - \phi(0, r')$  and  $\Delta G_2^\circ$ , has been done exploiting the JE[106]. Like for the Zn(II)-anion system, the symmetry numbers of  $\beta$ -CD and aromatic compounds do not change upon changing phase or association state. Moreover, we can disregard the volumes  $\bar{V}_L$ ,  $\bar{V}_R$  and  $\bar{V}_{RL}$ , because NPT equations of motion are employed. This allows to use simplified equations, analogous to eqs. 8.63 and 8.64, to evaluate  $\Delta G_1^\circ$  and  $\Delta G_2^\circ$ .

## 8.6.2 Results

### SiP-AP: Probability density contribution to the ABFE

In this section, we report on the contribution to the ABFE arising from the probability density computed at  $r'$ , expressed as  $-RT \ln(\rho(r')/C^\circ) \equiv \mathcal{G}_\rho$  (eq. 8.61). The probability density has been computed from eq. 8.60 by setting  $\delta r = 0.1 \text{ \AA}$ . We have verified that the error on  $\mathcal{G}_\rho$  due to the use of a not infinitesimal  $\delta r$  is negligible, being almost constant when  $\delta r$  ranges from 0.2 to 0.005  $\text{\AA}$ . The calculation of  $\mathcal{G}_\rho$  has been made by averaging 15 independent estimates, obtained dividing the whole simulation run into chunks of 2 ns each. In this case, the error has been evaluated as the standard deviation of the independent estimations. In table 8.3, we report the estimates of  $\mathcal{G}_\rho$  along with the related errors for the  $\beta$ -CD-benz and  $\beta$ -CD-naph systems. The calculation realized with using the whole set of configurations of the complex (simulations lasting 30 ns) provides almost coincident values, being -10.14 and -10.27  $\text{kJ mol}^{-1}$  for  $\beta$ -CD-benz and  $\beta$ -CD-naph, respectively.

### SiP-AP: Alchemical contribution to the ABFE

The free energy term  $\Delta\phi \equiv \phi(1, r') - \phi(0, r')$  has been computed by means of the bootstrapping technique. In particular,  $10^4$  blocks have been built, each consisting of 200 work values randomly picked from those achieved from the 1000 alchemical trajectories (uniform sampling with repetition is used). The JE has been applied on each block of data, obtaining

	$\beta$ -CD·benz	$\beta$ -CD·naph
$\mathcal{G}_\rho$	$-10.3 \pm 1.2$	$-10.2 \pm 0.5$
$\Delta\phi$ (30)	$34.9 \pm 3.5$	$51.2 \pm 3.7$
$\Delta\phi$ (60)	$29.3 \pm 3.4$	$45.7 \pm 3.0$
$\Delta\phi$ (120)	$26.9 \pm 1.8$	$41.8 \pm 1.8$
$\Delta\phi$ (240)	$23.6 \pm 1.8$	$37.7 \pm 1.8$
$\Delta\phi$ (540)	$22.5 \pm 1.9$	$36.0 \pm 1.0$
$\Delta G_2^\circ$ (30)	$3.2 \pm 1.6$	$9.4 \pm 2.4$
$\Delta G_2^\circ$ (240)	$1.7 \pm 0.2$	$7.1 \pm 0.4$
$\Delta G_2^\circ$ (540)	$1.8 \pm 0.1$	$7.1 \pm 0.2$

**Table 8.3:** Single free energy contributions to the ABFE for the  $\beta$ -CD·benz and  $\beta$ -CD·naph systems, obtained by using the SiP-AP scheme. The contribution dependent on  $\rho(r')$  is  $\mathcal{G}_\rho \equiv -RT \ln(\rho(r')/C^\circ)$ . The contributions calculated alchemically are  $\Delta\phi \equiv \phi(1, r') - \phi(0, r')$  (eq. 8.61) and  $\Delta G_2^\circ$  (eq. 8.51). Simplified forms of eqs. 8.61 and 8.51 are used upon considering that changes of symmetry numbers do not occur and partial molar volumes of the solutes at infinite dilution can be disregarded, since NPT simulations are carried out. Various series of alchemical calculations have been performed differing in the simulation time (reported in parenthesis in ps units). The errors are computed as described in the text. Free energies are in  $\text{kJ mol}^{-1}$ .

the corresponding free energy estimate. Such estimates are then averaged to evaluate the  $\Delta\phi$  value reported in table 8.3. The error, also reported in the table, has been determined

$\Delta G^\circ$	$\beta$ -CD·benz	ref.	$\beta$ -CD·naph	ref.
Present Calc.	$-10.4 \pm 3.2$		$-18.7 \pm 1.7$	
Exp.	$-12.7 \pm 0.2^d$	[190]	$-14.8 \pm 0.3^a$	[62]
	$-11.0$	[189]	$-16.2 \pm 0.2^b$	[92]
	$-13.0 \pm 0.1^e$	[91]	$-15.9$	[76]
	$-11.9 \pm 0.2^f$	[165]	$-16.0 \pm 0.2^c$	[72]
Previous Calc.	$-2.1$	[160]	$-25.76$	[76]
	$-12.1$	[40]	$-12.0 \pm 0.6$	[47]
	$-11.1$	[61]		
	$-15.4 \pm 0.3$	[201]		

**Table 8.4:** ABFEs of  $\beta$ -CD·benz and  $\beta$ -CD·naph computed with the SiP-AP scheme. Comparison with early experimental and computational studies is shown. In the following References, the binding constant,  $K$ , is given together with the related error,  $\delta K$ . For the sake of comparison with our outcomes,  $K$  has been converted into ABFE (eq. 8.4). The error has also been converted through the propagation formula  $\delta\Delta G^\circ = RTK^{-1}\delta K$ . <sup>a</sup> ref. [62]:  $K = 377 \pm 35 \text{ M}^{-1}$ . <sup>b</sup> ref. [92]:  $K = 678 \pm 41 \text{ M}^{-1}$ . <sup>c</sup> ref. [72]:  $K = 630 \pm 40 \text{ M}^{-1}$ . <sup>d</sup> ref. [190]:  $K = 169 \pm 11 \text{ M}^{-1}$ . <sup>e</sup> ref. [91]:  $K = 194 \pm 9 \text{ M}^{-1}$ . <sup>f</sup> ref. [165]:  $K = 120 \pm 10 \text{ M}^{-1}$ . Free energies are in  $\text{kJ mol}^{-1}$ .

as the standard deviation of the  $10^4$  estimates. Increasing the simulation time  $\tau$ , the free energy estimates decrease. This is indeed an expected result, as it is known that the JE systematically overestimates the free energy difference, owing to the statistical nature of exponential averages[88]. Convergence is obtained as long as slower nonequilibrium simulations are performed. In table 8.3, we can however observe that convergence seems to be almost reached in simulations lasting 540 ps. Nonetheless, the estimates of  $\Delta\phi$  for  $\tau = 240$  ps still appear a good achievement, differing only by less than  $2 \text{ kJ mol}^{-1}$  from those obtained using  $\tau = 540$  ps. The third contribution to the ABFE, namely the desolvation free energy  $\Delta G_2^\circ$ , is also reported in table 8.3 together with the associated errors. The procedure used

for evaluating  $\Delta G_2^{\circ}$  and the related error is that employed for  $\Delta\phi$ . Achievement of convergence is even more evident than for the  $\Delta\phi$  case, being the free energy estimates obtained from alchemical trajectories of 240 and 540 ps coincident, with errors smaller than  $0.5 \text{ kJ mol}^{-1}$ . The three contributions to the ABFE summarized in table 8.3 have been recasted via eq. 8.18 to obtain the ABFEs shown in table 8.4. The estimates reported in the table are computed from the most accurate data, namely those obtained from the longest alchemical trajectories (540 ps). The errors are evaluated standardly as the sum of the errors on the single free energy contributions. Early data from experimental and computational studies are also reported in table 8.4 for comparison. With respect to experimental results, our ABFE estimates for  $\beta$ -CD·benz and  $\beta$ -CD·naph appear slightly underestimated and overestimated, respectively, though the experimental data present a large spread. Nonetheless, the agreement is very good, being the deviations well below  $4 \text{ kJ mol}^{-1}$  in both cases. To the best of our knowledge, no ABFE calculations realized by means of alchemical transformations have been reported on the  $\beta$ -CD·benz and  $\beta$ -CD·naph complexes. Two studies were instead published on  $\beta$ -CD·benz[160] and  $\beta$ -CD·naph[47] complexes using full-atomistic MD simulations, with ABFE calculation based on the integration of the PMF expressed in terms of coordinates of extrusion of the ligand from the receptor. The PMF was determined through umbrella sampling simulations[188]. The ABFEs obtained for  $\beta$ -CD·benz and  $\beta$ -CD·naph in the mentioned studies are  $-2.1$  and  $-12.0 \text{ kJ mol}^{-1}$ , respectively. Considering the experimental outcomes for  $\beta$ -CD·benz[91, 165, 189, 190] and  $\beta$ -CD·naph[62, 72, 76, 92] (see table 8.4), these results seem worse than ours. However, a strict comparison of the employed computational techniques is improper in these cases, because of the different force fields adopted. Another simulation study[201] using the binding energy distribution analysis method with implicit solvation has been reported on ABFEs of several  $\beta$ -CD host-guest systems, including the  $\beta$ -CD·benz complex. The deviation of the estimated ABFE,  $-15.4 \pm 0.3 \text{ kJ mol}^{-1}$ , from the experimental data is quite small and comparable with our outcomes. Other theoretical studies on  $\beta$ -CD·benz have been reported exploiting quantitative structure-property relationships[61] (QSPR) and harmonic approximation/mode scanning method[40], with results comparable in accuracy to ours. For  $\beta$ -CD·naph, ABFE was estimated theoretically via automated semi-rigid docking[76], with results worse than ours.

## 8.7 Conclusions

The fast-switching decoupling method is a powerful technique to compute absolute binding free energies of ligand-receptor (RL) complexes. In the current implementations, fast-switching decoupling is applied without constraining the RL complex in the bound state[153]. Even if this has been revealed computationally effective[141, 164], a sound theoretical ground requires that the bound state of the complex is preserved during decoupling of the ligand from receptor and solvent. Here, we have addressed this issue supplementing the method with the possibility of performing alchemical trajectories with the ligand constrained to a fixed position relative to the receptor. Binded-domain alchemical-path (BiD-AP) and single-point alchemical-path (SiP-AP) schemes allow to compute the decoupling free energy contribution to the absolute binding free energy without resorting to the explicit calculation of the orientational binding-site volume[80]. With respect to fast-switching decoupling without constraints[153], BiD-AP prevents the ligand from leaving the binding site, but still requires an estimate of the positional binding-site volume. SiP-AP is an evolution of BiD-AP, in which a reference configuration of the RL complex is introduced to split the decoupling free energy of the ligand from solvent and receptor into two separate terms, one computed from an equilibrium MD simulation of the fully-coupled bound state of the complex and the other from nonequilibrium alchemical transformations of the complex constrained in the reference configuration. The improvement with respect to the BiD-AP scheme is that the SiP-AP scheme allows to avoid the calculation of the positional binding-site volume. BiD-AP and SiP-AP techniques are based on a binding descriptor corresponding to the position of a reference atom of the ligand with respect to a given atom of the receptor. As shown, the two schemes can also be devised to employ the simple distance between the two atoms as binding descriptor. The drawback of such an approach is that one has to assume that complete orientational sampling of the ligand is attained during the equilibrium MD simulations of the bound RL complex, whether in the MD simulation performed to get the initial microstates of the alchemical trajectories or, in the case of the SiP-AP scheme, in the one aimed at computing  $\rho(\mathbf{R}'_L)$ . The fact that alternative orientational poses are possible for a complex, with comparable binding affinity, could introduce important errors in the methodology. Nonetheless, this type of problem is common to almost all the double-decoupling based methods. In such cases, one must introduce an a priori knowledge of possible poses of

the ligand or to resort to some advanced sampling technique based, for example, on replica exchange or serial generalized ensemble schemes[27, 132, 146, 156, 183, 184]. BiD-AP and SiP-AP respectively derive from CDTS and PLD schemes, developed in chapters 5 and 7. The main difference stems from the number of calculations needed to recover the ABFE of a ligand-receptor complex. In BiD-AP, two types of calculation are required. One consists of an equilibrium simulation aimed at storing the initial microstates for alchemical trajectories and, at the same time, at computing the binding-site volume entering the ABFE. The second consists of a batch of alchemical trajectories with constrained dynamics, to estimate the decoupling free energy contribution to the ABFE. The SiP-AP technique, in addition to the batch of alchemical trajectories like BiD-AP, requires to perform two equilibrium simulations, one to determine the probability density as a function of the ligand position relative to the receptor and the other, implemented with constrained dynamics of the ligand, to store the initial microstates for alchemical trajectories. However, as shown in our numerical tests on the Zn(II)-anion system, the extra computational effort required by SiP-AP leads to a relevant enhancement of accuracy. This is basically due to the fact that the free energy contribution related to the probability density weakly depends on the sampling of the binding-site region, provided that the most important points are explored. In contrast, the analogous contribution in BiD-AP is based on the evaluation of the binding-site volume, a quantity which can strongly depend on the quality of the sampling of the binding-site region. Although in the present study we do not take particular care to the optimization of the methodology, we envisage some aspects that can enhance the degree of efficiency of fast-switching alchemical simulations with constrained dynamics. In the first instance, we notice the possibility of implementing fast-switching alchemical simulations in a bidirectional fashion, namely by combining two batches of alchemical trajectories related, in turn, to the coupling and decoupling processes. Combining forward and backward nonequilibrium simulations driven by an external control parameter is a well-known approach[174], which has been shown to improve significantly the accuracy of free energy estimates with respect to the monodirectional technique[25, 35, 137, 159, 177] (the latter being based on only one, forward or backward, process). As a matter of fact, the bidirectional strategy has already been applied in the framework of nonequilibrium alchemical transformations to compute the water to methane relative hydration free energy[143]. Furthermore, also in this study, coupling and decoupling trajectories have been combined to compute the ABFE of the Zn(II)-anion com-



plex by using SiP-AP. Another improvement of the method could be gained from applying a nonequilibrium simulation technique based on the breaking of highly dissipative alchemical trajectories before their normal end. This method, called path-breaking[29, 86], is extremely general for nonequilibrium simulations, and can be implemented in both monodirectional and bidirectional alchemical approaches. Finally, some methodology inspired to QM/MM simulations[171] developed in the framework of nonequilibrium simulations, such as dynamical freezing[81, 142] or configurational freezing[27, 143] could somehow be integrated in the alchemical machinery to decrease further the dissipation and hence to improve the accuracy. Nothing prevents, in principle, from combining the methodologies described above in a unique nonequilibrium alchemical protocol.



---

## Bibliography

---

- [1] In fact, also thermodynamic variables, such as temperature or pressure, can be considered.
- [2] Here and in the following, the term “microstate” is used to indicate the phase-space configuration  $\mathbf{\Gamma} = \{\mathbf{r}, \mathbf{p}, V, \mathbf{s}, \mathbf{h}\}$  of the system.
- [3] A slightly different definition of Heaviside step function is used:  $\theta(x) = 0$  for  $x < 0$  and  $\theta(x) = 1$  for  $x \geq 0$ .
- [4] The dimensionless work  $\mathcal{W}$  has been computed with Eq. 6.17. The dimensionless free energy  $\Delta\mathcal{G}$  for the high energy-barrier system is  $-2422.90 \pm 0.01$ .
- [5] Each component of  $\zeta(\mathbf{x})$  depends on the Cartesian coordinates of four atoms. However, to simplify the notation, here we take the general dependence on the coordinates  $\mathbf{x}$  of all the atoms.
- [6] From now on, the symbol  $\beta/\alpha_{\text{R}}$  will be used to refer to  $\beta$  or  $\alpha_{\text{R}}$  conformations indifferently.
- [7] The total SGE simulation time  $\tau_{\text{sge}}$  is the sum of the times related to all replicas.

## BIBLIOGRAPHY

---

- [8] The potential of mean force of L (Eq. 8.30) is independent of  $\mathbf{R}_L$  when L is decoupled from the rest of the system ( $\lambda = 1$ ); combine Eqs. 8.24 and 8.30.
- [9] With respect to Eq. 7.13, the energy takes the form  $U(\lambda, \mathbf{r}_L, \mathbf{r}_S)$ , that is it does not include the coordinates of R and is independent on the external coordinates of L.
- [10] If not specified otherwise,  $\rho(r)$  denotes the probability density of the fully coupled system.
- [11] This has been verified through numerical tests based on a free-energy threshold protocol, as reported for the Zn|anion system.
- [12] M.P. Allen and D.J.Tildesley. *Computer simulations of liquids*. Clarendon Press, Oxford, 1987.
- [13] H. C. Andersen. *J. Comput. Phys.*, 52:24–34, 1983.
- [14] P. Atkins and J. de Paula. *Physical Chemistry Seventh Edition*. Oxford University Press, 2002.
- [15] C. I. Bayly, P. Cieplak, W. D. Cornell, and P. A. Kollman. *J. Phys. Chem.*, 97:10269–10280, 1993.
- [16] A. D. Becke. *Phys. Rev. A*, 33:3098–3100, 1988.
- [17] A. Ben-Naim. *Statistical Thermodynamics for Chemists and Biochemists*. Plenum Press, New York, p. 677, 1992.
- [18] H. Bennett. *J. Comput. Phys.*, 22:245, 1976.
- [19] A. Bertin, M. Poli, and A. Vitale. *Fondamenti di termodinamica*. Progetto Leonardo, 1997.
- [20] S. Boresch, F. Tettinger, M. Leitgeb, and M. Karplus. *J. Phys. Chem. B*, 107:9535–9551, 2003.
- [21] Charles L. Brooks and David A. Case. *Chem. Rev.*, 93:2487 – 2502, 1993.
- [22] M. Campisi, P. Talkner, and P. Hänggi. *Phys. Rev. Lett.*, 102:210401, 2009.

## BIBLIOGRAPHY

---

- [23] D. Chandler. *Introduction to modern statistical mechanics*. Oxford University Press, 1987.
- [24] D. Chandler and L. R. Pratt. *J. Chem. Phys.*, 65:2925–2940, 1976.
- [25] R. Chelli. *J. Chem. Phys.*, 130:054102, 2009.
- [26] R. Chelli. *J. Chem. Phys.*, 130:054102, 2009.
- [27] R. Chelli. *J. Chem. Theory Comput.*, 8:4040–4052, 2012.
- [28] R. Chelli. *J. Chem. Theory Comput.*, 8:4040–4052, 2012.
- [29] R. Chelli, C. Gellini, G. Pietrapertusa, E. Giovannelli, and G. Cardini. *J. Chem. Phys.*, 38:214109, 2013.
- [30] R. Chelli, S. Marsili, A. Barducci, and P. Procacci. *Phys. Rev. E*, 75(050101(R)), 2007.
- [31] R. Chelli, S. Marsili, A. Barducci, and P. Procacci. *J. Chem. Phys.*, 127(034110), 2007.
- [32] R. Chelli, S. Marsili, A. Barducci, and P. Procacci. *Phys. Rev. E*, 75:050101, 2007.
- [33] R. Chelli, S. Marsili, A. Barducci, and P. Procacci. *J. Chem. Phys.*, 127:034110, 2007.
- [34] R. Chelli, S. Marsili, A. Barducci, and P. Procacci. *Phys. Rev. E*, 75:050101, 2007.
- [35] R. Chelli, S. Marsili, and P. Procacci. *Phys. Rev. E*, 77:031104, 2008.
- [36] R. Chelli and P. Procacci. *Phys. Chem. Chem. Phys.*, 11:1152–1158, 2009.
- [37] R. Chelli and P. Procacci. *Phys. Chem. Chem. Phys.*, 11:1152, 2009.
- [38] R. Chelli and G. F. Signorini. *J. Chem. Theory Comput.*, 8:830–842, 2012.
- [39] R. Chelli and G. F. Signorini. *J. Chem. Theory Comput.*, 8:2552, 2012.
- [40] W. Chen, C.-E. Chang, and M. K. Gilson. *biophys. J.*, 87:3035–3049, 2004.
- [41] C. Chipot and A. Pohorille, editors. *Free Energy Calculations: Theory and Applications in Chemistry and Biology*, volume 86. Springer, Berlin, 2007.

## BIBLIOGRAPHY

---

- [42] J. D. Chodera, D. L. Mobley, M. R. Shirts, R. W. Dixon, K. Branson, and V. S. Pande. *Curr. Opin. Struct. Biol.*, 21:150–160, 2011.
- [43] D. Cohen and Y. Imry. *Phys. Rev. E*, 86:011111, 2012.
- [44] F. Colizzi, R. Perozzo, L. Scapozza, M. Recanatini, and A. Cavalli. *J. Am. Chem. Soc.*, 132:7361–7371, 2010.
- [45] D. Collin, F. Ritort, C. Jarzynski, S. B. Smith, I. Tinoco, and C. Bustamante. *Nature*, 437:231, 2005.
- [46] B. P. Cossins, S. Foucher, C. M. Edge, and J. W. Essex. *J. Phys. Chem. B*, 113:5508, 2009.
- [47] T. F. G. G. Cova, S. C. C. Nunes, and A. A. C. C. Pais. *Phys. Chem. Chem. Phys.*, 19:5209–5221, 2017.
- [48] G. E. Crooks. *J. Stat. Phys.*, 90:1481, 1998.
- [49] G. E. Crooks. *Phys. Rev. E*, 60:2721–2726, 1999.
- [50] G. E. Crooks. *Phys. Rev. E*, 61:2361, 2000.
- [51] M. A. Cuendet. *J. Chem. Phys.*, 125:144109, 2006.
- [52] Y. Deng and B. Roux. *J. Chem. Theory Comput.*, 2:1255–1273, 2006.
- [53] Y. Deng and B. Roux. *J. Phys. Chem. B*, 113:2234–2246, 2009.
- [54] T. N. Do, P. Carloni, G. Varani, and G. Bussi. *J. Chem. Theory Comput.*, 9:1720–1730, 2013.
- [55] F. Douarche, S. Ciliberto, and A. Petrosyan. *J. Stat. Mech.*, page P09011, 2005.
- [56] F. Douarche, S. Joubaud, N. B. Garnier, A. Petrosyan, and S. Ciliberto. *Phys. Rev. Lett.*, 97:140603, 2006.
- [57] Y. Duan, C. Wu, S. Chowdhury, M. C. Lee, G. M. Xiong, W. Zhang, R. Yang, P. Cieplak, R. Luo, T. Lee, J. Caldwell, J. M. Wang, and P. Kollman. *J. Comput. Chem.*, 24:1999, 2003.

## BIBLIOGRAPHY

---

- [58] M. Lapelosa E. Gallicchio and R. M. Levy. *J. Chem. Theory Comput.*, 6:2961–2977, 2010.
- [59] B. Efron and R. J. Tibshirani. Chapman and Hall, Boca Raton, FL, 1993.
- [60] U. Essmann, M. L. Perera, M. L. Berkovitz, T. Darden, H. Lee, and G. L Pedersen. *J. Chem. Phys.*, 103:8577, 1995.
- [61] E. Estrada, I. Perdomo-López, and J. J. Torres-Labandeira. *J. Chem. Inf. Comput. Sci.*, 41:1561–1568, 2001.
- [62] C. H. Evans, M. Partyka, and J. van Stam. *J. Incl. Phenom. Macrocycl. Chem.*, 38:381–396, 2000.
- [63] D. J. Evans and D. J. Searles. *Phys. Rev. E*, 50:1645, 1994.
- [64] D. J. Evans and D. J. Searles. *Phys. Rev. E*, 52:5839, 1995.
- [65] D. J. Evans and D. J. Searles. *Phys. Rev. E*, 53:5808, 1996.
- [66] M. Fasnacht, R. H. Swendsen, and J. M. Rosenberg. *Phys. Rev. E*, 69:056704, 2004.
- [67] M. Feig. *J. Chem. Theory Comput.*, 4:1555–1564, 2008.
- [68] E. H. Feng and G. E. Crooks. *Phys. Rev. E*, 79:012104, 2009.
- [69] D. Frenkel and B. Smit. *Understanding Molecular Simulations: From Algorithms to Applications*. Academic Press, San Diego, California, 2002.
- [70] D. Frezzato. *Chem. Phys. Lett.*, 533:106–113, 2012.
- [71] M. J. Frisch, G. W. Trucks, H. B. Schlegel, G. E. Scuseria, M. A. Robb, J. R. Cheeseman, G. Scalmani, V. Barone, B. Mennucci, G. A. Petersson, H. Nakatsuji, M. Caricato, X. Li, H. P. Hratchian, A. F. Izmaylov, J. Bloino, G. Zheng, J. L. Sonnenberg, M. Hada, M. Ehara, K. Toyota, R. Fukuda, J. Hasegawa, M. Ishida, T. Nakajima, Y. Honda, O. Kitao, H. Nakai, T. Vreven, J. A. Montgomery Jr., J. E. Peralta, F. Ogliaro, M. Bearpark, J. J. Heyd, E. Brothers, K. N. Kudin, V. N. Staroverov, T. Keith, R. Kobayashi, J. Normand, K. Raghavachari, A. Rendell, J. C. Burant, S. S.

## BIBLIOGRAPHY

---

- Iyengar, J. Tomasi, M. Cossi, N. Rega, J. M. Millam, M. Klene, J. E. Knox, J.B. Cross, V. Bakken, C. Adamo, J. Jaramillo, R. Gomperts, R. E. Stratmann, O. Yazyev, A. J. Austin, R. Cammi, C. Pomelli, J. W. Ochterski, R. L. Martin, K. Morokuma, V. G. Zakrzewski, G. A. Voth, P. Salvador, J. J. Dannenberg, S. Dapprich, A. D. Daniels, O. Farkas, J. B. Foresman, J. V. Ortiz, J. Cioslowski, and D. J. Fox. Gaussian Inc., Wallingford CT, 2010.
- [72] M. Fujiki, T. Deguchi, and I. Sanemasa. *Bull. Chem. Soc. Jpn.*, 61:1163–1167, 1988.
- [73] G. Gallavotti and E. G. D. Cohen. *Phys. Rev. Lett.*, 74:2694, 1995.
- [74] G. Gallavotti and E. G. D. Cohen. *J. Stat. Phys.*, 80:931, 1995.
- [75] E. Gallicchio and R. M. Levy. *Curr. Opin. Struct. Biol.*, 21:161–166, 2011.
- [76] Í. X. García-Zubiri, G. González-Gaitano, and J. R. Isasi. *J. Incl. Phenom. and Macrocycl. Chem.*, 57:265–270, 2007.
- [77] N. Garnier and S. Ciliberto. *Phys. Rev. E*, 71:060101(R), 2005.
- [78] I. J. General and H. Meirovitch. *J. Chem. Theory Comput.*, 9:4609–4619, 2013.
- [79] G. Hummer and A. Szabo. *PNAS*, 98:3657–3661, 2001.
- [80] M. K. Gilson, J. A. Given, B. L. Bush, and J. A. McCammon. *Biophys. J.*, 72:1047–1069, 1997.
- [81] E. Giovannelli, G. Cardini, and R. Chelli. *J. Chem. Theory Comput.*, 12:1029–1039, 2016.
- [82] E. Giovannelli, G. Cardini, C. Gellini, G. Pietraperzia, and R. Chelli. *J. Chem. Theory Comput.*, 11:3561–3571, 2015.
- [83] E. Giovannelli, M. Cioni, P. Procacci, G. Cardini, M. Pagliai, V. Volkov, and R. Chelli. *journal*, volume:pages, year.
- [84] E. Giovannelli, C. Gellini, G. Pietraperzia, G. Cardini, and R. Chelli. *J. Chem. Phys.*, 140:064104, 2014.



## BIBLIOGRAPHY

---

- [85] E. Giovannelli, C. Gellini, G. Pietraperzia, G. Cardini, and R. Chelli. *J. Chem. Theory Comput.*, 10:4273–4283, 2014.
- [86] E. Giovannelli, C. Gellini, G. Pietraperzia, G. Cardini, and R. Chelli. *J. Chem. Theory Comput.*, 10:4273, 2014.
- [87] S. Glasstone. *Thermodynamics for Chemists*. van Nostrand, New York, p. 351, 1947.
- [88] J. Gore, F. Ritort, and C. Bustamante. *Proc. Natl. Acad. Sci. U.S.A.*, 100:12564, 2003.
- [89] J. C. Gumbart, B. Roux, and C. Chipot. *J. Chem. Theory Comput.*, 9:794–802, 2013.
- [90] P. Güntert, C. Mumenthaler, and K. Wüthrich. *J. Mol. Biol.*, 273:283, 1997.
- [91] Q.-X. Guo, S.-H. Luo, and Y.-C. Liu. *J. Incl. Phenom. Mol. Recogn. Chem.*, 30:173–182, 1998.
- [92] Q.-X. Guo, X.-Q. Zheng, X.-Q. Ruan, S.-H. Luo, and Y.-C. Liu. *J. Incl. Phenom. Mol. Recogn. Chem.*, 26:175–183, 1996.
- [93] N. Hansen and W. F. van Gunsteren. *J. Chem. Theory Comput.*, 10:2632–2647, 2014.
- [94] U. H. E. Hansmann. *Chem. Phys. Lett.*, 281:140, 1997.
- [95] U. H. E. Hansmann and Y. Okamoto. *J. Comput. Chem.*, 18:920, 1997.
- [96] M. D. Hanwell, D. E. Curtis, D. C. Lonie, T. Vandermeersch, E. Zurek, and G. R. Hutchison. *J. Cheminform.*, 4:1–17, 2012.
- [97] J. Hermans and S. Shankar. *Isr. J. Chem.*, 27:225–227, 1986.
- [98] T. L. Hill. *Cooperativity Theory in Biochemistry*. 1st ed. Springer Series in Molecular Biology, Springer-Verlag, New York, p. 8, 1985.
- [99] W. G. Hoover. *Phys. Rev. A*, 31:1695, 1985.
- [100] W. G. Hoover. *Phys. Rev. A*, 34:2499–2500, 1986.

## BIBLIOGRAPHY

---

- [101] V. Hornak, R. Abel, A. Okur, B. Strockbine, A. Roitberg, and C. Simmerling. *Proteins: Struct. Funct. Bioinf.*, 65:712–725, 2006.
- [102] X. Huang, G. R. Bowman, and V. S. Pande. *J. Chem. Phys.*, 128:205106, 2008.
- [103] G. A. Huber and J. A. McCammon. *Phys. Rev. E*, 55:4822, 1997.
- [104] K. Hukushima and K. Nemoto. *J. Phys. Soc. Jpn.*, 65:1604, 1996.
- [105] L. Ingber. *Mathl. Comput. Modelling*, 18:29–57, 1993.
- [106] C. Jarzynski. *Phys. Rev. Lett.*, 78:2690, 1997.
- [107] C. Jarzynski. *Phys. Rev. E*, 56:5018–5035, 1997.
- [108] C. Jarzynski. *Phys. Rev. E*, 56:5018–5035, 1997.
- [109] C. Jarzynski. *Phys. Rev. Lett.*, 78:2690, 1997.
- [110] C. Jarzynski. *Phys. Rev. E*, 56:5018, 1997.
- [111] W. L. Jorgensen, J. K. Buckner, S. Boudon, and J. Tirado-Rives. *J. Chem. Phys.*, 89:3742–3746, 1988.
- [112] W. L. Jorgensen, J. Chandrasekhar, J. D. Madura, R. W. Impey, and M. L. Klein. *J. Chem. Phys.*, 79:926, 1983.
- [113] W. L. Jorgensen and C. Ravimohan. *J. Chem. Phys.*, 83:3050–3054, 1985.
- [114] W. L. Jorgensen and L. L. Thomas. *J. Chem. Theory Comput.*, 4:869–876, 2008.
- [115] I. Junier, A. Mossa, M. Manosas, and F. Ritort. *Phys. Rev. Lett.*, 102:070602, 2009.
- [116] J. G. Kirkwood. *J. Chem. Phys.*, 3:300, 1935.
- [117] K. N. Kirschner, A. B. Yongye, S. M. Tschampel, J. González-Outeiriño, C. R. Daniels, B. L. Foley, and R. J. Woods. *J. Comput. Chem.*, 29:622–655, 2008.
- [118] P. V. Klimovich, M. R. Shirts, and D. L. Mobley. *J. Comput. Aided Mol. Des.*, 29:397–411, 2015.

## BIBLIOGRAPHY

---

- [119] P. A. Kollman. *Chem. Rev.*, 93:2395–2417, 1993.
- [120] I. Kolossvary. *J. Phys. Chem. A*, 101:9900–9905, 1997.
- [121] A. Laio and M. Parrinello. *Proc. Natl. Acad. Sci. USA*, 99:12562–12566, 2002.
- [122] A. Lavecchia and C. D. Giovanni. *Curr. Med. Chem.*, 20:2839–2860, 2013.
- [123] C. Lee, W. Yang, and R. G. Parr. *Phys. Rev. B*, 37:785–789, 1988.
- [124] G. Lewis and M. Randall. *Thermodynamics*. McGraw-Hill, 2 edition, Revised by K. S. Pitzer and L. Brewer, pp. 244-249, 1961.
- [125] J. Liphardt, S. Dumont, S. B. Smith, I. Tinoco Jr., and C. Bustamante. *Science*, 296:1832–1835, 2002.
- [126] H. Luo and K. Sharp. *Proc. Natl. Acad. Sci. USA*, 99:10399–10404, 2002.
- [127] E. Lyman and D. M. Zuckerman. *J. Chem. Phys.*, 127:065101, 2007.
- [128] E. Lyman and D. M. Zuckerman. *J. Chem. Phys.*, 130:081102, 2009.
- [129] A. P. Lyubartsev, A. A. Martsinovski, S. V. Shevkunov, and P. N. Vorontsov-Velyaminov. *J. Chem. Phys.*, 96:1776, 1992.
- [130] P. Maragakis, M. Spichty, and M. Karplus. *Phys. Rev. Lett.*, 96:100602, 2006.
- [131] M. Marchi and P. Procacci. *J. Chem. Phys.*, 109:5194–5202, 1998.
- [132] E. Marinari and G. Parisi. *Europhys. Lett.*, 19:451, 1992.
- [133] S. Marsili, A. Barducci, R. Chelli, P. Procacci, and V. Schettino. *J. Phys. Chem. B*, 110:14011–14013, 2006.
- [134] S. Marsili, G. F. Signorini, R. Chelli, M. Marchi, and P. Procacci. *J. Comput. Chem.*, 31:1106, 2010.
- [135] G. J. Martyna, D. J. Tobias, and M. L. Klein. *J. Chem. Phys.*, 101:4177, 1994.
- [136] D. A. McQuarrie. *Statistical Mechanics*. Harper & Row, New York, 1973.

## BIBLIOGRAPHY

---

- [137] D. D. L. Minh and A. B. Adib. *Phys. Rev. Lett.*, 100:180602, 2008.
- [138] A. Mitsutake and Y. Okamoto. *Chem. Phys. Lett.*, 332:131, 2000.
- [139] S. Mukamel. *Phys. Rev. Lett.*, 90:170604, 2003.
- [140] R. M. Neal. *Stat. Comput.*, 11:125, 2001.
- [141] F. Nerattini, R. Chelli, and P. Procacci. *Phys. Chem. Chem. Phys.*, 18:15005–15018, 2016.
- [142] P. Nicolini and R. Chelli. *Phys. Rev. E*, 80:041124, 2009.
- [143] P. Nicolini, D. Frezzato, and R. Chelli. *J. Chem. Theory Comput.*, 7:582–593, 2011.
- [144] P. Nicolini, D. Frezzato, C. Gellini, M. Bizzarri, and R. Chelli. *J. Comput. Chem.*, 34:1561–1576, 2013.
- [145] P. Nicolini, P. Procacci, and R. Chelli. *J. Phys. Chem. B*, 114:9546–9554, 2010.
- [146] P. Nicolini, P. Procacci, and R. Chelli. *J. Phys. Chem. B*, 114:9546–9554, 2010.
- [147] J. P. Nilmeier, G. E. Crooks, D. D. L. Minh, and J. D. Chodera. *Proc. Natl. Acad. Sci. U.S.A.*, 108:E1009–E1018, 2011.
- [148] G. Ozer, T. Keyes, S. Quirk, and R. Hernandez. *J. Chem. Phys.*, 141:064101, 2014.
- [149] S. Park. *Phys. Rev. E*, 677:016709, 2008.
- [150] S. Park and V. S. Pande. *Phys. Rev. E*, 76:016703, 2007.
- [151] S. Park and K. Schulten. *J. Chem. Phys.*, 120:5946–5961, 2004.
- [152] A. Piserchia, M. Zerbetto, and D. Frezzato. *Phys. Chem. Chem. Phys.*, 17:8038–8052, 2015.
- [153] P. Procacci. *Phys. Chem. Chem. Phys.*, 18:14991–15004, 2016.
- [154] P. Procacci. *J. Chem. Inf. Model.*, 56:1117–1121, 2016.
- [155] P. Procacci. *J. Mol. Graph. Model.*, 71:233–241, 2017.

---

BIBLIOGRAPHY

---

- [156] P. Procacci, M. Bizzarri, and S. Marsili. *J. Chem. Theory Comput.*, 10:439–450, 2014.
- [157] P. Procacci and C. Cardelli. *J. Chem. Theory Comput.*, 10:2813–2823, 2014.
- [158] P. Procacci and R. Chelli. *J. Chem. Theory Comput.*, 13:1924–1933, 2017.
- [159] P. Procacci, S. Marsili, A. Barducci, G. F. Signorini, and R. Chelli. *J. Chem. Phys.*, 125:164101, 2006.
- [160] R. K. Raju, I. H. Hillier, N. A. Burton, M. A. Vincent, S. Doudou, and R. A. Bryce. *Phys. Chem. Chem. Phys.*, 12:7959–7967, 2010.
- [161] J. C. Reid, E. M. Sevick, and D. J. Evans. *Europhys. Lett.*, 72:726, 2005.
- [162] B. Roux, M. Nina, R. Pomes, and J. C. Smith. *Biophys. J.*, 71:670–681, 1996.
- [163] J-P. Ryckaert and G. Ciccotti H. J. C. Berendsen. *J. Comput. Phys.*, 23:327–341, 1977.
- [164] R. B. Sandberg., M. Banchelli, C. Guardiani, S. Menichetti, G. Caminati, and P. Procacci. *J. Chem. Theory Comput.*, 11:423–435, 2015.
- [165] I. Sanemasa and Y. Akamine. *Bull. Chem. Soc. Jpn.*, 60:2059–2066, 1987.
- [166] E. Schöll-Paschinger and C. Dellago. *J. Chem. Phys.*, 125:054105, 2006.
- [167] S. Schuler, T. Speck, C. Tietz, J. Wrachtrup, and U. Seifert. *Phys. Rev. Lett.*, 94:180602, 2005.
- [168] J. M. Schurr and B. S. Fujimoto. *J. Phys. Chem. B*, 107:14007, 2003.
- [169] C. Schwieters, J. Kuszewski, N. Tjandra, and G. Clore. *J. Magn. Reson.*, 160:65, 2003.
- [170] H. Senderowitz, F. Guarnieri, and W. C. Still. *J. Am. Chem. Soc.*, 117:8211–8219, 1995.
- [171] H. M. Senn and W. Thiel. *Angew. Chem.-Int. Edit.*, 48:1198–1229, 2009.
- [172] J. Shen, W. Li, G. Liu, Y. Tang, and H. Jiang. *J. Phys. Chem. B*, 113:10436–10444, 2009.

## BIBLIOGRAPHY

---

- [173] T. Shen and D. Hamelberg. *J. Chem. Phys.*, 129:034103, 2008.
- [174] M. R. Shirts, E. Bair, G. Hooker, and V. S. Pande. *Phys. Rev. Lett.*, 91:140601, 2003.
- [175] M. R. Shirts and J. D. Chodera. *J. Chem. Phys.*, 129:124105, 2008.
- [176] M. R. Shirts, D. L. Mobley, and J. D. Chodera. *Annu. Rep. Comput. Chem.*, 3:41–59, 2007.
- [177] M. R. Shirts and V. S. Pande. *J. Chem. Phys.*, 122:144107, 2005.
- [178] B. Shoichet. *Nature*, 432:862–865, 2004.
- [179] G. F. Signorini, E. Giovannelli, Y. G. Spill, M. Nilges, and R. Chelli. *J. Chem. Theory Comput.*, 10:953–958, 2014.
- [180] J. L. Smart, T. J. Marrone, and J. A. McCammon. *J. Comput. Chem.*, 18:1750–1759, 1997.
- [181] M. Sotomayor and K. Schulten. *Science*, 316:1144–1148, 2007.
- [182] Y. G. Spill, G. Bouvier, and M. Nilges. *J. Comput. Chem.*, 34:132–140, 2013.
- [183] Y. Sugita and Y. Okamoto. *Chem. Phys. Lett.*, 314:141, 1999.
- [184] R. H. Swendsen and J-S. Wang. *Phys. Rev. Lett.*, 57:2607–2609, 1986.
- [185] P. Talkner and P. Hänggi. *J. Phys. A*, 40:F569, 2007.
- [186] K. Tazaki and K. Shimizu. *J. Phys. Chem. B*, 102:6419–6424, 1998.
- [187] M. C. Tesi, E. J. J. van Rensburg, E. Orlandini, and S. G. Whittington. *J. Stat. Phys.*, 82:155, 1996.
- [188] G. M. Torrie and J. P. Valleau. *J. Comput. Phys.*, 23:187–199, 1977.
- [189] I. M. Trofymchuk, L. A. Belyakova, and A. G. Grebenyuk. *J. Incl. Phenom. Macrocycl. Chem.*, 69:371–375, 2011.
- [190] E. E. Tucker and S. D. Christian. *J. Am. Chem. Soc.*, 106:1942–1945, 1984.

## BIBLIOGRAPHY

---

- [191] M. Tuckerman, B. J. Berne, and G. J. Martyna. *J. Chem. Phys.*, 97:1990–2001, 1992.
- [192] M. E. Tuckerman, B. J. Berne, G. J. Martyna, and M. L. Klein. *J. Chem. Phys.*, 99:2796, 1993.
- [193] Mark E. Tuckerman, Yi Liu, Giovanni Ciccotti, and Glenn J. Martyna. *J. Chem. Phys.*, 115:4, 2001.
- [194] P. J. M. van Laarhoven and E. H. L. Aarts. *Simulated Annealing: Theory and Applications*, volume 37 of *Mathematics and Its Applications*. Springer, 1987.
- [195] H. Vashisth and C. F. Abrams. *Biophys. J.*, 95:4193–4204, 2008.
- [196] M. B. Vester-Christensen, M. A. Hachem, B. Svensson, and A. Henriksen. *J. Mol. Biol.*, 403:739–750, 2010.
- [197] M. De Vivo, M. Masetti, G. Bottegoni, and A. Cavalli. *J. Med. Chem.*, 59:4035–4061, 2016.
- [198] J. Vymětal and J. Vondrášek. *J. Phys. Chem. B*, 114:5632–5642, 2010.
- [199] G. M. Wang, E. M. Sevick, E. Mittag, D. J. Searles, and D. J. Evans. *Phys. Rev. Lett.*, 89:050601, 2002.
- [200] L. Wang, Y. Wu, Y. Deng, B. Kim, L. Pierce, G. Krilov, D. Lupyan, S. Robinson, M. K. Dahlgren, J. Greenwood, D. L. Romero, C. Masse, J. L. Knight, T. Steinbrecher, T. Beuming, W Damm, E. Harder, W. Sherman, M. Brewer, R. Wester, M. Murcko, L. Frye, R. Farid, T. Lin, D. L. Mobley, W. L. Jorgensen, B. J. Berne, R. A. Friesner, and R. Abel. *J. Am. Chem. Soc.*, 137:2695–2703, 2015.
- [201] L. Wickstrom, P. He, E. Gallicchio, and R. M. Levy. *J. Chem. Theory Comput.*, 9:3136–3150, 2013.
- [202] S. R. Williams, D. J. Searles, and D. J. Evans. *Phys. Rev. Lett.*, 100:250601, 2008.
- [203] H. J. Woo and B. Roux. *Proc. Natl. Acad. Sci. USA*, 102:6285–6830, 2005.
- [204] T. Yamada and K. Kawasaki. *Prog. Theor. Phys.*, 38:1031, 1967.

## BIBLIOGRAPHY

---

- [205] F. M. Ytreberg. *J. Chem. Phys.*, 130:164906, 2009.
- [206] M. Zerbetto and D. Frezzato. *Phys. Chem. Chem. Phys.*, 17:1966–1979, 2015.
- [207] M. Zerbetto, A. Piserchia, and D. Frezzato. *J. Comput. Chem.*, 35:1865–1881, 2014.
- [208] L. Zhang and J. Hermans. *Proteins: Struct., Func., Gen.*, 24:433–438, 1996.
- [209] Z. Zhang, T. Wu, Q. Wang, H. Pan, and R. Tang. *J. Chem. Phys.*, 140:034706, 2014.
- [210] D. M. Zuckerman and T. B. Woolf. *Chem. Phys. Lett.*, 351:445–453, 2002.
- [211] R. W. Zwanzig. *J. Chem. Phys.*, 22:1420, 1954.